Doctoral Dissertation

Proton transport property and organized structure in polymer electrolyte thin films

高分子電解質薄膜の組織構造とプロトン輸送特性

Yutaro Ono

Supervisor: Associate Professor Yuki Nagao

School of Materials Science

Japan Advanced Institute of Science and Technology

Table of contents

List of figure

Chapter 1

Chapter 2.

Chapter 3.

List of scheme

Chapter 1.

Chapter 2.

Chapter 3.

List of table

Chapter 2.

Chapter 3.

Chapter 1. General Introduction

1-1. Fuel cell

The majority of japan energy production is derived from the burning of fossil fuels such as liquefied natural gas (LNG), petroleum and coal, which results in the emission of large amounts of the greenhouse gas (CO_2) in addition to environmental pollution. Polymer electrolyte fuel cells (PEFCs) are expected to be an important technology for solving the environmental problem and energy strategy. PEFCs have a high power density, environmental friendliness and relatively efficient in their conversion of chemical energy to electrical energy. In general, PEFCs require hydrogen and oxygen as a fuel for their operation. Exhaust of the PEFCs is free of CO_2. Therefore, PEFCs have attracted interest from wide application such as zero emission vehicles, portable energy source and etc. Toyota Motor Cooperation published the first commercial fuel cell vehicles on Dec 2014.

The PEFCs consists of a membrane electrode assembly (MEA), gas diffusion layer (GDL), separator and current collector as shown in Figure 1-1. The MEA is fabricated by heat press method using two catalyst layer (CL) and polymer electrolyte membrane (PEM). Generally, CL and PEM use costly carbon supported platinum type metal

catalysts and sulfonic acid functionalized polymers such as Nafion (Figure.1-2). Figure 1-3 shows breakdown for cost of the PEFC. At the various components of the PEFCs, CL and PEM play an important role, which are strongly contribute to cost of the PEFC [1]. Especially, PEM is expected to be many ideal specific such as high ion conductivity, excellent mechanical and chemical stability, and low cost. Therefore, over the last decade the proton-conducting PEM for fuel cell have been developed extensively [2-8].

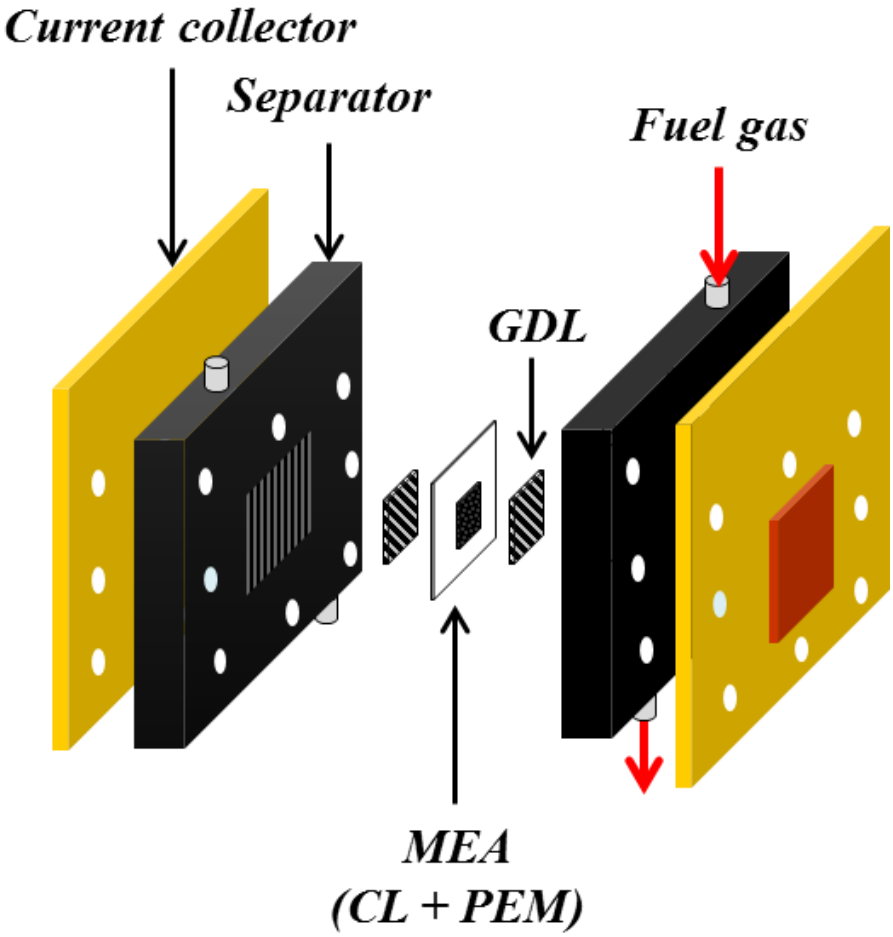

Figure 1-1. Schematic illustration of Polymer electrolyte fuel cell (PEFC)

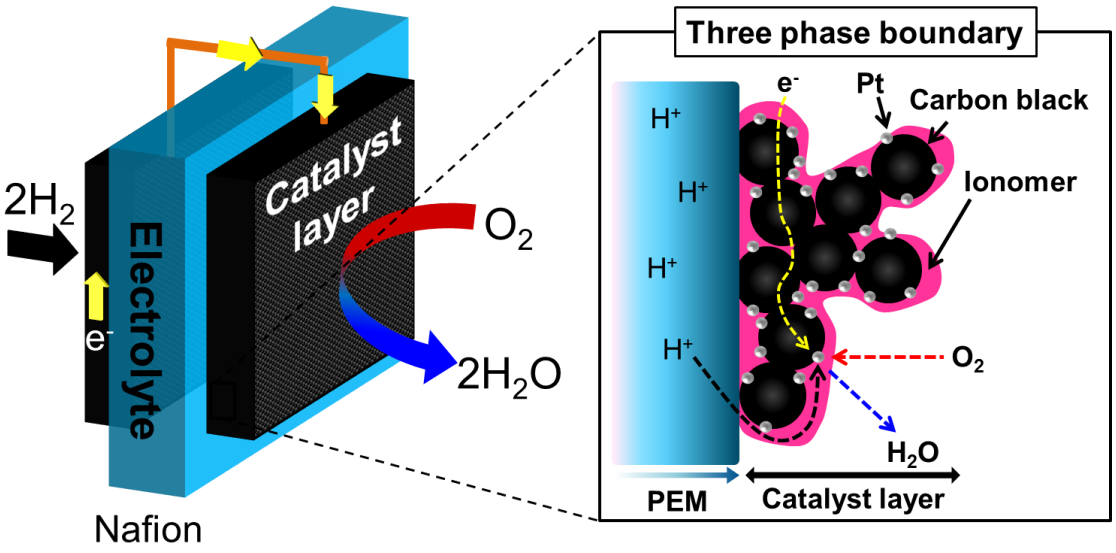

Figure 1-2. Schematic illustration of a membrane electrode assembly (MEA) and function of a catalyst layer.

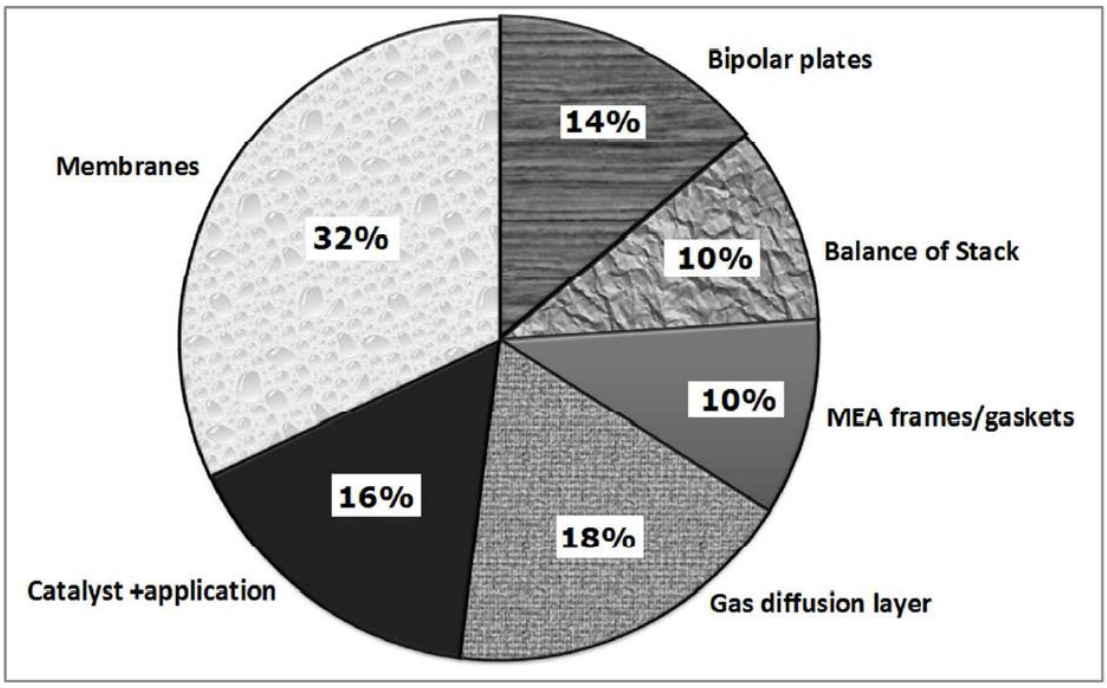

Figure 1-3. Breakdown of the 2013 projected PEFC stack cost at 1,000/year production of 80-kW systems [2].

1-2. Polymer electrolyte

1-2-1. Perfluorosulfonated ionomers

For commercialization of the PEFCs, much effort has been devoted for the research of advanced polymer electrolyte because of the polymer electrolyte is one of the most important components of fuel cell. The most widely used PEM are perfluorosulfonated polymers such as Nafion. Nafion is originally used in chlor-alkali process for produce chlorine and sodium hydroxide [5]. They compose of the polytetrafluoroethylene (PTFE) backbone and perfluorinated ether side chains terminated by super acidic sulfonic acid groups as shown in Scheme 1. Nafion is one of the most promising PEM for PEFC because of their high proton conductivity, excellent thermal and chemical stability due to the special chemical structure. For understanding of high proton conductivity of the Nafion, the higher order structure in commercial bulk Nafion membrane has been investigated by variety of scattering methods such as small-angle X-ray scattering (SAXS) (Figure.1-4) [9-12]. Hsu and Gierke have reported the famous morphological model of the Nafion membrane [9]. Their study has revealed a phase segregation structure between the hydrophobic and hydrophilic parts and 4 nm inverted micelle clusters and 1 nm channel in Nafion (Figure 1-4(a)). Furthermore, other groups

revealed the elongated polymeric aggregates with ionic groups are packed with an orientation ordering in bundles [10-12] (Figure 1-4 (b), (c)).

Although perfluorosulfonated polymers show excellent performance for fuel cell, it has some drawbacks. Perfluorosulfonated polymers have relatively low glass transition temperatures, and the proton conductivity decrease above 100° because of the ionic cluster is dehydrated [2-5]. Perfluorosulfonated polymers are expensive because of their complex manufacturing process due to the special chemical structure [2,5,6] . Moreover, complex manufacturing processes contribute to impediments of the synthesis strategy and poor flexibility of the molecular design. Therefore, many sulfonic acids functionalized hydrocarbon based PEM have been intensively studied for alternative PEM [2-4, 6-8].

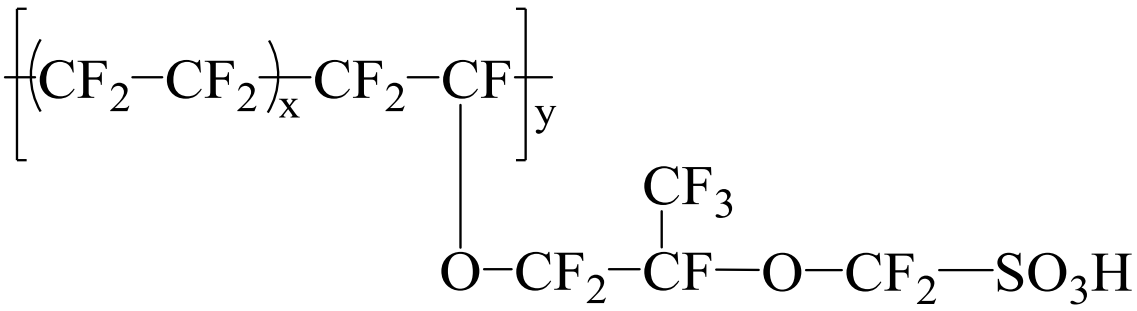

Scheme 1-1. Nafion chemical structure

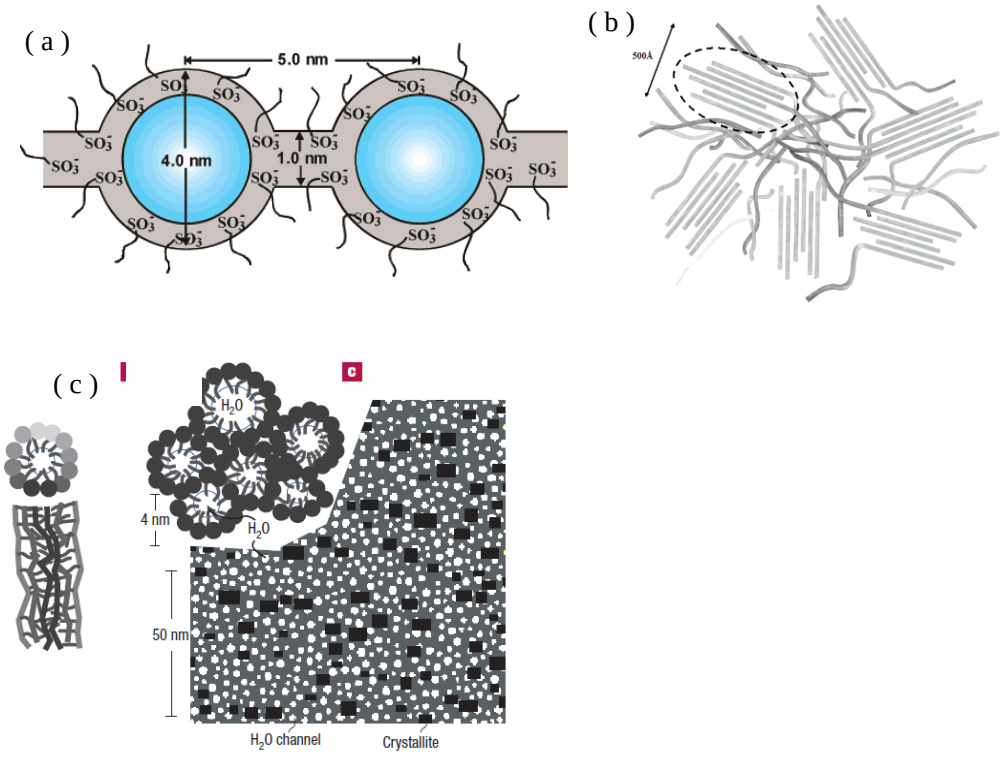

.

Figure 1-4. Schematic representations of the Nafion structure.

(a) Cluster-network model [9]

(b) Lodlike aggregate model [10]

(c) Inverted-micelle cylinder model [11]

1-2-2. Nafion thin film

Nafion is also commonly used in a dispersion state with various solvents for the preparation of catalyst layers for PEFC [13]. It is present as few nm thick film with three-phase boundary of catalyst (Pt or Pt alloy) and gas (Figure 1-2.) [13,14]. Understanding this interface has become necessary because the properties of the Nafion thin film may be drastically different from bulk membranes and reactions in the PEFC occur at those interfaces. Therefore, characterization of thin film structure and proton transport property is important.

Recently, several studies of Nafion thin films have reported the structure [15-25], proton conductivity [23, 26-31], water uptake [22, 23, 32-34] and diffusion coefficient [21,28]. Siroma *et al.* [31], Paul *et al*. [26-28], and Nagao [29,30] demonstrated the in-plane proton conductivity decreases with decreasing thickness in Nafion thin film, which prepared by drop casting, self-assemble, and spin-coating respectively. The structural models of Nafion thin films have been investigated by scattering methods such as Neutron reflectivity (NR)(14-18), grazing incidence small-angle X-ray scattering (GI-SAXS)[19-23], X-ray specular reflectivity (XRR)[24], and other techniques [35-38] . These structural models completely differ from the bulk Nafion membrane and depend on the thickness and surface state of substrate (Figure 1-5).

However, for use in fuel cell operations, the structure and proton conductivity of Nafion thin films on a Pt surface has not been investigated systematically.

(a)

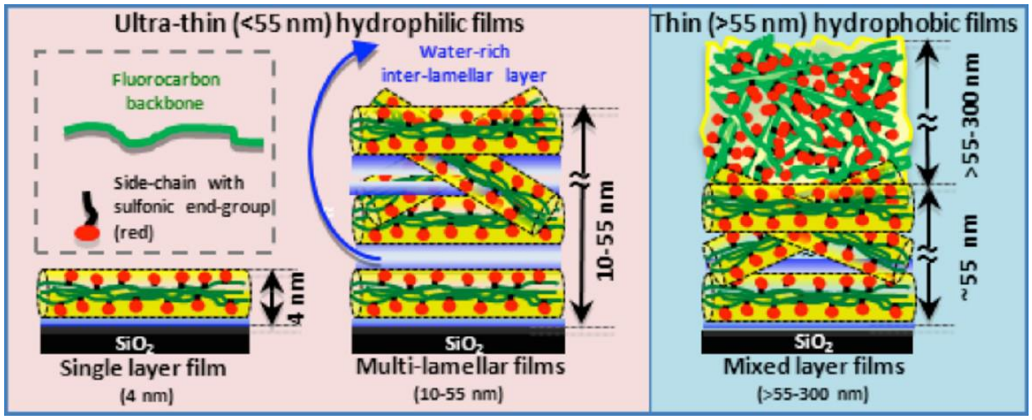

(b)

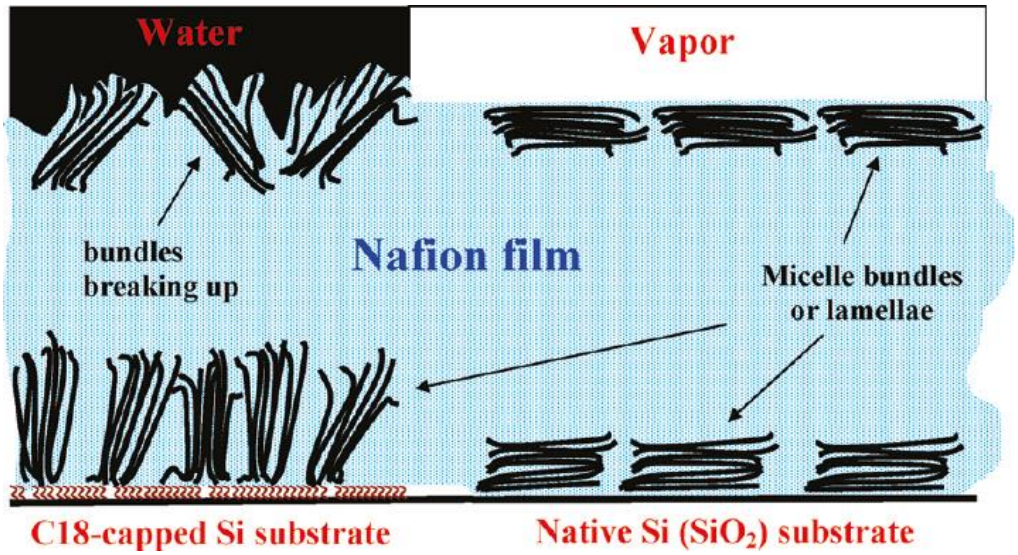

Figure 1-5. Schematic representations of the Nafion thin film structure. (a) Thickness dependent [35], (b) surface dependent nano-structure [21].

1-2-3. Hydrocarbon based ionomers

The various sulfonic acids functionalized aromatic hydrocarbon based PEMs including the polyimides [38-47], polyphenylenes [48-52], polybenzimidazoles [53] and poly(ether ketone)[54-59] have been reported for alternative PEM (Scheme 1-2). These molecular designs are based on the phase segregation structure. Because proton is considered to be transported smoothly through the hydrophilic sulfonic acid part in phase segregation structure. Miyatake *et al*. have synthesized many sulfonic acids functionalized poly(ether ether ketone) and polyimides ionomers [42-44, 54,55,57,58]. It was reported in the literature that the poly(ether ether ketone) and polyimide ionomers exhibited good proton conductivity, chemical stability and fuel cell performance comparable to or higher than perfluorosulfonated ionomers[42, 58] . To improve further proton conductivity and chemical stability with phase segregation structure, many researchers developed sulfonated block copolymers [51,52,55,58]. Amphiphilic block copolymers are composed of the long hydrophobic and hydrophilic part. Therefore, these block copolymers have larger scale for phase segregation and wider nano-channel than random copolymers [7]. Mochizuki and Miyatake *et al*. have reported that difference of the phase segregation morphology, proton conductivity and water uptake at the perfluorosulfonated ionomers and hydrocarbon based block copolymers [60]. In perfluorosulfonated ionomers cases, hydrophilic ionic channel orders with water

uptake(Figure1-7 (a) and (b)). The hydrocarbon based block copolymers show the randomization of the hydrophilic ionic channel with increasing the water uptake (Figure1-7 (c) and (d)). The block copolymers with wide nano-channels have been considered to exhibit higher proton conductivity than random copolymers with narrower channels because the block copolymers have continuous nano-channel [7]. However, recent study of the advanced ionomers has demonstrated that the much wide channels are not necessary for proton conductive channel [61]. Mochizuki and Miyatake *et al*. have reported that the uniform hydrophilic channel is important for PEFC. Rikukawa *et al*. demonstrated that the well-defined ordered structures contribute to high proton conductivity at the low relative humidity (RH) region [52]. In summary, many reports have described studies of the alternative PEM. Sulfonated aromatic hydrocarbon based PEMs have been most intensively investigate. Recent studies pointed out that the importance of the well-defined and uniform hydrophilic channel rather than channel size. However, relationship between the proton transport property and detailed structure of the hydrophilic channel has not been described. Moreover, alternative PEM is limited within the concept of the chemical modification as described later (chapter 1-3).

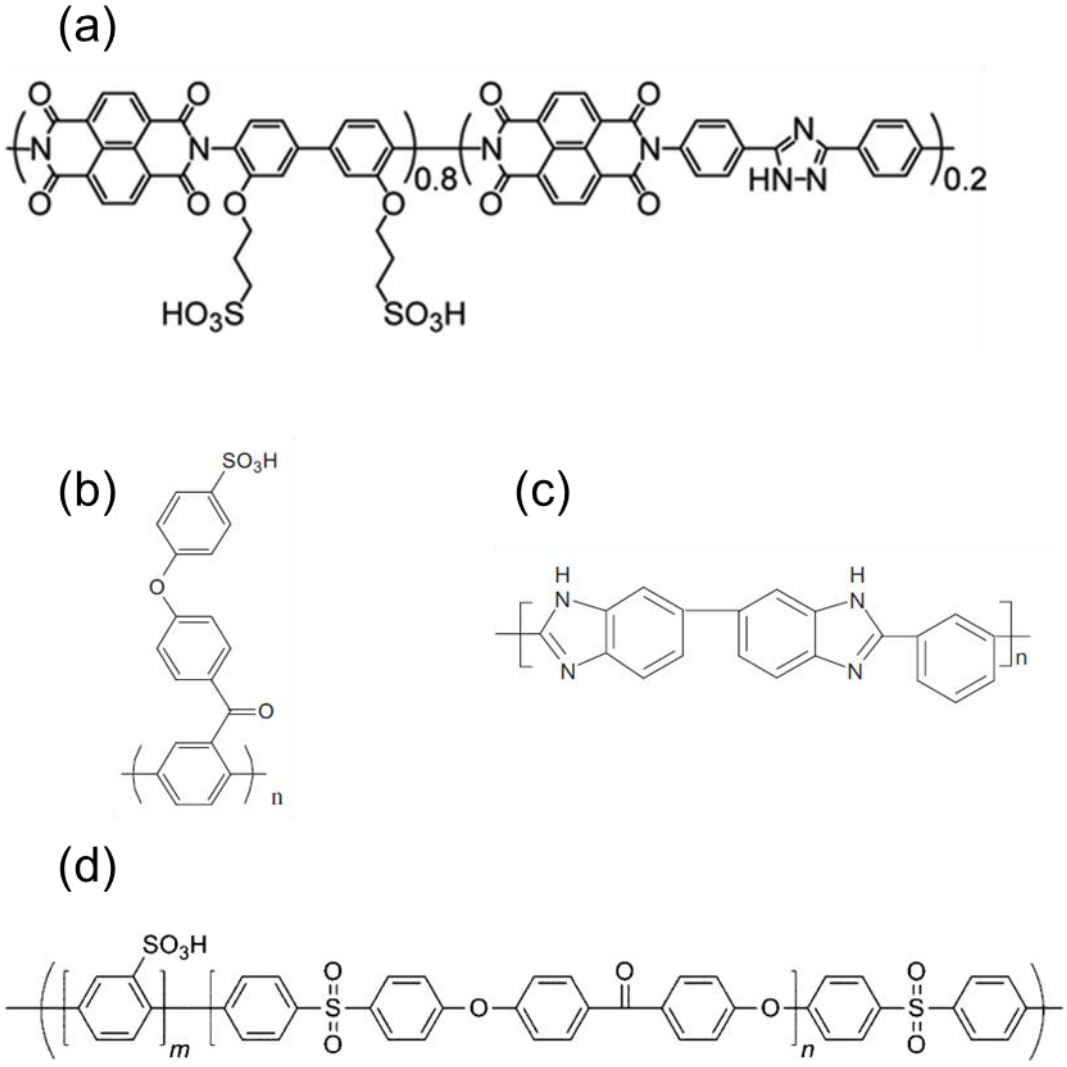

Scheme 1-2. Chemical structurer of the (a) sulfonated polyimide [43], (b) polyphenylenes [48], (c) polybenzimidazoles [53], (d) poly(ether ketone)[57].

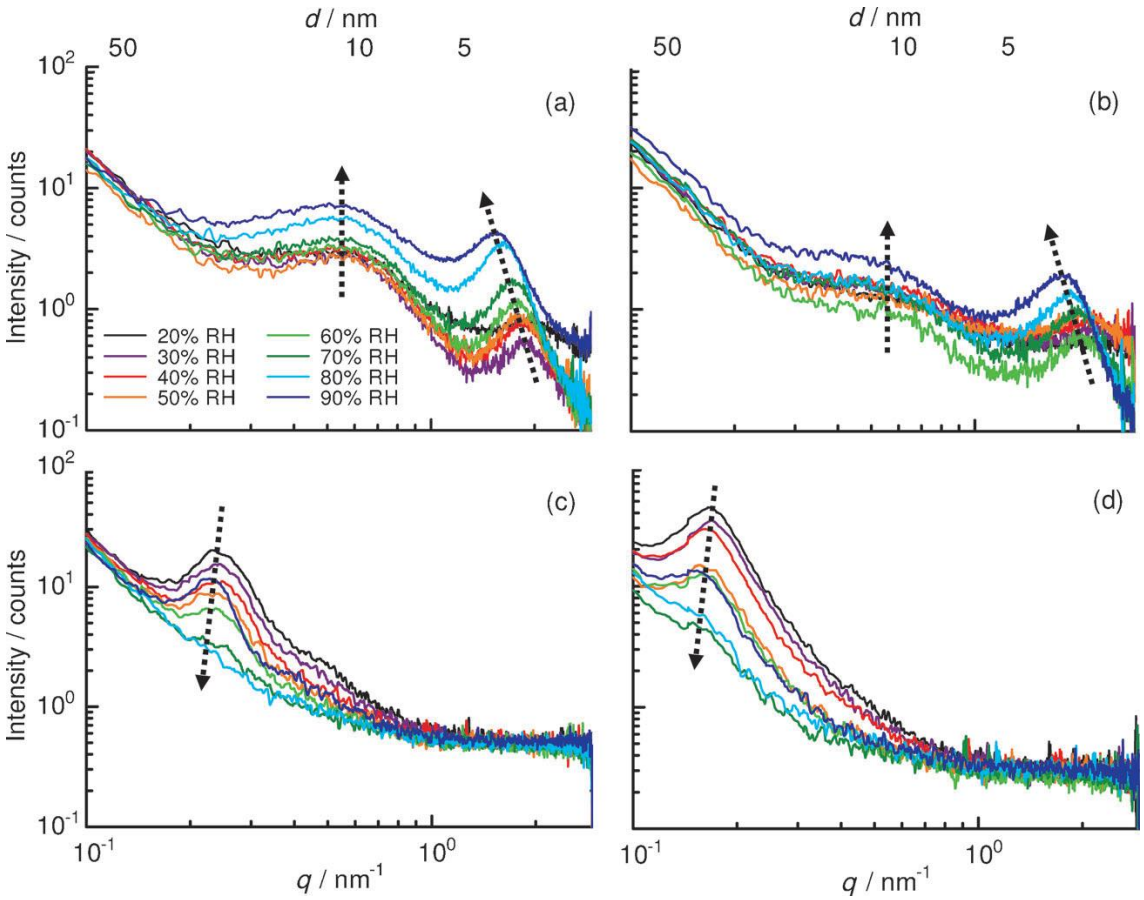

Figure 1-6. SAXS profiles for (a) Nafion, (b) Aquivion, (c) Poly(arylene ether sulfone ketone) multiblock copolymer, (d) poly(arylene ether) block copolymer [60] .

1-3. Factor of the controlling proton conductivity

Controlling proton conductivity will be the important factor to design further improved PEM. The most fundamental approach to achieve the high proton conductivity is to increase the ion exchange capacity (IEC). Because IEC directly affects ion concentration of the PEM. PEM with high IEC exhibits the highly water uptake, resulting in higher proton conductivity compared with PEM with low IEC. An acidity of the PEM is also one of the important factors for high proton conductivity.

High acidity contributes to highly water uptake at low humidity, meaning that proton conductivity at low humidity improves. Recently, some groups have demonstrated that aromatic ionomers with perfluorinated side chains can improve proton conductivities under low humidity [44, 49, 63]. The high acidity of the perfluoroalkyl sulfonic acid groups (*pKa* = c.a.-14) contributes to more effective proton conductivity compared to lower acidity of the aromatic (*pKa* = c.a.-2.5) and alkyl (*pKa* = c.a.-0.6) sulfonic acid. For example Rikukawa *et al*. have synthesized a novel poly(phenylene) with perfluoroalkyl sulfonic acid groups at the side chain [49]. These membranes showed high proton conductivity and water uptake compared with non-fluoro membranes (Figure1-7). However, approach of the high acidity of the sulfonic acid groups limited to the polymer main chain and side chain such as fluoro and aromatic. Moreover, high IEC PEM exhibits to the poor mechanical stability and soluble in water [7, 39]. Therefore, an innovative strategy for design of the high proton conductive PEM has been needed.

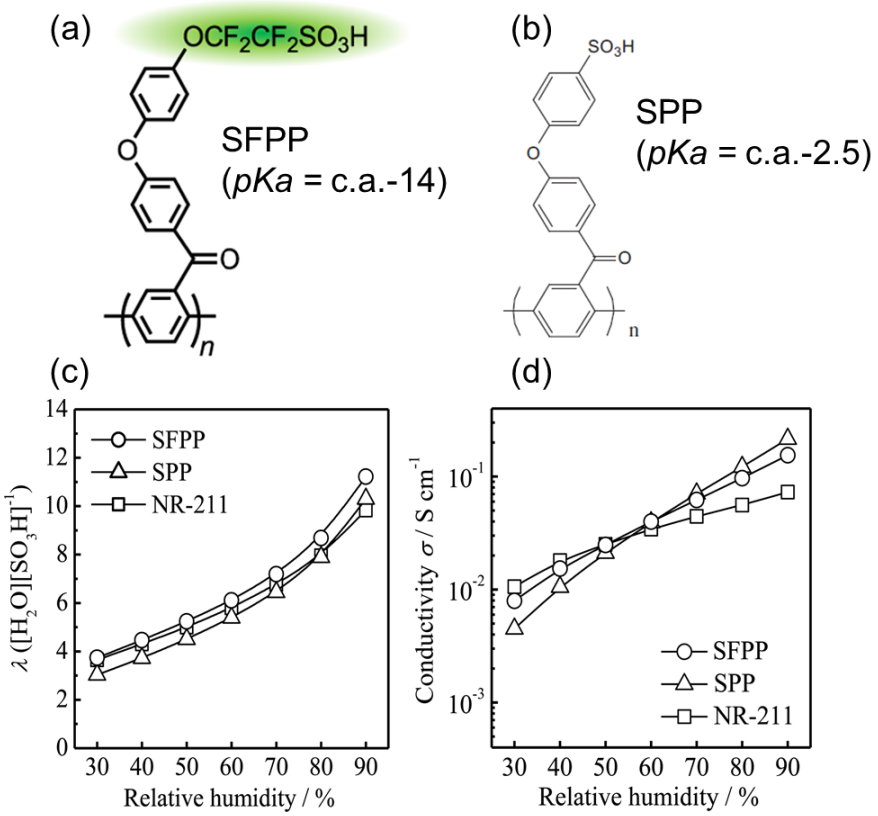

Figure 1-7. Chemical structurer of the (a) polyphenylenes with perfluoroalkyl sulfonic acid groups (SFPP) and (b) polyphenylenes with aromatic shifonic acids groups (SPP). Humidity dependence of the water uptake and proton conductivity of SFPP, SPP and Nafion [49].

1-4. New strategy for high proton conductive PEM

Recent investigations have reported the enhancement of proton conductive properties by the structural control of the conductive channel without chemical modification. For examples, Kawakami *et al.* has revealed that uniaxially aligned sulfonated polyimide shows the high proton conductivity and good mechanical stability [45-47]. These results indicate the possibility of the enhancement proton conductivity using the oriented molecular structure. However, relationships between nano structure and proton transport properties of highly proton conductive polymers are still not well understood, because nature of many proton conductive polymers has amorphous.

For uniformed or continuous proton conductive channel, the various techniques and materials for fabrication of the proton conductive material are described which including the Langmuir-Blodgett films [64,65], spin-coat films [66], coordination polymer [67], graphene oxides [68] and liquid crystal [69]. The well-defined two-dimensional lamella structure of the Langmuir-Blodgett film with carboxylic acid showed the high in-plane proton conductivity and large anisotropic proton conductivity (Figure 1-8) [64]. Highly oriented polypeptide film using the spin-coat method showed that the one order of magnitude higher proton conductivity compared with the bulk sample [66]. These results indicate that high proton conductivity can be attained even

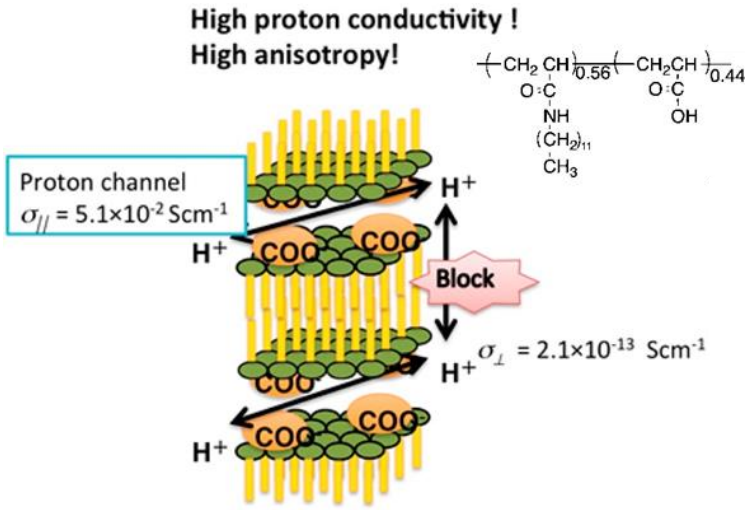

Figure 1-8. Schematic illustration of well-defined two-dimensional lamella structure of the Langmuir-Blodgett film [64].

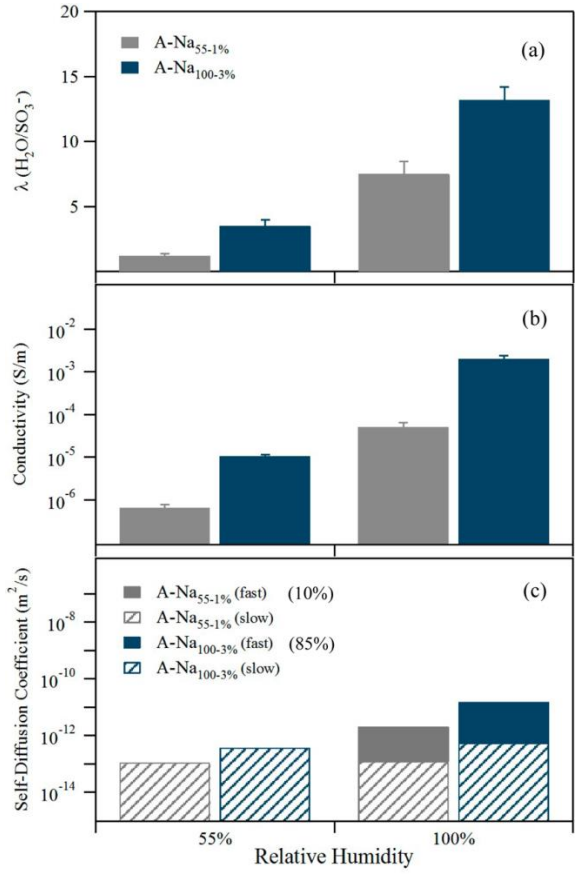

Figure 1-9. (a) Water uptake, (b) through plane ionic conductivity, and (c) diffusion coefficients measured at different relative humidity conditions for A-Na55–1% (hexagonal) and A-Na100–3% (bicontinuous) membranes [74].

in a weak acid group (carboxylic acid) with an oriented thin film. In the case of the porous coordination polymers (PCP) and Metal–Organic Frameworks (MOF), nanopores functioned as highly proton conductive channels with guest molecules and hydrogen-bonding network [67]. A liquid crystal material has attracted attention due to fabrication of nanostructures by using molecular self-organization processes [69-74]. This organized structure forms uniform and definite proton conduction channel. Kato *et al.* have examined the glassy liquid crystals preserving bicontinuous cubic structure [69]. This glassy liquid-crystalline material exhibits proton conduction due to formation of hydrogen-bonding network by water uptake. Hernandez *et al.* have reported the photo-cross-linking process to liquid-crystalline structures formed by self-assembly. These cross-linked liquid-crystalline materials succeeded nanostructured polymer membranes with ionic channel in different liquid-crystalline phases such as hexagonal, lamellar and bicontinuous cubic [74]. Interestingly, the ionic conductivity and water uptake of these polymer membranes were found to be strongly dependent on the liquid-crystalline phases (Figure 1-9). As described above, liquid-crystalline material may present opportunities to investigate the relationship between the structure and proton conductivity. Moreover, various liquid-crystalline phases are an attractive for understanding the proton conduction mechanism.

Proton conductive material using liquid-crystalline property

Recently, a number of new ion conductive liquid-crystalline (LC) materials have been developed and relationships between the molecular assembled nanostructures and property have been studied [70-81]. These materials comprised ionic liquids and thermotropic LC property. Generally, thermotropic LC materials exhibit a various LC phases and orientation at the different temperature and photo irradiation [82, 83]. Moreover, these ion conductive LC materials show the interesting property such as one dimensional ion transport, switching of ionic conductivity and phase transition. In contrast, there are a number of limited reports on the application of lyotropic LC materials for ion and proton transport.

Lyotropic LC property is observed when an amphiphile is dissolved in a solvent such as water or selective solvent [84]. This amphiphile requires a rigid molecular structure and dissolve only one end of the molecular. The molecular structure of this amphiphile is very similar to the concept of the aromatic PEM. For example, Wegner *et al.* reported that the poly (p-Pheneylene sulfonic acid) and alkyl substituted (p-Pheneylene) showed the lyotropic behaver in DMSO solution [85, 86]. Vile *et al.* reported that the poly(p-sulfophenylene sulfoterephthalamide) shows that the nematic LC phase in water [87, 88]. Chen *et al.* revealed that the wedge-shaped sulfonate

amphiphile shows the phase transition with increase in humidity (Figure1-9) [87]. These results indicate that the combination of the rigid molecular structure and sulfonic acid groups lead to a lyotropic LC property. However, these lyotropic LC properties were used for only fabrication of polymer film [48, 74, 89, 90]. Currently, less is known about direct relation between the lyotropic LC property and proton conductivity.

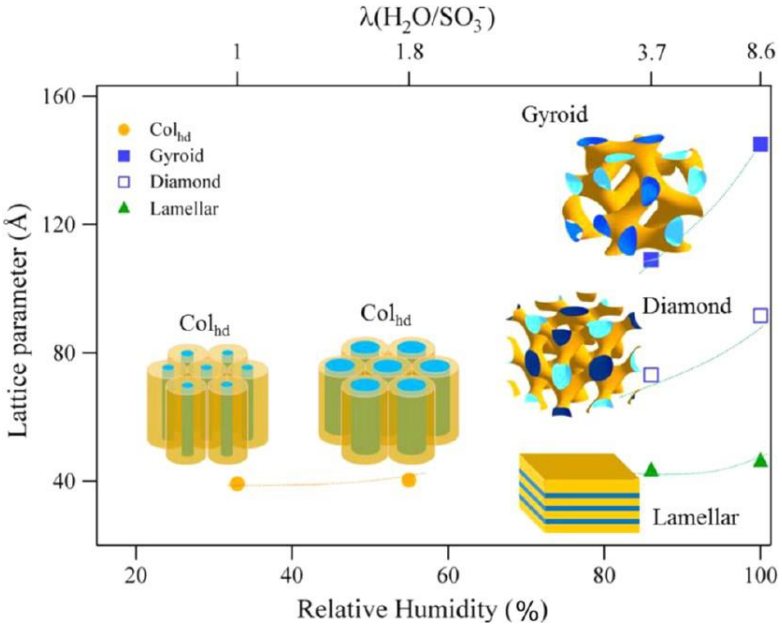

Figure 1-9. Evolution of the lattice parameter as a function of RH (bottom horizontal axis) and water uptake (top horizontal axis) for wedge-shaped sulfonate amphiphile in different mesophases [87].

1-5. Research objectives

Understanding the relationships between nanostructure, and ion-transport properties are critical to the design of PEM. However, it should be difficult to directly evaluate the relationship between the structure and proton conductivity because of less structural nature in the high proton conductive PEMs. In this thesis, the author paid attention to understanding of the relationship between the proton transport property and polymer nanostructure. This research mainly addresses following two parts;

(1) Understanding the relationship between the proton transport property and Nafion thin film structure on the Pt-deposited surface. The author found the properties of the Nafion thin film was drastically different from those of bulk membranes.

(2) Demonstrating an organized structure with hydrophilic water channels using lyotropic liquid property using non-planar sulfonated polyimides with alkyl side chain (ASPI) thin films. This new synthesis enhanced discussion of relationship between the proton transport property and organized polymer nanostructure.

These findings in this research can contribute to the study of PEM for both

fundamental and application. Moreover, it can extend to understand lyotropic LC property in solid state materials.

The chapter 2 and chapter 3 are based on the strategy of relation between the interfacial structure and proton transport property. The former significantly decreased proton conductivity at the interface. Moreover, the interfacial structure strongly depended on the thickness and interface. The latter enables more detail discussion for the relation between the structure and proton transport property using at the interface.

1-6. Outline of thesis

In chapter 1, the general introduction of this thesis was mentioned about the State-of-the-art PEM and recent strategy using the ordered molecular structure.

In chapter 2, the proton transport property and thin film structure of the Nafion at the Pt-deposited surface were investigated. These results can contribute to understand the relationship between the proton transport property and thin film structure on the Pt-deposited surface at the three-phase boundary for fuel cells.

In chapter 3, the relationship between the proton transport property, water uptake and organized structure using sulfonated polyimide with different molecular structure was discussed.

In chapter 4, general conclusion of this research was presented. The finding can contribute not only to understand the relationship between the proton transport properties and structure but also to develop a new strategy for the PEM.

References

[1] Diat, O.: Gebel, G. Proton channels. *Nature Mater*. **2008**, *7*, 13–14.

[2] Kraytsberg, A.; Ein-Eli, Y. Review of Advanced Materials for Proton Exchange Membrane Fuel Cells. *Energy & Fuels* **2014**, *28*, 7303−7330.

[3] Rikukawa, M.; Sanui, K. Proton-conducting polymer electrolyte membranes based on hydrocarbon polymers. *Prog. Polym. Sci.* **2000**, *25*, 1463−1502.

[4] Hickner, M. A.; Ghassemi, H.; Kim, Y.; Einsla, B. R.; McGrath, J. E. Alternative Polymer Systems for Proton Exchange Membranes (PEMs). *Chem. Rev.* **2004**, *104* 4587–4611.

[5] Mauritz, K. A.; Moore, R. B. State of Understanding of Nafion. *Chem. Rev.* **2004**, *104*, 4535–4585.

[6] Li, N.; Guiver, M. D. Ion Transport by Nanochannels in Ion-Containing Aromatic Copolymers. *Macromolecules* **2014**, *47*, 2175–2198.

[7] Shin, D. W.; Guiver, M. D.; Lee, Y. M. Hydrocarbon-Based Polymer Electrolyte Membranes: Importance of Morphology on Ion Transport and Membrane Stability. *Chem. Rev.* **2017**, *117*, 4759–4805.

[8] He, G.; Li, Z.; Zhao, J.; Wang, S.; Wu, H.; Guiver, M. D.; Jiang, Z. Nanostructured Ion-Exchange Membranes for Fuel Cells: Recent Advances and Perspectives. *Adv.*

Mater. **2015**, *27*, 5280–5295.

[9] Hsu, W. Y.; Gierke, T. D. Ion transport and clustering in Nafion perfluorinated membranes. *J. Membr. Sci.* **1983**, *13*, 307−326.

[10] Gebel, G.; Diat, O. Neutron and X-ray Scattering: Suitable Tools for Studying Ionomer Membranes. *Fuel cells* **2005**, *5*, 261−276.

[11] Rubatat, L.; Gebel, G.; Diat, O. Fibrillar Structure of Nafion: Matching Fourier and Real Space Studies of Corresponding Films and Solutions. *Macromolecules* **2004**, *37*, 7772−7783.

[12] Schmidt-Rohr, K.; Chen, A. Q. Parallel cylindrical water nanochannels in Nafion fuel-cell membranes. *Nature Mater.* **2008**, *7*, 75−83.

[13] Holdcroft, S. Fuel Cell Catalyst Layers: A Polymer Science Perspective. *Chem. Mater*. **2014**, *26*, 381−393.

[14] Peng, H. C.; Wang, C. N.; Yeh, T. K.; Su, Y. C.; Pan, C.; Tseng, F. G. A high efficient micro-proton exchange membrane fuel cell by integrating micro-nano synergic structures. *Journal of Power Sources* **2014**, *225*, 277−285.

[15] Murthi, V. S.; Dura, J. A.; Satija, S.; Majkrzak, C. F. Water Uptake and Interfacial Structural Changes of Thin Film Nafion Membranes Measured by Neutron Reflectivity for PEM Fuel Cells. *ECS Trans.* **2008**, *16*, 1471–1485.

[16] Dura, J. A.; Murthi, V. S.; Hartman, M.; Satija, S.; Majkrzak, C. F. Multilamellar Interface Structures in Nafion. *Macromolecules* **2009**, *42*, 4769–4774.

[17] Kim, S.; Dura, J. A.; Page, K. A.: Rowe, B. W.; Yager, K. G.; Lee, H. J.; Soles, C. L. Surface-Induced Nanostructure and Water Transport of Thin Proton-Conducting Polymer Films. *Macromolecules* **2013**, *46*, 5630–5637.

[18] Ogata, Y.; Kawaguchi, D.; Yamada, N.L.; Tanaka, K. Multistep Thickening of Nafion Thin Films in Water. *ACS Macro. Lett.* **2013**, *2*, 856–859.

[19] Wood, D. L.; Chlistunoff, J.; Majewski, J.; Borup, L. Nafion Structural Phenomena at Platinum and Carbon Interfaces. *J. Am. Chem. Soc.* **2009**, *131*, 18096–18104.

[20] Bass, M.; Beman, A.; Singh, A.; Konovalov, O.; Freger, V. Surface Structure of Nafion in Vapor and Liquid. *J. Phys. Chem. B* **2010**, *114*, 3784–3790.

[21] Bass, M.; Beman, A.; Singh, A.; Konovalov, O.; Freger, V. Surface-Induced Micelle Orientation in Nafion Films. *Macromolecules* **2011**, *44*, 2893–2899.

[22] Modestino, M. A.; Kusoglu, A.; Hexemer, A.; Weber, A. Z.; Segalman, R. A. Controlling Nafion Structure and Properties via Wetting Interactions. *Macromolecules* **2012,** *45*, 4681–4688.

[23] Modestino, M. A.; Paul, D. K.; Dishari, S.; Petrina, S. A.; Allen, F.; Hickner, M. A.; Karan, K.; Segalman, R. A.; Weber, A. Z. Self-Assembly and Transport Limitations in

Confined Nafion Films. *Macromolecules* **2013**, *46*, 867–873.

[24] Kusoglu, A.; Kushner, D.; Paul, D. K.; Karan, K.; Hickner, M. A.; Weber, A. Z. Impact of Substrate and Processing on Confinement of Nafion Thin Films. *Adv. Funct. Mater.* **2014**, *24*, 4763–4774.

[25] Eastman, S. A.; Kim, S.; Page, K. A.; Rowe, B. W.; Kang, S.; Soles, C. L. Effect of Confinement on Structure, Water Solubility, and Water Transport in Nafion Thin Films. *Macromolecules* **2012**, *45*, 7920–7930.

[26] Paul, D. K.; Fraser, A.; Karan, K. Towards the Understanding of Proton Conduction Mechanism in PEMFC Catalyst Layer: Conductivity of Adsorbed Nafion Films. *Electrochem. Commun.* **2011**, *13*, 774–777.

[27] Paul, D. K.; McCreery, R,; Karan, K. Proton Transport Property in Supported Nafion Nanothin Films by Electrochemical Impedance Spectroscopy. *J. Electrochem. Soc.* **2014**, 161, 1395–1402.

[28] Paul, D. K.; Karan, K. Conductivity and Wettability Changes of Ultrathin Nafion Films Subjected to Thermal Annealing and Liquid Water Exposure. *J. Phys. Chem. C* **2014**, *118*, 1828–1835.

[29] Nagao, Y. Proton Transport Property of Nafion Thin Films on MgO(100) with Anisotropic Molecular Structure. *e-J. Surf. Sci. Nanotechnol*. **2012**, *10* 114–116.

[30] Nagao, Y. Highly Oriented Sulfonic Acid Groups in a Nafion Thin Film on Si Substrate. *J. Phys. Chem. C* **2013**, *117*, 3294–3297.

[31] Siroma, Z.; Kakitubo, R.; Fujiwara, N.; Ioroi, T.; Yamazaki, S.; Yasuda, K. Depression of Proton Conductivity in Recast Nafion Film Measured on Flat Substrate. J. *Power Sources* **2009**, *189*, 994–998.

[32] Kongkanand, A. Interfacial Water Transport Measurements in Nafion Thin Films Using a Quartz-Crystal Microbalance. *J. Phys. Chem. C* **2011**, *115*, 11318–11325.

[33] Abuin, G. C.; Fuertes, M. C.; Corti, H. R. Substrate Effect on the Swelling and Water Sorption of Nafion Nanomembranes. *J. Membr. Sci.* **2013**, *428*, 507–515.

[34] Dishari, S. K.; Hickner, M. A. Antiplasticization and Water Uptake of Nafion Thin Films. *ACS Macro. Lett.* **2012**, *1*, 291–295.

[35]Paul, D. K.; Karan, K.; Docoslis, A.; Giorgi, J. B.; Pearce, J. Characteristics of Self-Assembled Ultrathin Nafion Films. *Macromolecules* 2013, *46*, 3461–3475.

[36] Kendrick, I.; Kumari, D.; Yakaboski, A.; Dimakis, N.; Smotkin, E. S. Elucidating the Ionomer-electrified Metal Interface. *J. Am. Chem. Soc.* **2010**, *132*, 17611–17616.

[37] Zeng, J.; Jean, D. I.; Ji, C.; Zou, S. In Situ Surface-Enhanced Raman Spectroscopic Studies of Nafion Adsorption on Au and Pt Electrodes. *Langmuir* **2012**, *28*, 957–964.

[38] Yagi, I.; Inokuma, K.; Kimijima, K.; Notstu, H. Molecular Structure of Buried

Perfluorosulfonated Ionomer/Pt Interface Probed by Vibrational Sum Frequency Generation Spectroscopy. *J. Phys. Chem. C* **2014**, *118*, 26182–26190.

[38] Genies, C.; Mercier, R.; Sillion, B.; Cornet, N.; Gebel, G.; Pineri, M. Soluble sulfonated naphthalenic polyimides as materials for proton exchange membranes. *Polymer* **2001**, *42*, 359–373.

[39] Fang, J. H.; Guo, X. X.; Harada, S.; Watari, T.; Tanaka, K.; Kita, H.; Okamoto, K. Novel sulfonated polyimides as polyelectrolytes for fuel cell application. 1. Synthesis, proton conductivity, and water stability of polyimides from 4,4′ -diaminodiphenyl ether-2,2-disulfonic acid. *Macromolecules* **2002**, *35*, 9022–9028.

[40] Guo, X. X.; Fang, J. H.; Watari, T.; Tanaka, K.; Kita, H.; Okamoto, K. Novel sulfonated polyimides as polyelectrolytes for fuel cell application. 2. Synthesis and proton conductivity, of polyimides from 9,9-bis(4-aminophenyl)fluorene-2,7-disulfonic acid. *Macromolecules* **2002**, *35*, 6707–6713.

[41] Watari, T.; Fang, J. H.; Tanaka, K.; Kita, H.; Okamoto, K.; Hirano, T. Synthesis, water stability and proton conductivity of novel sulfonated polyimides from 4,4′ -bis(4-aminophenoxy)biphenyl-3,3-disulfonic acid. *J. Membr. Sci.* **2004**, *230*, 111–120.

[42]Asano, N.; Aoki, M.; Suzuki, S.; Miyatake, K.; Uchida, H.; Watanabe, M. Aliphatic/aromatic polyimide lonomers as a proton conductive membrane for fuel cell

applications. *J. Am. Chem. Soc.* **2006**, *128*, 1762–1769.

[43] Omata, T.; Tanaka, M.; Miyatake, K.; Uchida, M.; Uchida, H.; Watanabe, M. Preparation and Fuel Cell Performance of Catalyst Layers Using Sulfonated Polyimide Ionomers. *ACS Appl. Mater. Interfaces* **2012**, *4*, 730– 737.

[44] Miyahara, T.; Miyake, J.; Matsuno, S.; Watanabe, M.; Miyatake, K. A sulfonated polybenzophenone/polyimide copolymer as a novel proton exchange membrane. *RSC Adv.*, **2015**, 5, 50082–50086.

[45]Tamura, T.; Kawakami, H. Aligned Electrospun Nanofiber Composite Membranes for Fuel Cell Electrolytes. *Nano Lett.* **2010**, *10*, 1324–1328.

[46] Takemori, R.; Ito, G.; Tanaka, M.; Kawakami, H. Ultra-high proton conduction in electrospun sulfonated polyimide nanofibers. *RSC Adv*. **2014**, *4*, 20005−20009.

[47] Tamura, T.; Takemori, R.; Kawakami, H. Proton conductive properties of composite membranes containing uniaxially aligned ultrafine electrospun polyimide nano fiber. *Journal of Power Sources* **2012**, *217*, 135−141.

[48] Tonozuka, I. ;Yoshida, M. ;Kaneko, K. ;Takeoka, Y. ;Rikukawa, M. Considerations of polymerization method and molecular weight for proton-conducting poly(p-phenylene) derivatives. *Polymer* **2011**, *52*, 6020–6028.

[49] Oshima, T.; Yoshizawa-Fujita, M.; Takeoka, Y.; Rikukawa, M. Use of a

High-Performance Poly(p-phenylene)-Based Aromatic Hydrocarbon Ionomer with Superacid Groups in Fuel Cells under Low Humidity Conditions. *ACS Omega*, **2016**, *1*, 939–942.

[50]Kobayashi, T.; Rikukawa, M.; Sanui, K.; Ogata, N. Proton-conducting Polymers Derived from Poly(ether-etherketone) and Poly(4-phenoxybenzoyl-1,4-phenylene). *Solid State Ionics* **1998**, *106*, 219–225.

[51]Umezawa, K.; Oshima, T.; Yoshizawa-Fujita, M.; Takeoka, Y.; Rikukawa, M. Synthesis of Hydrophilic–Hydrophobic Block Copolymer Ionomers Based on Polyphenylenes. *ACS Macro Lett.* **2012**, *1*, 969–972.

[52]Takeoka, Y.; Umezawa, K.; Oshima, T.; Yoshida, M.; Yoshizawa-Fujita, M.; Rikukawa, M. Synthesis and Properties of Hydrophilic–Hydrophobic Diblock Copolymer Ionomers Based on Poly(p-phenylene)s *Polym. Chem.* **2014**, *5*, 4132–4140.

[53] Li, Q.; He, R.; Jensen, J. O.; Bjerrum, N. J. Fuel Cells PBI-Based Polymer Membranes for High Temperature Fuel Cells – Preparation, Characterization and Fuel Cell Demonstration. *Fuel Cells* **2004**, *4*, 147–159.

[54] Miyatake, K.; Chikashige, Y.; Higuchi, E.; Watanabe, M. Tuned Polymer Electrolyte Membranes Based on Aromatic Polyethers for Fuel Cell Applications. *J. Am. Chem. Soc.* **2007**, *129*, 3879–3887.

[55] Bae, B.; Yoda, T.; Miyatake, K.; Uchida, H.; Watanabe, M. Proton-Conductive Aromatic Ionomers Containing Highly Sulfonated Blocks for High-Temperature-Operable Fuel Cells. *Angew. Chem., Int. Ed.* 2010, *49*, 317–320.

[56] Li, N.; Wang, C.; Lee, S. Y.; Park, C. H.; Lee, Y. M.; Guiver, M. D. Enhancement of Proton Transport by Nanochannels in Comb-Shaped Copoly(arylene ether sulfone)s. *Angew. Chem., Int. Ed.* **2011**, *50*, 9158–9161.

[57] Miyake, J.; Mochizuki, T.; Miyatake, K. Effect of the Hydrophilic Component in Aromatic Ionomers: Simple Structure Provides Improved Properties as Fuel Cell Membranes. *ACS Macro Lett.* **2015**, *4*, 750–754.

[58] Miyahara, T.; Hayano, T.; Matsuno, S.; Watanabe, M.; Miyatake, K. Sulfonated Polybenzophenone/Poly(arylene ether) Block Copolymer Membranes for Fuel Cell Applications. *ACS Appl. Mater. Interfaces* **2012**, *4*, 2881–2884.

[59] Chang, Y.; Mohanty, A. D.; Smedley, S. B.; Abu-Hakmeh, K.; Lee, Y. H.; Morgan, J. E.; Hickner, M. A.; Jang, S. S.; Ryu, C. Y.; Bae, C. Effect of Superacidic Side Chain Structures on High Conductivity Aromatic Polymer Fuel Cell Membranes. *Macromolecules* **2015**, *48*, 7117–7126.

[60] Mochizuki, T.; Kakinuma, K.; Uchida, M.; Deki, S.; Watanabe, M.; Miyatake, K. Temperature- and Humidity-Controlled SAXS Analysis of Proton-Conductive Ionomer

Membranes for Fuel Cells. *ChemSusChem* **2014**, *7*, 729–733.

[61] Mochizuki, T.; Uchida, M.; Miyatake, K. Simple, Effective Molecular Strategy for the Design of Fuel Cell Membranes: Combination of Perfluoroalkyl and Sulfonated Phenylene Groups. *ACS Energy Lett.*, **2016**, *1* , 348–352.

[62] Miyanishi, S.; Fukushima, T.; Yamaguchi, T. Synthesis and property of semicrystalline anion exchange membrane with well-defined ion channel structure. *Macromolecules* **2015**, *48*, 2576–2584.

[63] Chang, Y.; Brunello, G. F.; Fuller, J.; Hawley, M.; Kim, Y. S.; Disabb-Miller, M.; Hickner, M. A.; Jang, S. S.; Bae, C. Aromatic ionomers with highly acidic sulfonate groups: acidity, hydration, and proton conductivity. *Macromolecules* **2011**, *44*, 8458–8469.

[64] Sato, T.; Hayasaka, Y.; Mitsuishi, M.; Miyashita, T.; Nagano, S.; Matsui, J.High Proton Conductivity in the Molecular Interlayer of a Polymer Nanosheet Multilayer Film. *Langmuir* **2015**, *31*, 5174–5180.

[65] Matsui, J.; Miyata, H.; Hanaoka, Y.; Miyashita, T.Layered Ultrathin Proton Conductive Film Based on Polymer Nanosheet Assembly. *ACS Appl. Mater. Interfaces* **2011**, *3* 1394–1397.

[66] Nagao, Y.; Matsui, J.; Abe, T.; Hiramatsu, H.; Yamamoto, H.; Miyashita, T.; Sata,

N.; Yugami, H. Enhancement of Proton Transport in an Oriented Polypeptide Thin Film. *Langmuir* **2013**, *29*, 6798–6804.

[67] Horike, S.; Umeyama, D.; Kitagawa, S. Ion Conductivity and Transport by Porous Coordination Polymers and Metal–Organic Frameworks. *Acc. Chem. Res.* **2013**, *46*, 2376–2384.

[68] He, G. W.; Chang, C. Y.; Xu, M. Z.; Hu, S.; Li, L. Q.; Zhao, J.; Li, Z.; Li, Z. Y.; Yin, Y. H.; Gang, M. Y.; Wu, H.; Yang, X. L.; Guiver, M. D.; Jiang, Z. Y. Tunable Nanochannels along Graphene Oxide/Polymer Core-Shell Nanosheets to Enhance Proton Conductivity. *Adv. Funct. Mater.* **2015**, *25*, 7502– 7511.

[69] Kobayashi, T.; Ichikawa, T.; Kato, T.; Ohno, H. Development of glassy bicontinuous cubic liquid crystals for solid proton-conductive materials. Adv. Mater. **2017**.

[70] Soberats, B.; Yoshio, M.; Ichikawa, T.; Taguchi, S.; Ohno, H.; Kato, T. 3D Anhydrous Proton-Transporting Nanochannels Formed by Self-Assembly of Liquid Crystals Composed of a Sulfobetaine and a Sulfonic Acid. *J. Am. Chem. Soc.* **2013**, *135*, 15286–15289.

[71] Ichikawa, T.; Kato, T.; Ohno, H. 3D Continuous Water Nanosheet as a Gyroid Minimal Surface Formed by Bicontinuous Cubic Liquid-Crystalline Zwitterions. *J. Am.*

Chem. Soc. **2012**, *134*, 11354–11357.

[72] Soberats, B.; Yoshio, M.; Ichikawa, T.; Zeng, X.; Ohno, H.; Ungar, G.; Kato, T. Ionic Switch Induced by a Rectangular-Hexagonal Phase Transition in Benzenammonium Columnar Liquid Crystals. J. Am. Chem. Soc. **2015**, *137*, 13212–13215.

[73] Soberats, B.; Uchida, E.; Yoshio, M.; Kagimoto, J.; Ohno, H.; Kato, T. Macroscopic Photocontrol of Ion-Transporting Pathways of a Nanostructured Imidazolium-Based Photoresponsive Liquid Crystal. J. Am. Chem. Soc. **2014**, *136* (27) 9552–9555.

[74] Hernandez, J.; Zhang, H.; Chen, Y.; Rosenthal, M.; Lingwood, M.; Goswami, M.; Zhu, X.; Moeller, M.; Madsen, L.; Ivanov, D. Bottom-Up Fabrication of Nanostructured Bicontinuous and Hexagonal Ion-Conducting Polymer Membranes. *Macromolecules*, **2017**, *50*, 5392–5401.

[75]Soberats, B.; Yoshio, M.; Ichikawa, T.; Zeng, X.; Ohno, H.; Ungar, G.; Kato, T. Ionic Switch Induced by a Rectangular-Hexagonal Phase Transition in Benzenammonium Columnar Liquid Crystals *J. Am. Chem. Soc.* **2015**, *137*, 13212–13215.

[76]Soberats, B.; Uchida, E.; Yoshio, M.; Kagimoto, J.; Ohno, H.; Kato, T. Macroscopic

Photocontrol of Ion-Transporting Pathways of a Nanostructured Imidazolium-Based Photoresponsive Liquid Crystal. *J. Am. Chem. Soc.* **2014**, *136*, 9552– 9555.

[77]Yoshio, M.; Kagata, T.; Hoshino, K.; Mukai, T.; Ohno, H.; Kato, T. One-Dimensional Ion-Conductive Polymer Films: Alignment and Fixation of Ionic Channels Formed by Self-Organization of Polymerizable Columnar Liquid Crystals. *J. Am. Chem. Soc.* **2006**, *128*, 5570–5577.

[78]Sakuda, J.; Hosono, E.; Yoshio, M.; Ichikawa, T.; Matsumoto, T.; Ohno, H.; Zhou, H.; Kato, T. Liquid-Crystalline Electrolytes for Lithium-Ion Batteries: Ordered Assemblies of a Mesogen-Containing Carbonate and a Lithium Salt. *Adv. Funct. Mater.* **2015**, *25*, 1206–1212.

[79]Ichikawa, T.; Kato, T.; Ohno, H. 3D Continuous Water Nanosheet as a Gyroid Minimal Surface Formed by Bicontinuous Cubic Liquid-Crystalline Zwitterions. *J. Am. Chem. Soc.* **2012**, *134*, 11354–11357.

[80]Soberats, B.; Yoshio, M.; Ichikawa, T.; Taguchi, S.; Ohno, H.; Kato, T. 3D Anhydrous Proton-Transporting Nanochannels Formed by Self-Assembly of Liquid Crystals Composed of a Sulfobetaine and a Sulfonic Acid. *J. Am. Chem. Soc.* **2013**, *135*, 15286–15289.

[81]Ichikawa, T.; Yoshio, M.; Hamasaki, A.; Taguchi, S.; Liu, F.; Zeng, X.; Ungar, G.;

Ohno, H.; Kato, T. Induction of Thermotropic Bicontinuous Cubic Phases in Liquid-Crystalline Ammonium and Phosphonium Salts. *J. Am. Chem. Soc.* **2012**, *134* 2634–2643.

[82] Nakai, T.; Tanaka, D.; Hara, M.; Nagano, S.; Seki, T. Free Surface Command Layer for Photoswitchable Out-of-Plane Alignment Control in Liquid Crystalline Polymer Films. *Langmuir* **2016**, *32*, 909–914.

[83] Sano, M.; Hara, M.; Nagano, S.; Shinohara, Y.; Amemiya, Y.; Seki, T. New Aspects for the Hierarchical Cooperative Motions in Photoalignment Process of Liquid Crystalline Block Copolymer Films. *Macromolecules* **2015**, *48*, 2217–2223.

[84]Bridges, C. R.; Ford, M. J.; Popere, B. C.; Bazan, G. C.; Segalman, R. A. Formation and Structure of Lyotropic Liquid Crystalline Mesophases in Donor-Acceptor Semiconducting Polymers. *Macromolecules* **2016**, *49*, 7220–7229.

[85]Rulkens, R.; Schulze, M.; Wegner, G. Rigid-rod polyelectrolytes: synthesis of sulfonated poly(p-phenylene)s. *Macromol. Rapid Commun*. **1994**, *15*, 669-1994

[86] Rulkens, R.; Wegner, G.; Enkelmann, V.; Schulze, M. Rigid-rod polyelectrolytes based on poly(p-Phenylene sulfonic acid). *Ber. Bunsenges. Phys. Chem.* **1996**, *100*, 707-714.

[87]Viale, S.; Best, A. S.; Mendes, E.; Picken, S. J. Formation of aqueous molecular

nematic liquid crystal phase in poly(p-sulfophenylene sulfoterephthalamide). *Chem. Commu.* **2005**, *12*, 1528–1530.

[88] Viale, S.; Best, A. S.; Mendes, E.; Jagaer, W. F.; Picken, S. J. A supramolecular nematic phase in sulfonated polyaramides. *Chem. Commu.* **2004**, *14*, 1596–1597.

[89] Chen, Y.; Lingwood, M. D.; Goswami, M.; Kidd, B. E.; Hernandez, J. J.; Rosenthal, M.; Ivanov, D. A.; Perlich, J.; Zhang, H.; Zhu, X.; Möller, M.; Madsen, L. A. Humidity-Modulated Phase Control and Nanoscopic Transport in Supramolecular Assemblies. *J. Phys. Chem. B* **2014**, *118*, 3207–3217.

[90] Zhang, H.; Li, L.; Möller, M.; Zhu, X.; Rueda, J. J. H.; Rosenthal, M.; Ivanov, D. A. From Channel-Forming Ionic Liquid Crystals Exhibiting Humidity-Induced Phase Transitions to Nanostructured Ion-Conducting Polymer Membranes. *Adv. Mater.* **2013**, *25*, 3543–3548.

[91] Zhu, X.; Scherbina, M. A.; Bakirov, A. V.; Gorzolnik, B.; Chvalun, S. N.; Beginn, U.; Möller, M. Methacrylated Self-Organizing 2,3,4-Tris(alkoxy)benzenesulfonate: A New Concept Toward Ion-Selective Membranes. *Chem. Mater.* **2006**, *18*, 4667–4673.

Chapter 2.
Interfacial Structure and Proton Conductivity of Nafion thin film at the Pt-deposited Surface

Abstract

Understanding the Nafion-Pt interface structure is important because fuel cell reactions occur at the three-phase boundary. Infrared (IR) p-polarized multiple-angle incidence resolution spectrometry (pMAIRS) technique was used to investigate the in-plane (IP) and out-of-plane (OP) spectra in the identical substrate. Proton conductivity of the Nafion thin films decreased at the MgO and SiO_2 surfaces. The origin for the lower proton conductivity can be proposed because of a highly oriented structure at the interface. However, the interface structure of the Nafion-Pt interface remains unclear. In this study, Nafion thin films were prepared by spin-coating on a Pt-deposited MgO substrates. The IP spectrum exhibited a well-known spectrum, but the OP spectrum was quite differed considerably from the IP spectrum. Furthermore, thickness dependence of the degree of orientation for this OP band was observed at the Nafion-Pt interface. This OP band can be assigned as the vibration mode of the mixture of the CF_2 and sulfonic acid groups. At the low-RH region, proton conductivity of the Nafion thin film on the Pt-deposited surface was one order of magnitude higher than that on the SiO_2 surface.

Furthermore, the activation energy was 0.4–0.5 eV, which is lower than that of the SiO_2 surface. These results, which suggest that the Pt surface influenced the proton transport property of Nafion thin film, can contribute to understand the relationship between the proton transport property and thin film structure on the Pt-deposited surface at the three-phase boundary for fuel cells.

2-1. Introduction

Polymer electrolyte fuel cells (PEFCs), which are anticipated for use as a next-generation power source, have been investigated extensively for use in energy conversion for automotive, portable device and other applications. The membrane electrode assembly (MEA) comprises a catalyst layer and the electrolyte membrane. Understanding this interface has become necessary because reactions occur at the three-phase boundary of a proton conductive ionomer, catalyst (Pt or Pt alloy), and gas. Therefore, the structure and properties of the materials at the interface must be elucidated [1]. Some reports have described that the interfacial confinement of polymer electrolyte structure strongly affects the proton transport property [2–6].

Nafion, the most well-known and widely studied ionomer developed by DuPont, has high proton conductivity in addition to excellent thermal and chemical stability [7]. The chemical structure of Nafion consists of a hydrophobic polytetrafluoroethylene (PTFE)

backbone with perfluorinated ether side chains terminated by hydrophilic sulfonic acid groups, as shown in Scheme 2-1.

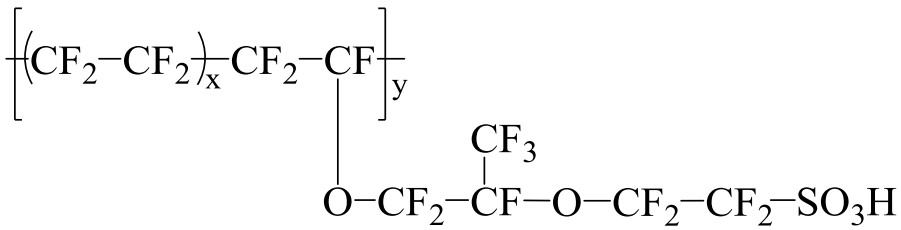

Scheme 2-1. Nafion structure.

The structure in commercial bulk Nafion membrane has been investigated thoroughly using small-angle X-ray scattering technique [8–11]. A phase segregation structure in hydrated Nafion has been reported. Moreover, Nafion is used in a dispersion state with various solvents for the preparation of MEA. The ideal ionomer layer in the MEA is regarded as extremely thin [12,13]. Paul *et al*. have reported the properties of ultrathin Nafion films [14–17]. The structure and properties of bulk Nafion membranes have been investigated widely in several studies described the literature, but the character of its confined thin film in the catalyst layer is still not well understood.

Several studies of Nafion thin films have been reported on the structure, water uptake, proton transport, and other characteristics. Neutron reflectivity (NR) [18–22], grazing incidence small-angle X-ray scattering (GI-SAXS) [23–27], and X-ray specular reflectivity (XRR) [28] techniques have revealed the effects of confinement and

substrates. The NR study has revealed a lamellar structure between the SiO_2 substrate and Nafion thin film [19]. Moreover, a single hydrated layer appeared at the metal interface such as Pt and Au surfaces [18, 19]. Surface hydrophilicity and the water–vapor interface contributed to the structure of the Nafion surface [23, 24]. Results of another GI-SAXS study have demonstrated that the degree of the phase segregation losses with decreasing the thickness [26]. Furthermore, Kusoglu *et al.* reported that the annealed films also exhibit the loss of microphase segregation [27]. Our previous studies conducted using infrared (IR) p-polarized multiple-angle incidence resolution spectrometry (pMAIRS) technique [29, 30], which had been developed by Hasegawa [31–34], revealed the highly oriented molecular structure of Nafion thin films on both MgO(100) and Si wafer.

Some studies of proton transport have reported a decrease of the proton conductivity with decreasing thickness [16, 26, 30, 35], Moreover, proton conductivity has been described as quite lower than that of the commercial bulk Nafion membrane [15, 30]. Recent investigations have revealed that the hydrophilicity at the surface of Nafion ultrathin films is altered drastically by annealing, with conductivity changed by around one order of magnitude according to relative humidity [17].

Systematic analyses have examined the relationship between the structure and the proton conductivity of Nafion thin films. However, the relation between the interfacial behavior and proton transport property is not understood completely. For example, the different interfaces suggest the results of different water uptake [26, 27, 36–38]. Kongkanand reported that water uptake decreases concomitantly with decreasing the film thickness [36]. In contrast, Dishari *et al.* reported that the thin film at the SiO_2 interface had higher water uptake than thicker films [38]. These results suggest that the effects of the interface cannot be neglected. Bass *et al.* reported the surface hydrophilicity dependence of the micelle orientation [24]. However, proton conductivity has not been reported for the different interfacial conditions.

For use in fuel cell operations, the structure of confined Nafion thin films on a Pt surface has not been investigated sufficiently. As described herein, IR pMAIRS technique was conducted to investigate the molecular structure of the Nafion thin films on Pt-deposited surface (Figure 2-1.). IR pMAIRS is increasingly regarded as a powerful spectroscopic tool for revealing molecular orientation in thin films. The pMAIRS analysis showed that in-plane (IP) and out-of-plane (OP) transition dipoles are distinguishable in an identical infrared transparent substrate. However, because Pt is not transparent for IR light, this study prepared an ultrathin Pt-deposited surface on the

transparent substrate for pMAIRS. This ultrathin Pt-deposited surface has enabled the measurement of proton conductivity because the electronic conductivity of the ultrathin Pt-deposited surface is lower than the proton conductivity of the Nafion thin film. This result can help to understand the relation between the proton transport property and the thin film structure on the Pt-deposited surface at the three-phase boundary for fuel cells.

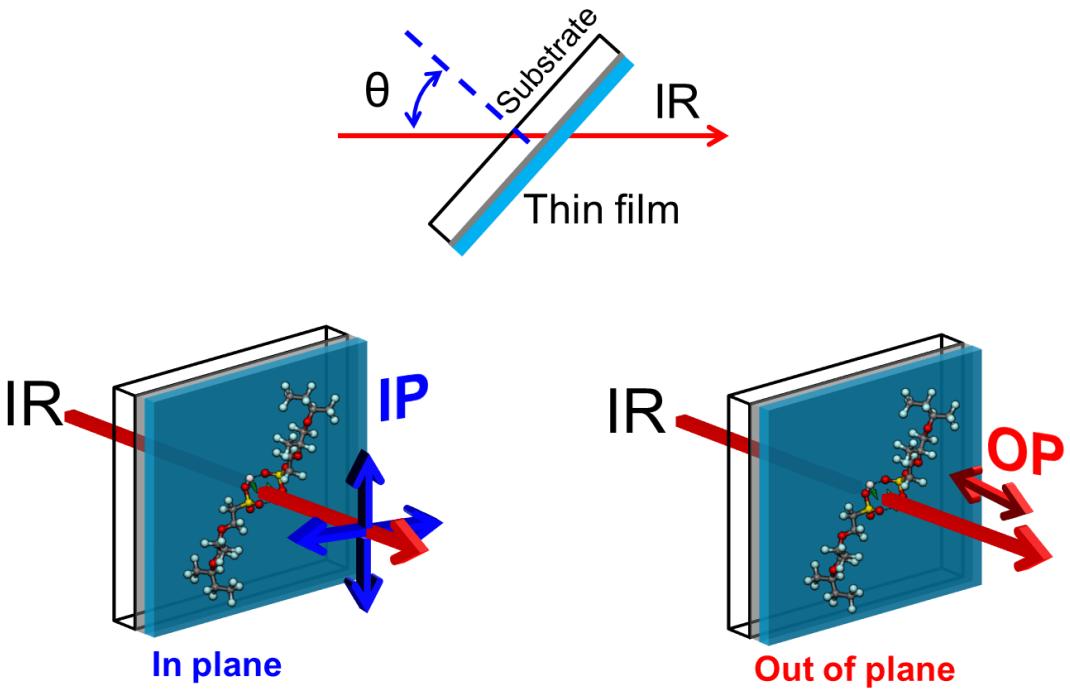

Figure 2-1. AFM image of the cross-section of Pt/SiO_2 surface

2-2. Experimental

2-2-1. Nafion Thin Film Preparation on Pt Modified Surface

For this study, MgO (Furuuchi Chemical Industries Corp., Japan) and SiO_2 substrates

(each 15 × 15 × 0.5 mm; Sendai Sekiei Co. Ltd.) were used respectively for IR and proton conductivity measurements. This study examined the relation between the thin film structure and proton conductivity on the Pt-deposited surfaces that had been prepared on each substrate using radio frequency (RF) magnetron sputtering system (KXS-110; Kenix Co. Ltd.). First, Pt-deposited surfaces were prepared by RF sputtering of a pure platinum (99.99%, Kojundo Chemical Laboratory Co. Ltd.) metal target. The RF power was applied, 20 W and 15 W respectively to MgO and SiO_2 substrates. Deposition was done in 20 s at room temperature with an Ar atmosphere. To obtain thin film thickness of Pt layer, deposition parameters were optimized. The thickness of the Pt-deposited layer was c.a. 15–20 nm (Figure 2-2), determined using atomic force microscopy (AFM, VN-8000; Keyence Co.).

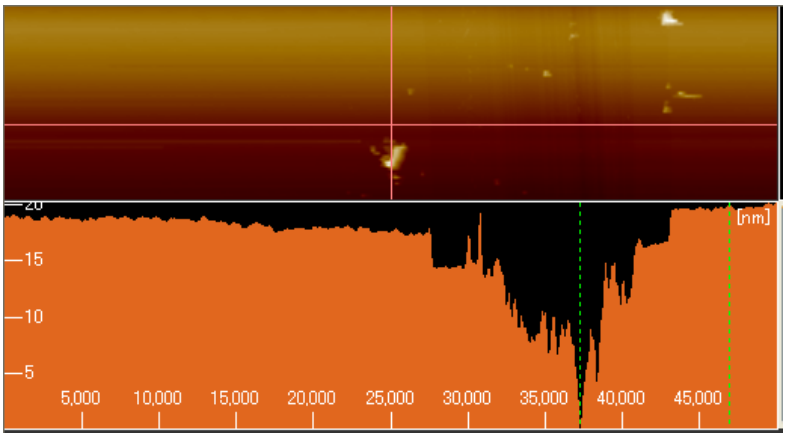

Figure 2-2. AFM image of the cross-section of Pt/SiO_2 surface

The Pt-deposited surface was characterized using X-ray photoelectron spectroscopy (XPS, AXIS-ULTRA DLD; Shimadzu Corp.). Energy calibration and component

separation were conducted using the bundled software with Gaussian profile. As a reference, MgO and SiO_2 substrates were used without Pt deposition. Before using them, plasma cleaning (Cute-MP; Femto Science, Korea) was conducted for a 10 sec.

For thin film preparation by spin-coating (ACT-200; Active Co. Ltd.), 5 % Nafion dispersion (DE521 CS type; Wako Pure Chemical Industries Ltd.) was used. Thicknesses of 20–400 nm were found using a surface profiler (P-15; KLA-Tencor Corp.). The thickness was controlled by adjustment of the Nafion solution concentration using ethanol and water. The Nafion thin films were dried for at least 12 hr in a desiccator.

2-2-2. Infrared (IR) p-polarized Multiple-angle Incidence Resolution Spectrometry (pMAIRS)

To investigate IP and OP molecular vibrations in an identical thin film, the IR pMAIRS technique was performed. The pMAIRS measurements were taken using an FT-IR spectrometer (Nicolet 6700; Thermo Fisher Scientific Inc.) equipped with a mercury–cadmium–telluride (MCT) detector. The optical configuration is shown in Figure 2-3. To obtain the p-polarized light, a ZnSe polarizer was used. Single-beam spectra were collected from 38° through 8° in 6° steps between the angles of incidence. The wavenumber resolution was 4 cm^{-1}. The number of scans was 64 for each angle of

incidence. Dry air or N_2 gases passed through the sample compartment and inside of the spectrometer for air purge. The humidity of the sample compartment was less than 5% under room temperature. The aperture was fully opened (size of 150). A metal plate with small pores was placed in the light path of the incidental beam to prevent saturation. The pMAIRS analysis from the collected spectra was conducted automatically using pMAIRS analyzer software (Thermo Fisher Scientific Inc.).

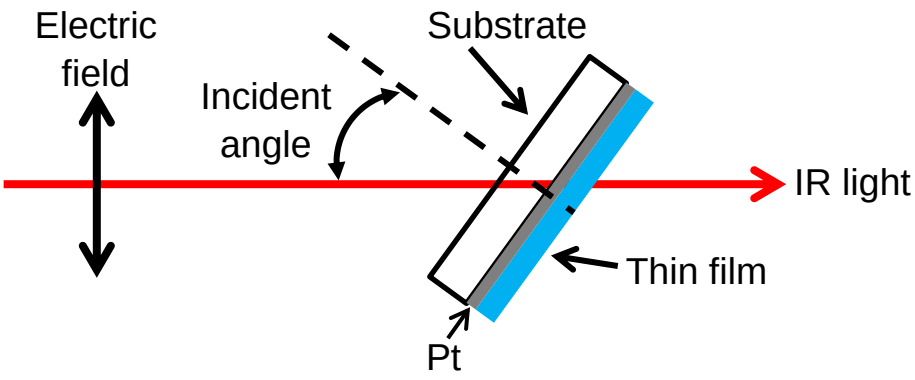

Figure 2-3. Configuration of the polarized incident beam path and incident angle.

2-2-3. Proton Conductivity Measurement of the Nafion Thin Films

The proton conductivity of thin films was measured at relative humidity (RH) range of 40–95% and temperature of 298–333 K using an impedance / gain-phase analyzer (SI1260; Solartron Analytical) with a dielectric interface system (SI1296; Solartron Analytical) with humidity-controlled and temperature-controlled chamber (SH-221; Espec Corp). Measurements were taken parallel to the substrate. The Au electrodes were fabricated at the edge of thin film. The impedance data were collected at the frequency range of 10 MHz and 1 Hz with amplitude of 50 mV. Proton conductivity (σ) was calculated as follows,

$$\sigma = \frac{d}{Rlt} \qquad (1)$$

where d is the distance between the Au electrodes, R is the resistance value from impedance, l and t are the length of the contact electrodes and thickness of the film respectively.

The typical impedance response of Nafion thin films is comprised of a semicircle and slant line response. The thin film resistance value (R) was determined by the point of the intersection of a semicircle with real axis at the complex impedance plots.

.

2-2-4. DFT Calculations

For the attribution of IR spectra, density functional theory (DFT) calculations were performed using the DMol3 package in Materials Studio (Accelrys Software Inc.). The Perdew−Burke−Ernzerhof (PBE) function was chosen. Convergence threshold for the maximum force and maximum displacement for normal geometry optimization were set respectively to 0.004 Ha $Å^{-1}$ and 0.005 Å.

2-3. Results and Discussion

The pMAIRS technique has never been applied to the Pt-deposited surface. To confirm the validity of the pMAIRS technique using a Pt-deposited surface on the MgO substrate, a validity check was carried out according to the literature [33]. Figure 2-4 shows the single-beam spectra with different incident angles.

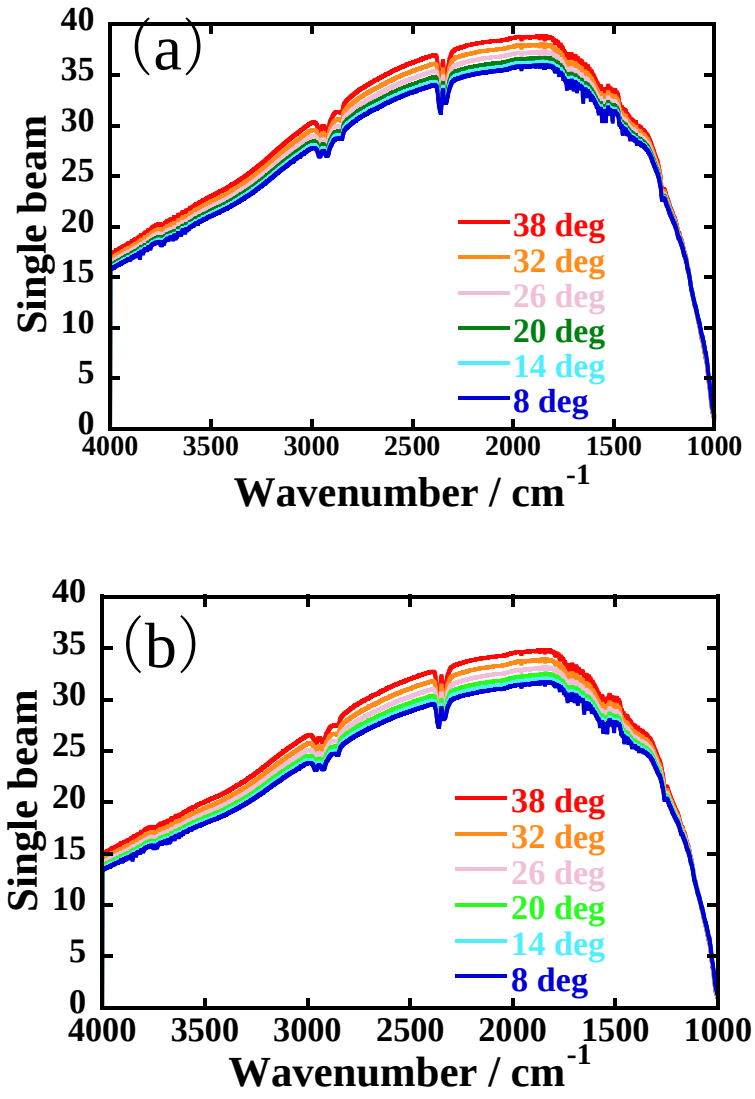

Figure 2-4. Single beam spectra of different angle and Transmission spectrum. (a) MgO substrate (b) Pt-deposited MgO surface.

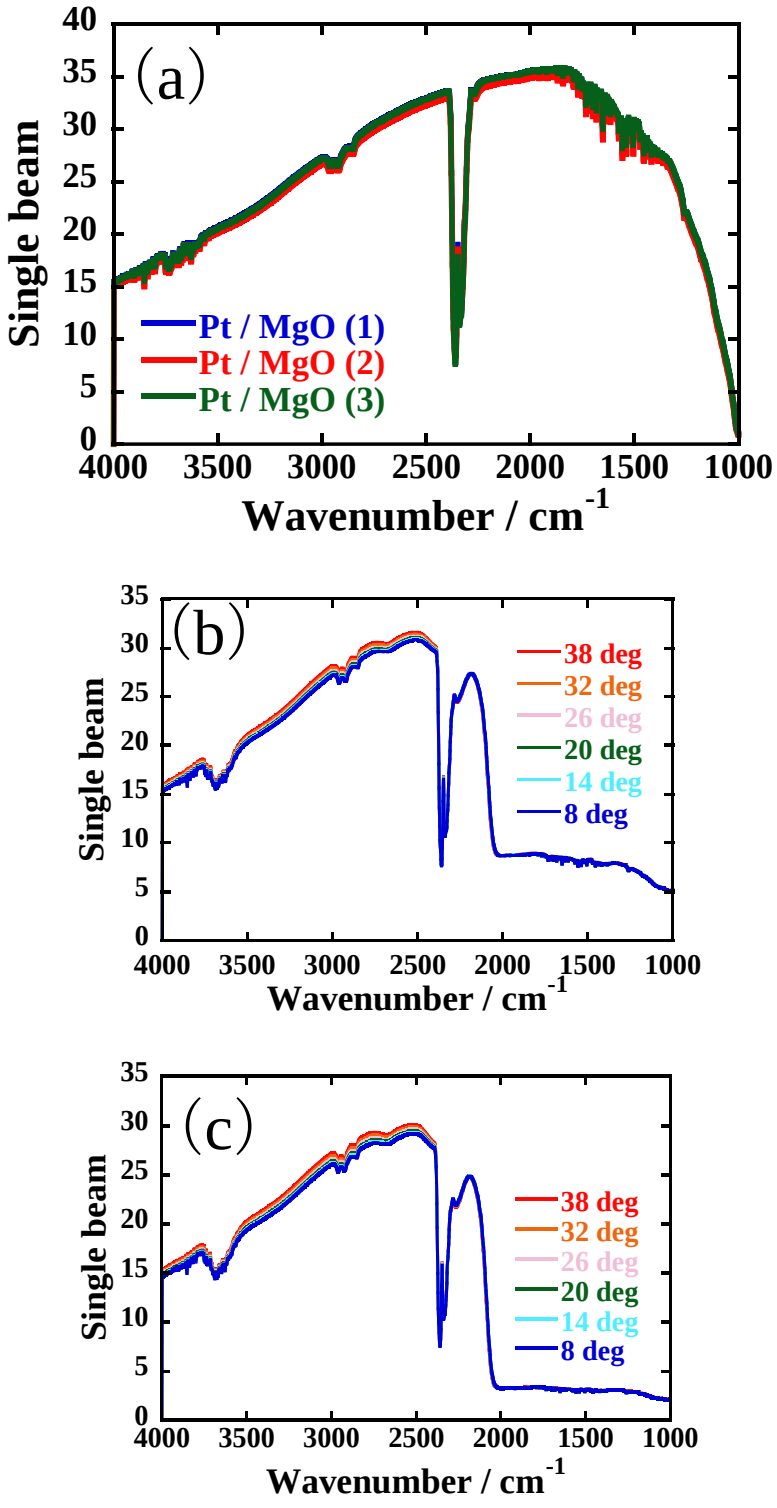

Figure 2-5. Single beam spectra of different angle (a) Pt-deposited MgO surface for three different samples at 38 degree (b) SiO_2 substrate (c) and Pt deposited SiO_2 surfaces.

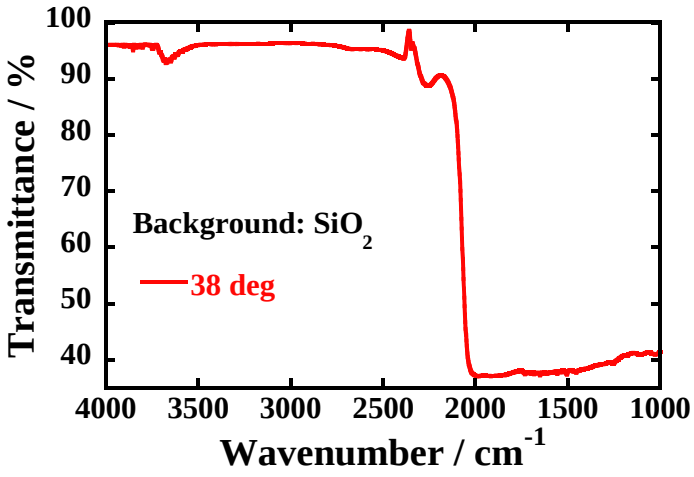

Figure 2-6. Transmission spectrum for Pt-deposited SiO_2 surface at the incident angle of 38 degree.

The intensity of the single-beam in the case of thicker Pt-deposited substrate was almost zero. However, the intensity for the thin Pt-deposited MgO (Figure 2-4(b)) was only 10% lower than that of the bare MgO substrate (Figure 2-4(a)). Each spectrum had a similar shape in the case of Pt-deposited and bare MgO substrates. The intensity of the single-beam spectra gradually decreased when the angle of incident decreased from 38° to 8°. Therefore, it is inferred that this pMAIRS technique is applicable with the Pt-deposited surface. To confirm the reproducibility for Pt deposition, Figure 2-5(a) shows the Pt-deposited MgO surface of three samples at 38°. Three samples show similar spectra. The single-beam spectra of the SiO_2 showed different spectra compared to the MgO substrate, because SiO_2 has low IR transmittance (Figure 2-5 (b)) as a result of the large absorption band at less than ca. 2100 cm^{-1}. The intensity from 4000 to 2200

cm^{-1} for ₹ thin Pt-deposited SiO_2 (Figure 2-5(c)) was a 4–10 % decrease compared with the bare SiO_2 substrate (Figure 2-6). This value is approximately equal to that of the Pt-deposited MgO.

Pt, an electroconductive material, the direction used for the impedance measurement is parallel to the Pt-deposited surface. For thick Pt thin film, proton conductivity cannot be measured because the resistance of Pt and Nafion thin films should be regarded as a parallel circuit. Therefore, a thin Pt-deposited surface is necessary to evaluate proton conductivity. Figure 2-7 shows the RH dependence of the resistance of Pt-deposited surface on the SiO_2 substrate.

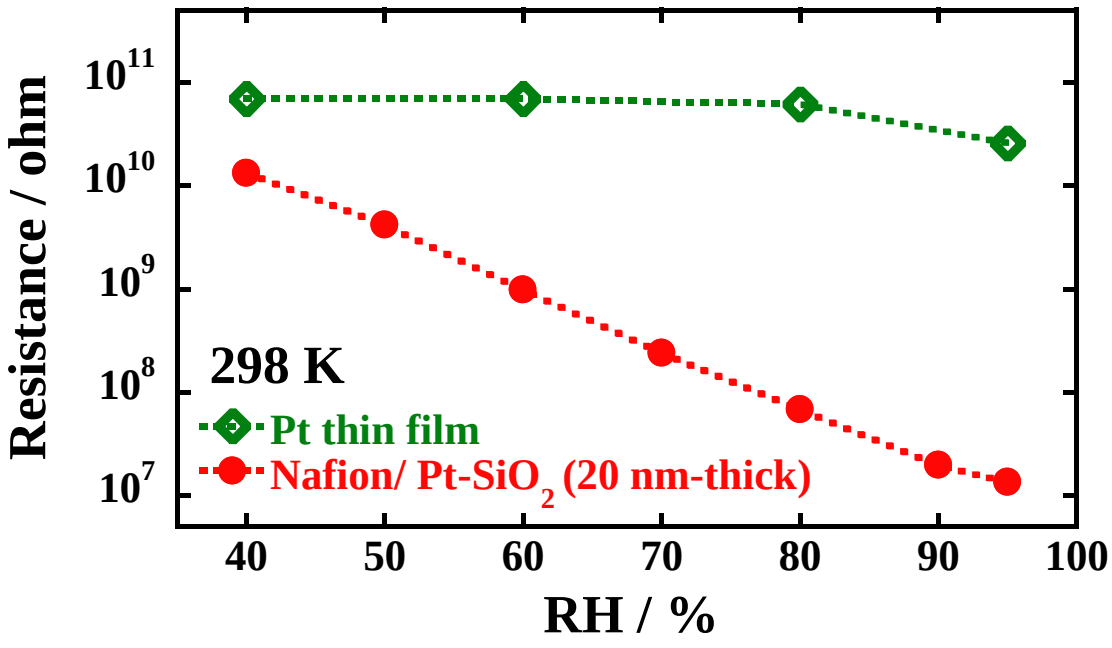

Figure 2-7. Humidity dependence (RH) of the resistance obtained directly from the impedance measurement.

The resistance of the Pt-deposited surface was found to be independent of the RH: it was 10^{11} ohm. In contrast, the resistance of the 20-nm-thick Nafion thin film deposited on Pt / SiO_2 substrate was strongly dependent on the RH. The resistance of the Pt-deposited surface was one order of magnitude higher than that of the Nafion thin films in the whole RH region. Therefore the proton conductivity can be evaluated in comparison to the Pt electronic conductivity. Two reasons for the higher resistance of the Pt-deposited surface are considered: the thin Pt-deposited surface is oxidized; alternatively, Pt is an island structure rather than a smooth thin film. To assess these possibilities, XPS was used. Figure 2-8 shows XPS spectra of Pt 4f and Si 2p electrons for the Pt / SiO_2 surface. The binding energies of Pt $4f_{7/2}$, $4f_{5/2}$ electron peaks were found respectively to be 71.5 eV and 74.7 eV. These values show good agreement with those of Pt $4f_{7/2}$, $4f_{5/2}$ electron peaks that have been reported in the literature [39]. The oxidation state of Pt 4f peaks was observed in curve-fitted XPS spectra (Figure 2-9). The relative peak areas were, respectively, ca. 25% (Pt^{+2} $4f_{5/2}$) and 75% (Pt^{+0} $4f_{5/2}$), respectively (Table 2-1). This result suggests that the Pt-deposited surface was partially oxidized. The Si 2p electron peak can be assigned as SiO_2. It can be supposed that the Pt-deposited surface has an island shape on the SiO_2 substrate. This result suggests that the Pt-deposited surface was partially oxidized.

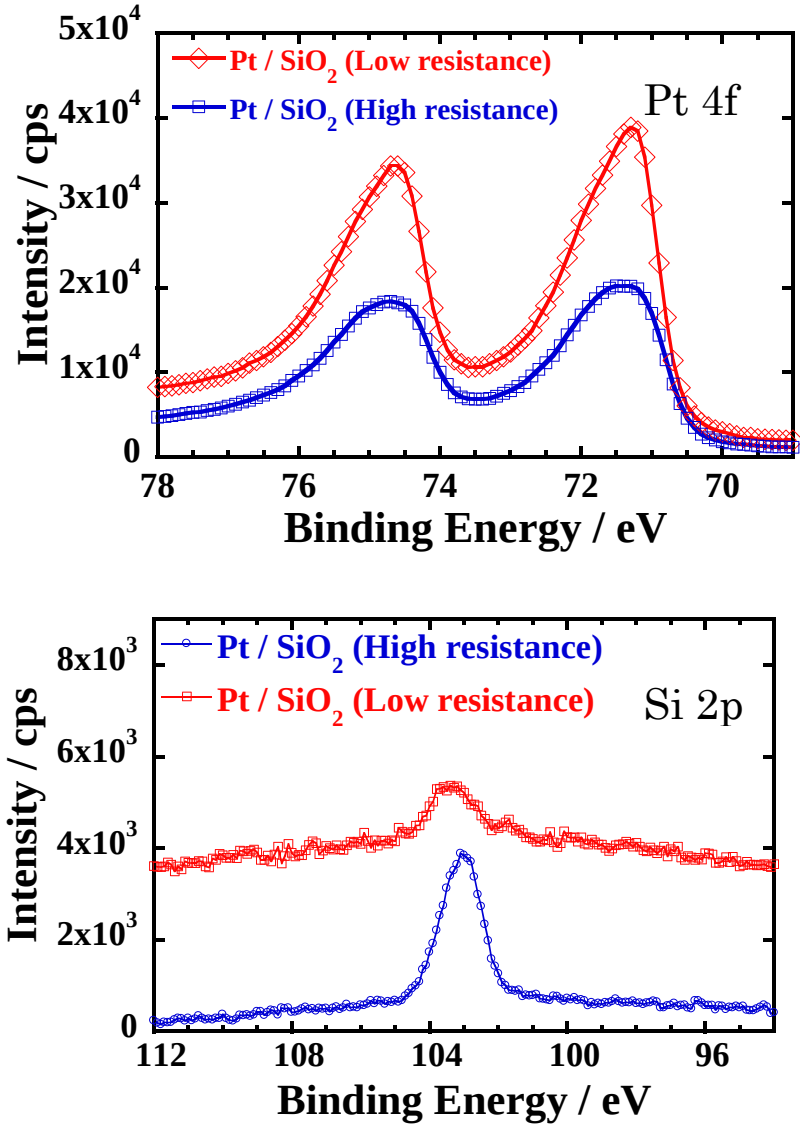

Figure 2-8. XPS spectra of Pt 4f and Si 2p electrons from Pt / SiO_2 substrate.

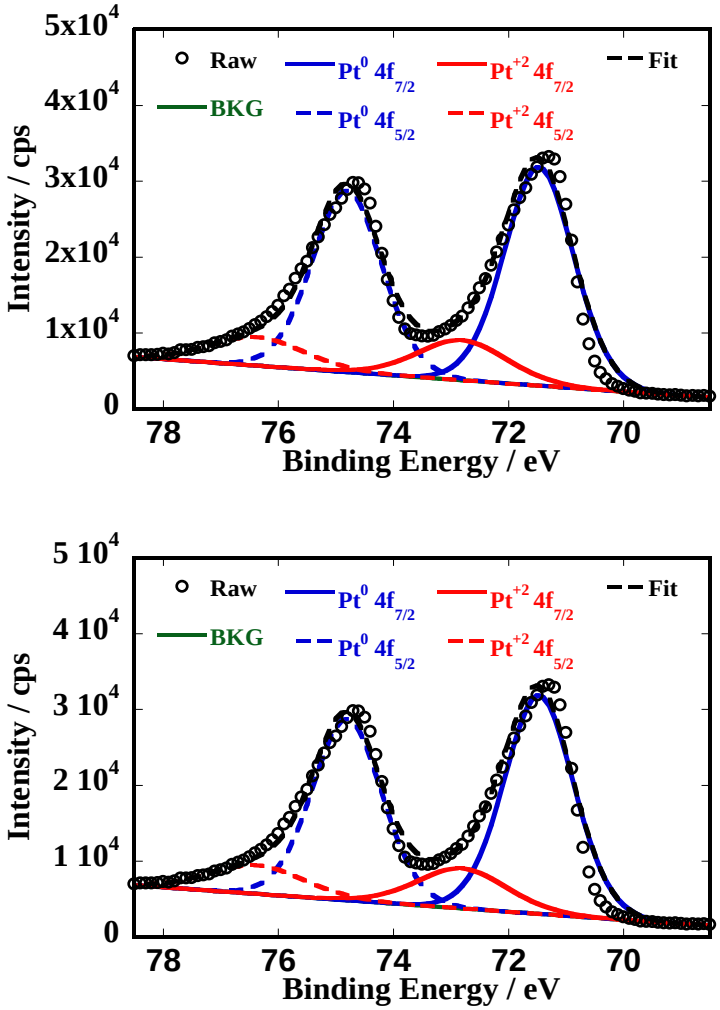

Figure 2-9. Curve-fitted XPS spectra for the Pt 4f core binding energy region of (a) Low, (b) High resistance.

Table 2-1. Relative peak area from curve-fitted XPS spectra.

	$Pt^{+0}\,4f_{5/2}$	$Pt^{+2}\,4f_{5/2}$
(a)	85 %	15 %
(b)	75 %	25%

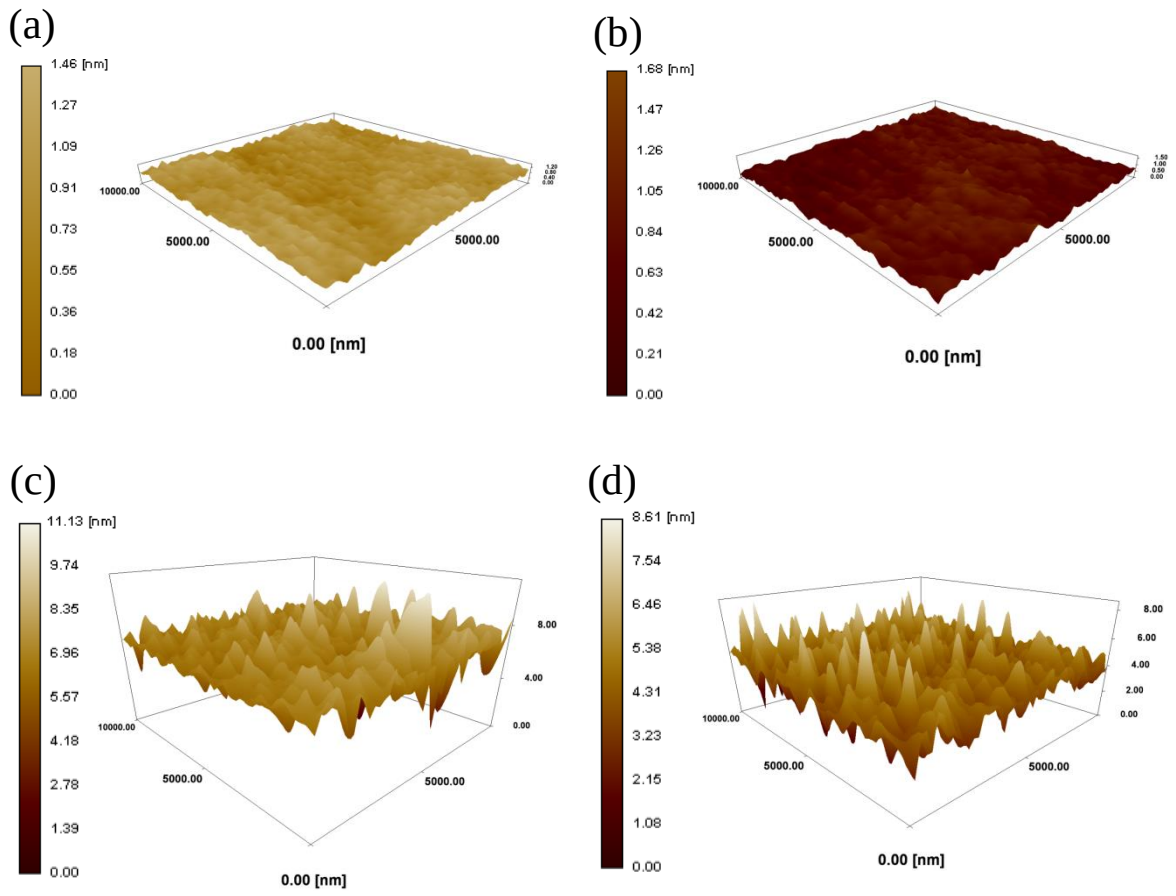

Figure 2-10. Dynamic force mode (DFM) of atomic force microscope (AFM) images of the bare surface and Pt-deposited surface: (a) MgO (b) SiO_2 (c) Pt / MgO (d) Pt / SiO_2 surface.

The surface morphology of the bare surface and Pt-deposited surface was obtained using AFM. Figure 2-10 shows topographic AFM images of the bare surface and Pt-deposited surface. Each image shows a 10 μm × 10 μm area of the surface. The smooth surface images were obtained respectively from bare MgO and SiO_2 surfaces in Figure 2-10(a) and (b), respectively. In contrast, rougher surfaces compared to bare surface were observed in both Pt-deposited MgO and SiO_2 surfaces, as shown in Figure 2-10(c) and (d). These results support that the Pt-deposited surface has island morphology on both substrates. Figure 2-11 shows the incident angle dependence of the transmission IR spectra of the 300-nm-thick Nafion film on the Pt-deposited surface. The absorbance around 1260 cm^{-1} depended on the incident angle. This result suggests that the thin film has an oriented structure. For a low incident angle, the peak around 1260 cm^{-1} was not observed, which suggests that the IP transition dipole moment does not have so much. The shoulder peak appeared gradually with the incident angle, meaning that OP transition dipole moments were excited by polarized light.

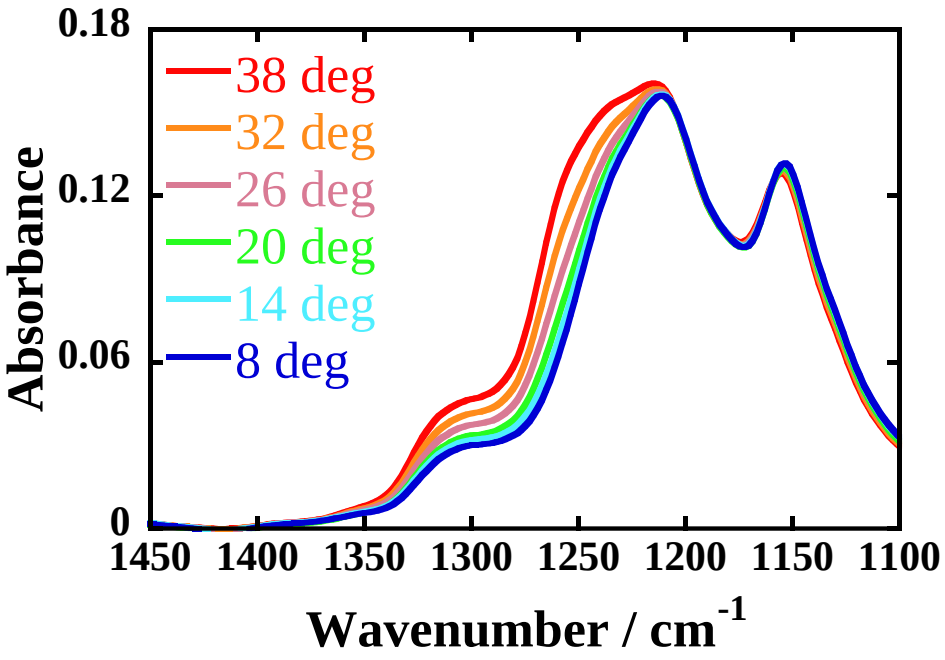

Figure 2-11. Incident angle dependence of the transmission IR spectra of the 300-nm-thick Nafion film on the Pt-deposited surface.

To discuss the details of the molecular orientation, pMAIR spectra after the collection of single-beam spectra are shown in Figure 2-12. The Nafion membrane consists of a hydrophobic PTFE backbone with perfluorinated ether side chains terminated by hydrophilic sulfonic acid groups. The IP spectrum shows the well-known spectrum of Nafion membrane [40, 41]. The bands at 1150 and 1210 cm^{-1} are assigned respectively to $\nu_s(CF_2)$ and $\nu_{as}(CF_2)$. The shoulder band at 1300 cm^{-1} is assigned to $\nu_{as}(CF_3)$. These vibration modes can be observed in the IP spectrum. However, the OP spectrum differed greatly from the IP spectrum. The characteristic absorption band at 1260 cm^{-1} was observed only in the OP spectrum. Many investigations of IR spectra have been

conducted using commercial Nafion films with several hundred or tens of micrometer order thickness. Two groups have reported this peak located at 1260 cm^{-1} experimentally by polarization modulation infrared reflection absorption spectroscopy (PM-IRRAS) [42, 43]. They assigned different attributions of the band at 1260 cm^{-1} as ν (CF_2) [42] and ν_{as} (CF_3) + δ_s (COC) [43] vibration mode, respectively. Zeng *et al.* assigned ν_{as} (CF_3) vibration mode at the 1269 cm^{-1} in the Raman spectra [44]. Malevich *et al*. and Korzeniewski *et al*. assigned attributions of the band at 1250–1350 cm^{-1} and 1249–1275 cm^{-1} as $–SO_3^-$ from a deconvoluted IR spectrum [45, 46]. In our previous report, this IR band at 1260 cm^{-1} was attributed to $–SO_3H$ vibration modes between the two sulfonic acid groups with hydrogen bonds by the DFT calculation [30]. Similar calculation results have been reported by another group [47]. Their calculations suggest that the dimer structure of triflic acid shows absorption near the 1260 cm^{-1}. They assigned this band as SOH in-plane bending vibration mode. Furthermore, Warren and McQuillan assigned the measured band at 1255–1289 cm^{-1} as sulfonic acid groups of perfluoro(2-ethoxyethane) sulfonic acid [48]. For further consideration the attribution of this band, DFT calculations were conducted as a modified model. Figure 2-13 shows a perfluorinated sulfonic acid as a model compound of Nafion for DFT calculation. This study employed the new model based on the Nafion equivalent weight with a longer

backbone than that described in the previous report. Vibration analysis was performed after geometry optimization. In the previous calculation with the short main chain of perfluorinated sulfonic acid, the band at 1260 cm^{-1} had not been suggested [30]. However, the CF_2 mode around 1260 cm^{-1} was suggested in this work using the longer main chain. Therefore, the band at 1260 cm^{-1} can be assigned as the vibration modes of the mixture of the CF_2 and sulfonic acid groups. That abrupt conclusion for this attribution seems inappropriate: further investigation is needed for this attribution. The peak at 1060 cm^{-1} [49], which corresponds to sulfonic acid group, is helpful for this attribution. However, this IR region cannot be discussed because of IR absorption by the MgO substrate.

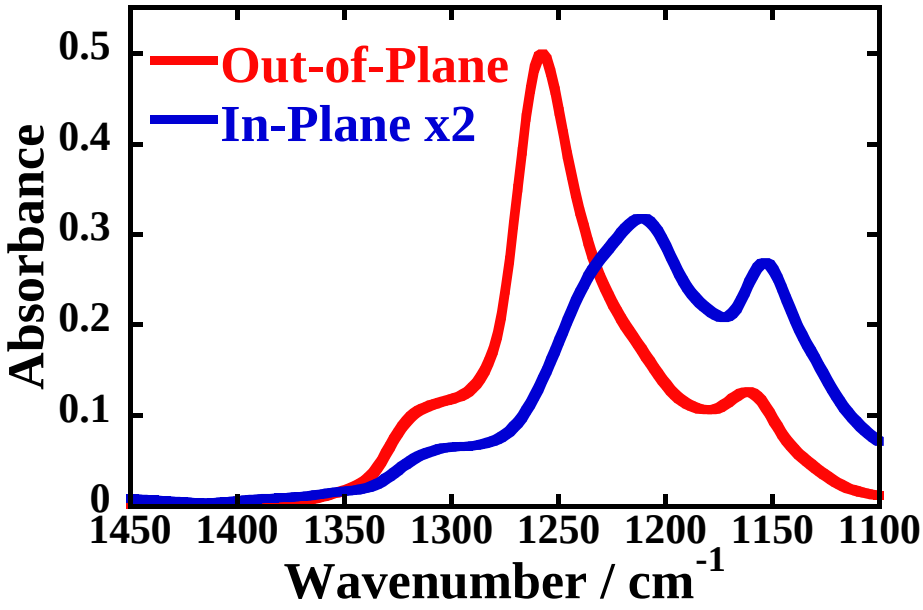

Figure 2-12. IR pMAIRSpectra of 300-nm-thick Nafion thin film on the Pt-deposited surface.

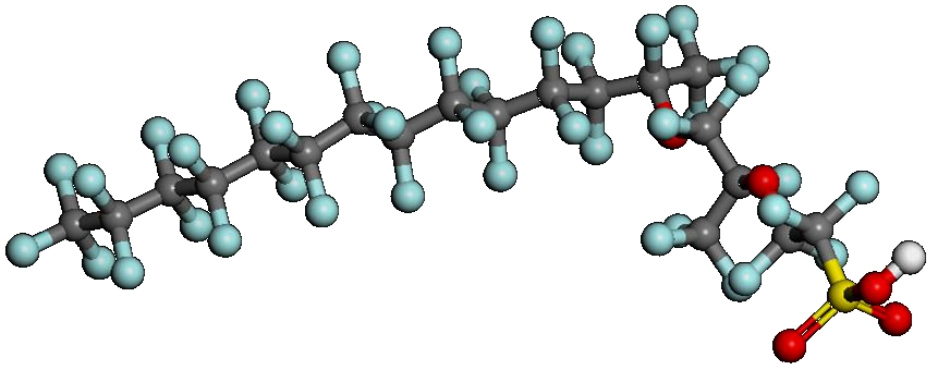

Figure 2-13. Nafion-like model for DFT calculation: carbon (gray), fluorine (light blue), oxygen (red), sulfur (yellow), and hydrogen (white).

Some literatures describe the thickness dependence by other measurements in the confined Nafion thin films. The proton conductivity [16, 26, 29, 35], water uptake [26, 27, 36–38], and degree of hydrophilicity depend on the thickness [14]. The thin film

thickness may affect the interface structure. To investigate the interface structure of the confined Nafion thin films on the Pt-deposited surface, Figure 2-14 shows the thickness dependence of the oriented structure on the Pt-deposited surface. The absorbance of the band at 1260 cm^{-1} depends strongly on decreasing thickness and decreases along with it.

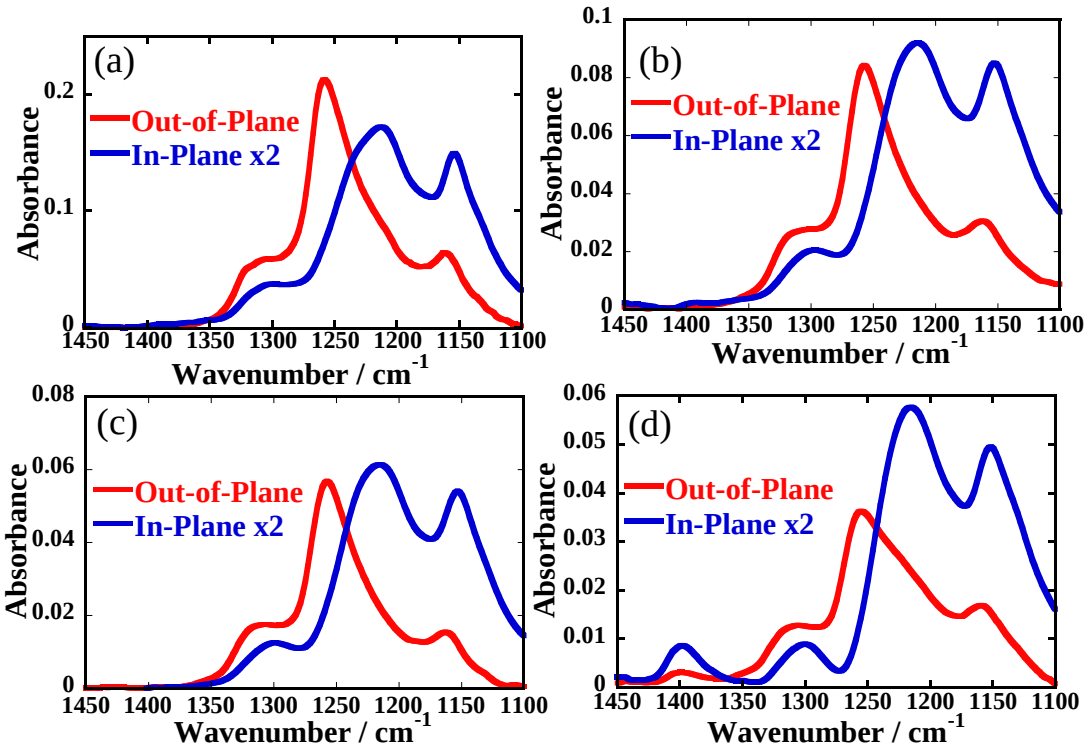

Figure 2-14. IR pMAIRSpectra of a Nafion thin film on the Pt-deposited surface. The thickness of Nafion thin films is (a)170 nm, (b)80 nm, (c)50 nm, and (d)35 nm thick.

Figure 2-16 depicts the thickness dependence of relative intensity ratios based on the strongest bands located at 1260 cm^{-1} (OP) and 1215 cm^{-1} (IP). The relative intensity ratio is calculated as follows,

$$Intensity\ ratio\ = \frac{I_{OP}(1260\ cm^{-1})}{I_{IP}(1215\ cm^{-1})} \qquad (2)$$

where I_{OP} and I_{IP} are derived from peak absorbance of IR pMAIRSpectra. The threshold was observed around 50–70 nm for the case of the Pt-deposited surface. The thin film structure changes drastically at this region of the thickness. A few literatures are available for the discussion between Pt and sulfonic acid groups [27, 44, 50, 51]. The possibility of a contribution by the difference of the surface morphologies between the Pt-deposited surface and MgO cannot be excluded based on our experiments results. And no apparent surface-enhanced IR effect was observed. Additional information for the thin film structure can be considered at 1400 cm^{-1}. A new peak appeared for 35-nm-thick Nafion thin films on the Pt-deposited surface. This new peak can be assigned as (S=O) of the SO_3H [49]. Our model compound of Nafion also suggests the S=O and S-OH stretching modes of the -SO_3H groups at 1400 cm^{-1}. The dissociation state of the -SO_3H groups depends on the thickness. Although the proton of -SO_3H groups in the thicker thin film is dissociated, the proton of -SO_3H groups at the interface on the Pt-deposited surface is not dissociated in the dry atmosphere. The dissociation state might derive from the structure. Thickness dependence has not been discussed for the previous report by the MgO substrate [29]. Figure 2-15 shows the thickness dependence of the pMAIR spectra.

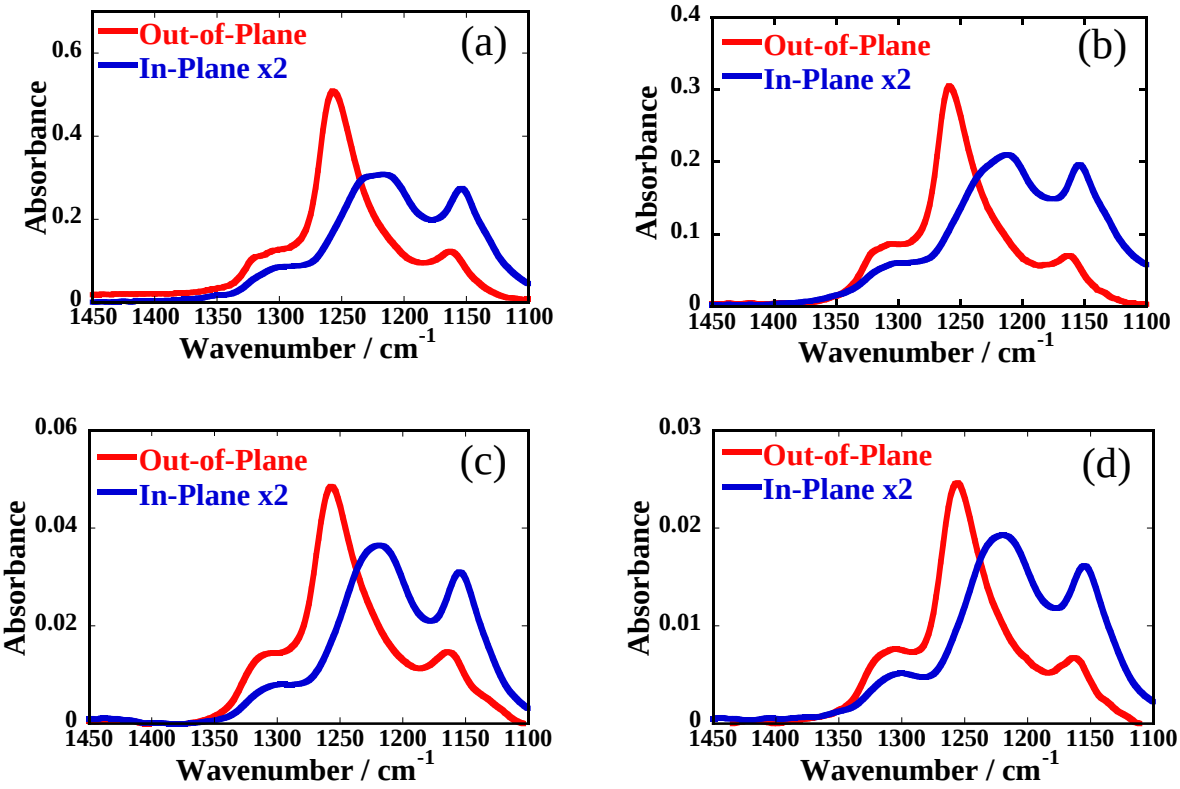

Figure 2-15. IR pMAIR spectra of a Nafion thin film on the MgO surface. The thickness of Nafion thin films is (a)400 nm, (b)250 nm, (c) 30 nm, (d)20-nm-thick.

The absorbance did not depend as much as in the case of the Pt-deposited surface. As shown in Figure 2-16, thickness dependence of the intensity ratio between the Pt-deposited surface and MgO substrates showed a different trend. The threshold was not observed in the case of the MgO substrate which suggests that the thin film structure depends on the type of the substrate. Similar thresholds of the proton conductivity and surface hydrophilicity were reported respectively by Modestino *et al.* and Paul *et al.* using the thermal treated SiO_2 surface, [14, 26].

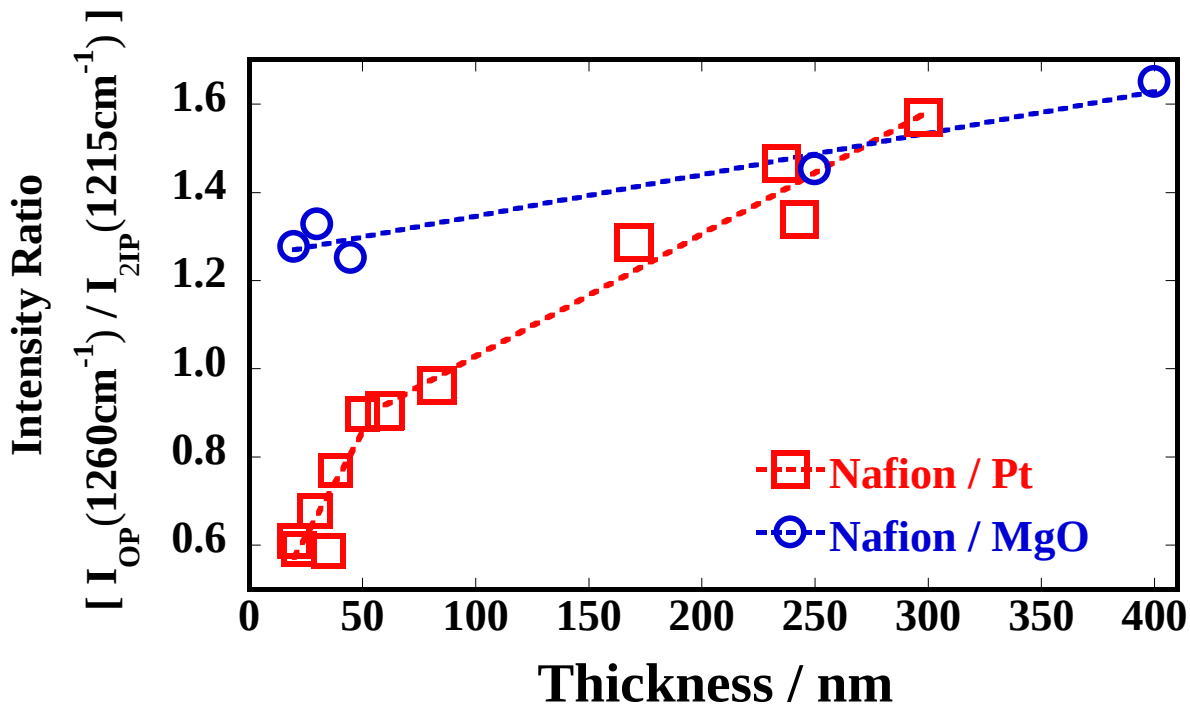

Figure 2-16. Thickness dependence of relative intensity ratios based on the strongest bands located at 1260 cm^{-1} (OP) and 1215 cm^{-1} (IP) for the Nafion thin films.

Figure 2-17 shows the proposed schematic views of the interface structure of the Nafion thin films on the Pt and MgO substrate. The hydrophobic PTFE backbone might be orient to in-plane direction. This oriented structure is similar to the structure proposed by other groups [12, 23, 24]. In the case of the Pt-deposited surface, sulfonic acid groups are in non-dissociative state in the section of the pMAIR results and previous reports [43, 51].

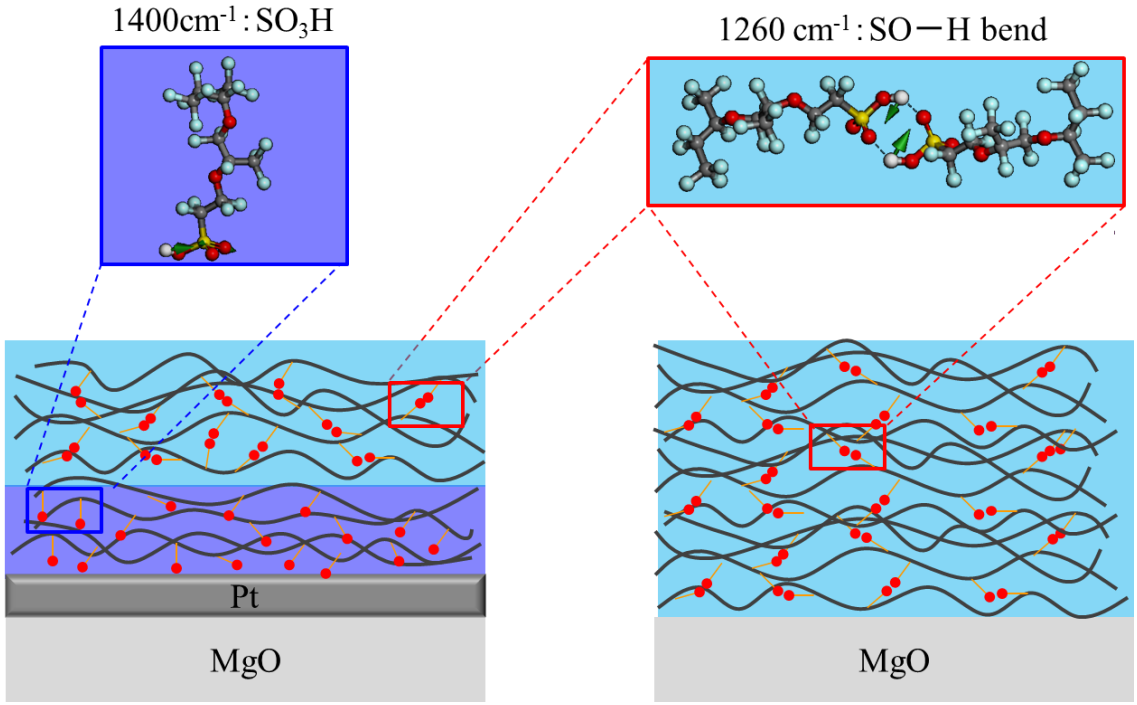

Figue 2-17. Schematic views of the interface structure of the Nafion thin films on the Pt and MgO substrate.

The thickness dependence of the proton conductivity on the SiO_2 substrate has been reported [16, 26, 29, 35]. Modestino and co-workers reported that this conductivity change derives from the change of the interface structure from the GI-SAXS results. However, the proton transport on the Pt-deposited surface has not been sufficiently discussed. The thickness dependence of proton conductivity of the Nafion thin film for various RH at 298 K is shown in Figure 2-18. Proton conductivity is dependent on thickness and RH. These proton conductivities were found to be $10^{-3} - 10^{-2}$ S cm^{-1} at 95% RH. However, their conductivities were lower than that of the commercial bulk

Nafion membrane. Furthermore, stronger RH dependence of the proton conductivity was observed in the thin film case. At the low RH region, the proton conductivity depends on the surface type. Proton conductivity on the Pt-deposited surface was one order of magnitude higher than that on the SiO_2 substrate. This difference might derive from the different thin film structure and/or state of proton dissociation of the sulfonic acid groups, as discussed in the section of the pMAIR results.

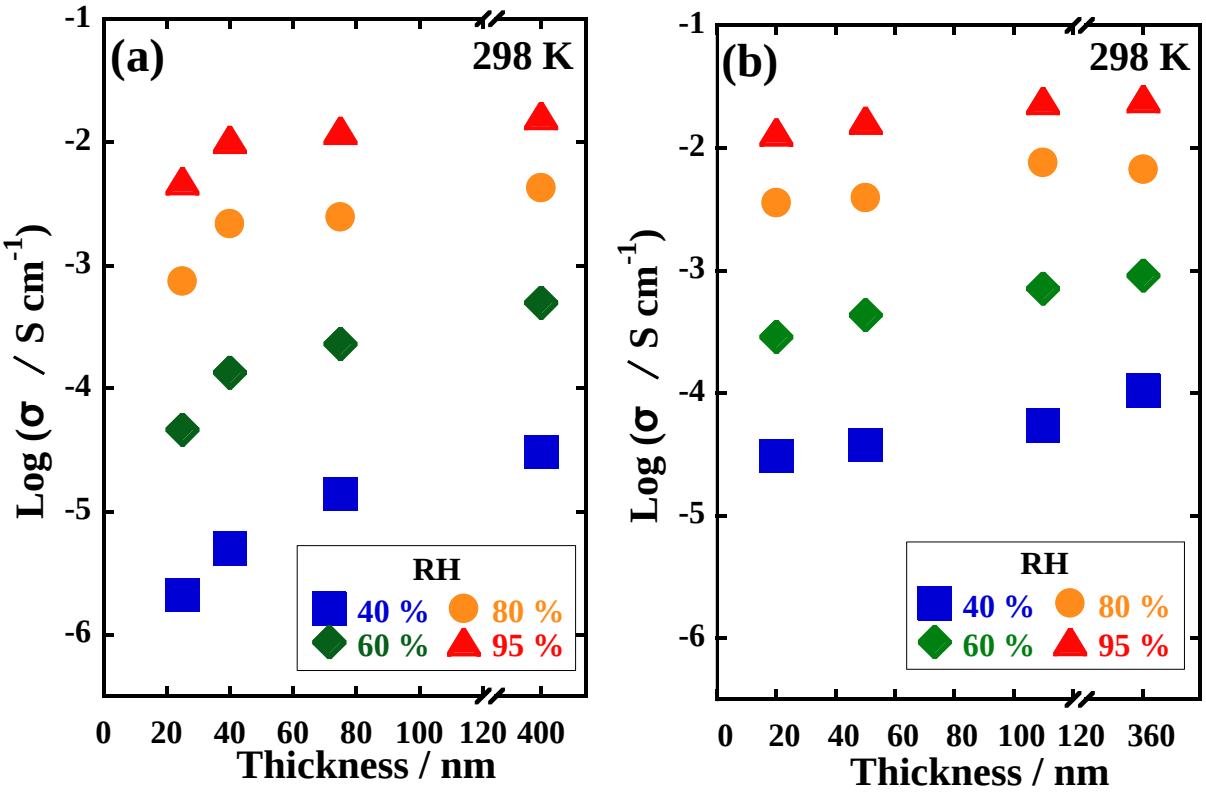

Figure 2-18. Thickness dependence of the proton conductivity for the Nafion thin films at various RH: (a) on SiO_2 and (b) on Pt-deposited surfaces.

The activation energy of each RH can provide useful information related to the proton conduction mechanism. To obtain the activation energy, the temperature dependence of the proton conductivity is shown in Figure 2-19.

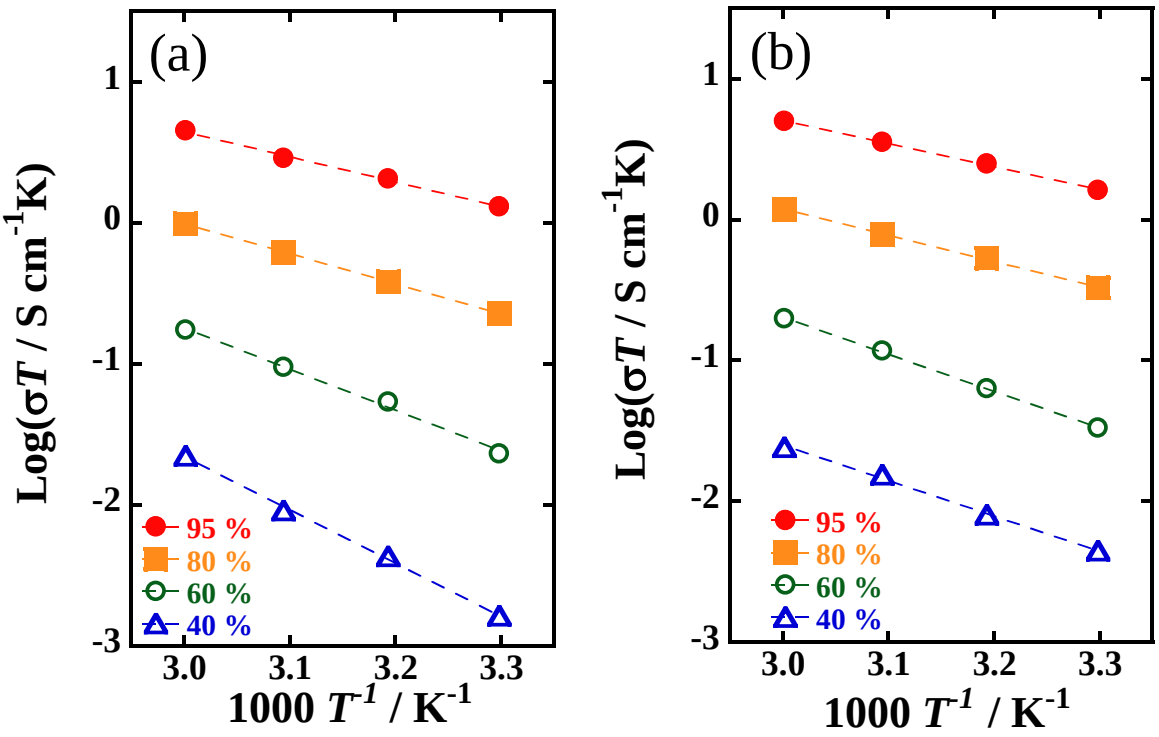

Figure 2-19. Temperature dependence of proton conductivities at various RH. (a) 40-nm -thick film on SiO_2 surface. (b) 40-nm-thick film on Pt-deposited surface.

All log(σT) depended lineally on the $1000T^{-1}$ in this temperature region. The activation energy for the 40-nm-thick Nafion thin films on SiO_2 and Pt-deposited surfaces is shown in Figure 2-20 as a function of the RH. At the high RH region, all activation energies exhibited similar values (ca. 0.3–0.4 eV). However, at the low RH region, the activation energies depended strongly on the surface. The activation energy depends

strongly on RH in the case of the SiO_2 surface. A similar trend was reported by Paul *et al.* [16]. In the case of the Pt-deposited surface as new data, the activation energy was 0.4–0.5 eV, which has lower activation energy than in the SiO_2 surface case. The reason for the relatively higher proton conductivity at the low RH on the Pt-deposited surface is derived from this lower activation energy.

To understand the origin of the lower activation energy on the Pt-deposited surface, it is essential to consider the Nafion interface on the Pt-deposited surface. Water uptake and the diffusion coefficient of the water were informative physical parameters for the further discussion of the proton transport. Eastman et al. reported that the diffusion coefficient of the water decreased drastically at the interface [28]. These data are based on the polarization modulation-infrared reflection-adsorption spectroscopy (PM-IRRAS) with the Au surface and QCM measurements with the SiO_2 surface. The diffusion coefficient between the metal and SiO_2 surfaces shows no difference. Regarding water uptake, Murthi *et al.* , Kusoglu *et al.* and Shim *et al.* reported that the water content (λ) at the interface on the Pt [18] surface is less than that of the bulk [27, 52]. Modestino *et al.* reported that the water content at the interface on the SiO_2 surface is greater than that of the bulk. This greater water uptake enhances the dilution and isolation of the sulfonic acid groups. [26]. This contributes to the decrease of the proton

conductivity and to the high activation energy. Based on the description presented above, the Nafion interface on the Pt-deposited surface might hold the low water contents. The appropriate amount of water might develop a favorable structure for the proton conduction. The proton conductivity at further low RH around 0% was not obtainable because of limited machine specifications.

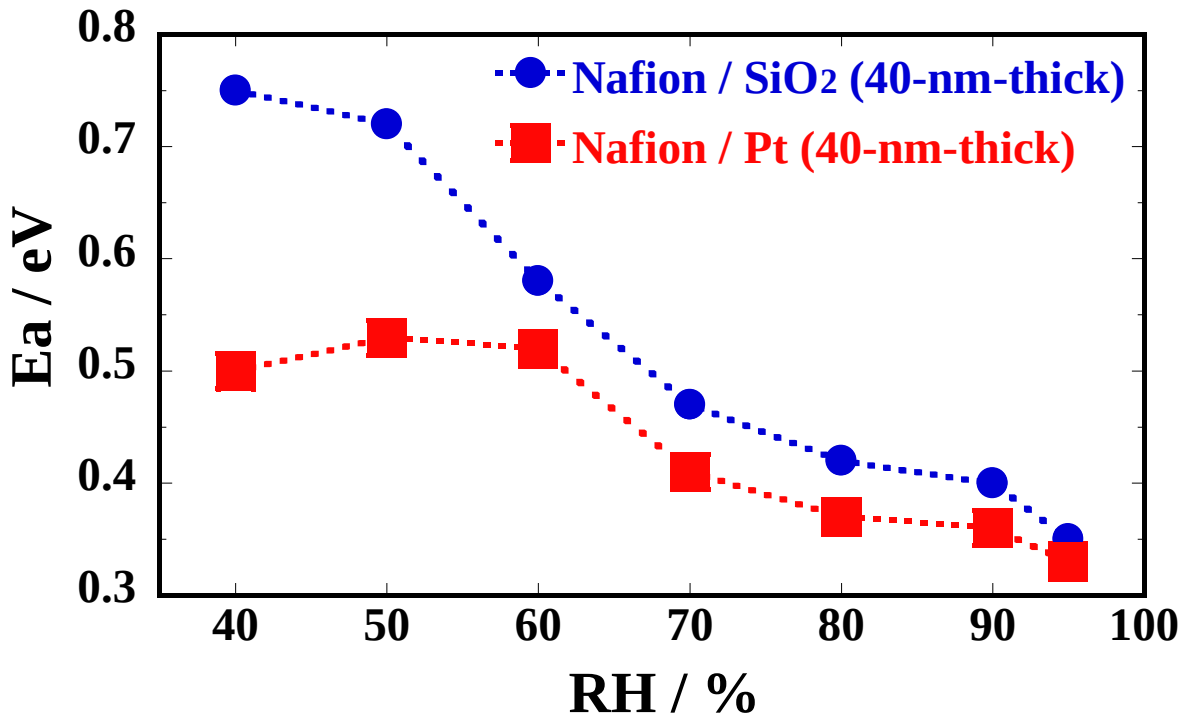

Figure 2-20. Activation energy for the 40-nm-thick Nafion thin films on SiO_2 and Pt-deposited surface as a function of the RH.

2-4. Conclusion

The interfacial confinement of polymer electrolyte structure strongly affects the proton transport property. Although structure and properties of Nafion bulk membranes have been investigated widely, the character of their confined thin films on the Pt-deposited surface as a model of the three-phase boundary remains unclear. Nafion has an orientation structure at the Pt-deposited surface by pMAIRS. The degree of orientation on the Pt-deposited surface depends on the thickness. A different dissociation state of sulfonic acid groups was also observed. At the low-RH region, proton conductivity depends on the Pt-deposited and SiO_2 surfaces. Proton conductivity on the Pt-deposited surface was one order of magnitude higher than that on SiO_2 substrate, but its conductivity remained lower than that of the bulk membrane. This difference might be derived from the different thin film structure and/or the dissociation state of the protons at the sulfonic acid groups. For the Pt-deposited surface, the activation energy is 0.4–0.5 eV, which has lower activation energy than in the case of the SiO_2 surface. These results elucidate the relationship between the proton transport property and thin film structure on the Pt-deposited surface at the three-phase boundary for fuel cells.

References

[1] Holdcroft, S. Fuel Cell Catalyst Layers: A Polymer Science Perspective. *Chem. Mater.* **2014**, *26*, 381–393.

[2] Nagao, Y.; Naito, N.; Iguchi, F.; Sata, N.; Yugami, H. Synthesis of Oligomeric Poly[(1, 2-propanediamine)-alt-(oxalic acid)] and Anomalous Proton Conductivities of the Thin Films. *Solid State Ionics* **2009**, *180*, 589–591.

[3] Nagao, Y.; Iguchi, F.; Sata, N.; Yugami, H. Synthesis and Proton Transport Property of Poly(aspartic acid) Thin Film on SiO_2 Substrate. *Solid State Ionics* **2010**, *181*, 206–209.

[4] Krishnan, K.; Iwatsuki, H.; Hara, M.; Nagano, S.; Nagao, Y. Proton Conductivity Enhancement in Oriented, Sulfonated Polyimide Thin Films. *J. Mater. Chem. A* **2014**, *2*, 6895–6903.

[5] Krishnan, K.; Yamada, T.; Iwatsuki, H.; Hara, M.; Nagano, S.; Otsubo, K.; Sakata, O.; Fujiwara, A.; Kitagawa, H.; Nagao, Y. Influence of Confined Polymer Structure on Proton Transport Property in Sulfonated Polyimide Thin Films. *Electrochemistry* **2014**, *82*, 865–869.

[6] Matsui, J.; Miyata, H.; Hanaoka, Y.; Miyashita, T. Layered Ultrathin Proton Conductive Film Based on Polymer Nanosheet Assembly. *ACS Appl. Mater. Interfaces*

2011, *3*, 1394–1397.

[7] Mauritz, K. A.; Moore, R. B. State of Understanding of Nafion. *Chem. Rev.* **2004**, *104*, 4535–4585.

[8] Schmidt-Rohr, K.; Chen, A. Q. Parallel Cylindrical Water Nanochannels in Nafion Fuel-Cell Membranes. *Nature Mater*. **2008**, *7*, 75–83.

[9] Gebel, G.; Diat, O. Neutron and X-ray Scattering: Suitable Tools for Studying Ionomer Membranes. *Fuel Cells* **2005**, *5*, 261–276.

[10] Hsu, W. Y.; Gierke, T. D. Ion Transport and Clustering in Nafion Perfluorinated Membranes. *J. Membr. Sci*. **1983**, *13*, 307–26.

[11] Kreuer, K. D. On the Development of Proton Conducting Polymer Membranes for Hydrogen and Methanol Fuel Cells. *J. Membr. Sci.* **2001**, *185*, 29–39.

[12] Peng, H. C.; Wang, C. N.; Yeh, T. K.; Su, Y. C.; Pan, C.; Tseng, F. G. A high Efficient Micro-Proton Exchange Membrane Fuel Cell by Integrating Micro-Nano Synergic Structures. *J. Power Sources* **2014**, *225*, 277–285.

[13] More, K.; Borup, R.; Reeves, K. Identifying Contributing Degradation Phenomena in PEM Fuel Cell Membrane Electride Assemblies via Electron Microscopy. *ECS Trans.* **2006**, *3*,717–733.

[14] Paul, D. K.; Karan, K.; Docoslis, A.; Giorgi, J. B.; Pearce, J. Characteristics of

Self-Assembled Ultrathin Nafion Films. *Macromolecules* **2013**, *46*, 3461–3475.

[15] Paul, D. K.; Fraser, A.; Karan, K. Towards the Understanding of Proton Conduction Mechanism in PEMFC Catalyst Layer: Conductivity of Adsorbed Nafion Films. *Electrochem. Commun.* **2011**, *13*, 774–777.

[16] Paul, D. K.; McCreery, R,; Karan, K. Proton Transport Property in Supported Nafion Nanothin Films by Electrochemical Impedance Spectroscopy. *J. Electrochem. Soc.* **2014**, *161*, 1395–1402.

[17] Paul, D. K.; Karan, K. Conductivity and Wettability Changes of Ultrathin Nafion Films Subjected to Thermal Annealing and Liquid Water Exposure. *J. Phys. Chem. C* **2014**, *118*, 1828–1835.

[18] Murthi, V. S.; Dura, J. A.; Satija, S.; Majkrzak, C. F. Water Uptake and Interfacial Structural Changes of Thin Film Nafion Membranes Measured by Neutron Reflectivity for PEM Fuel Cells. *ECS Trans*. **2008**, 16, 1471–1485.

[19] Dura, J. A.; Murthi, V. S.; Hartman, M.; Satija, S.; Majkrzak, C. F. Multilamellar Interface Structures in Nafion. *Macromolecules* **2009**, *42*, 4769–4774.

[20] Kim, S.; Dura, J. A.; Page, K. A.: Rowe, B. W.; Yager, K. G.; Lee, H. J.; Soles, C. L. Surface-Induced Nanostructure and Water Transport of Thin Proton-Conducting Polymer Films. *Macromolecules* **2013**, *46*, 5630–5637.

[21] Ogata, Y.; Kawaguchi, D.; Yamada, N.L.; Tanaka, K. Multistep Thickening of Nafion Thin Films in Water. *ACS Macro. Lett.* **2013**, *2*, 856–859.

[22] Wood, D. L.; Chlistunoff, J.; Majewski, J.; Borup, L. Nafion Structural Phenomena at Platinum and Carbon Interfaces. *J. Am. Chem. Soc.* **2009**, *131*, 18096–18104.

[23] Bass, M.; Beman, A.; Singh, A.; Konovalov, O.; Freger, V. Surface Structure of Nafion in Vapor and Liquid. *J. Phys. Chem. B* **2010**, *114*, 3784–3790.

[24] Bass, M.; Beman, A.; Singh, A.; Konovalov, O.; Freger, V. Surface-Induced Micelle Orientation in Nafion Films. *Macromolecules* **2011**, *44*, 2893–2899.

[25] Modestino, M. A.; Kusoglu, A.; Hexemer, A.; Weber, A. Z.; Segalman, R. A. Controlling Nafion Structure and Properties via Wetting Interactions. *Macromolecules* **2012**, *45*, 4681–4688.

[26] Modestino, M. A.; Paul, D. K.; Dishari, S.; Petrina, S. A.; Allen, F.; Hickner, M. A.; Karan, K.; Segalman, R. A.; Weber, A. Z. Self-Assembly and Transport Limitations in Confined Nafion Films. *Macromolecules* **2013**, *46*, 867–873.

[27] Kusoglu, A.; Kushner, D.; Paul, D. K.; Karan, K.; Hickner, M. A.; Weber, A. Z. Impact of Substrate and Processing on Confinement of Nafion Thin Films. *Adv. Funct. Mater.* **2014**, *24*, 4763–4774.

[28] Eastman, S. A.; Kim, S.; Page, K. A.; Rowe, B. W.; Kang, S.; Soles, C. L. Effect of

Confinement on Structure, Water Solubility, and Water Transport in Nafion Thin Films. *Macromolecules* **2012,** *45***,** 7920–7930.

[29] Nagao, Y. Proton Transport Property of Nafion Thin Films on MgO(100) with Anisotropic Molecular Structure. *e-J. Surf. Sci. Nanotechnol*. **2012**, *10* 114–116.

[30] Nagao, Y. Highly Oriented Sulfonic Acid Groups in a Nafion Thin Film on Si Substrate. *J. Phys. Chem. C* **2013**, *117*, 3294–3297.

[31] Hasegawa, T. A Novel Measurement Technique of Pure Out-of-plane Vibrational Modes in Thin Films on a Nonmetallic Material with No Polarizer. *J. Phys. Chem. B* **2002**, *106*, 4112–4115.

[32] Hasegawa, T.; Matsumoto, L.; Kitamura, S.; Amino, S.; Katada, S.; Nishijo, J. Optimum Condition of Fourier Transform Infrared Multiple-Angle Incidence Resolution Spectrometry for Surface Analysis. *Anal. Chem*. **2002**, *74*, 6049–6054.

[33] Hasegawa, T. Advanced Multiple-angle Incidence Resolution Spectrometry for Thin-layer Analysis on a Low-refractive-index Substrate. *Anal. Chem.* **2007**, *79*, 4385–4389.

[34] Hasegawa, T.; Itoh, Y.; Kasuya, A. A. Experimental Optimization of P-polarized MAIR Spectrometry Performed on a Fourier Transform Infrared Spectrometer. *Anal. Sci*. **2008**, *24*, 105–109.

[35] Siroma, Z.; Kakitubo, R.; Fujiwara, N.; Ioroi, T.; Yamazaki, S.; Yasuda, K. Depression of Proton Conductivity in Recast Nafion Film Measured on Flat Substrate. *J. Power Sources* **2009**, *189*, 994–998.

[36] Kongkanand, A. Interfacial Water Transport Measurements in Nafion Thin Films Using a Quartz-Crystal Microbalance. *J. Phys. Chem. C* **2011**, *115*, 11318–11325.

[37] Abuin, G. C.; Fuertes, M. C.; Corti, H. R. Substrate Effect on the Swelling and Water Sorption of Nafion Nanomembranes. *J. Membr. Sci*. **2013**, *428*, 507–515.

[38] Dishari, S. K.; Hickner, M. A. Antiplasticization and Water Uptake of Nafion Thin Films. *ACS Macro. Lett.* **2012**, *1*, 291–295.

[39] Parkinson, C. R.; Walker, M.; McConville, C. F. Reaction of Atomic Oxygen with a Pt(111) Surface: Chemical and Structural Determination Using XPS, CAICISS and LEED. *Surf. Sci.* **2003**, *545*, 19–33.

[40] Gruger, A.; Regis, A.; Schmatko, T.; Colomban, P. Nanostructure of Nafion Membranes at Different States of Hydration an IR and Raman Study. *Vib. Spectrosc.* **2001**, *26*, 215–225.

[41] Danilczuk, M.; Lin, L.; Schlick, S.; Hamrock, S. J.; Schaberg, M. S. Understanding the Fingerprint Region in the Infra-red Spectra of Perfluorinated Ionomer Membranes and Corresponding Model Compounds: Experiments and Theoretical Calculations. *J.*

Power Sources **2011**, *196*, 8216–8224.

[42] Davis, E. M.; Stafford, C. M.; Page, K. A. Elucidating Water Transport Mechanisms in Nafion Thin Films. *ACS Macro Lett*. **2014**, *3*, 1029–1035.

[43] Kendrick, I.; Kumari, D.; Yakaboski, A.; Dimakis, N.; Smotkin, E. S. Elucidating the Ionomer-electrified Metal Interface. *J. Am. Chem. Soc.* **2010**, *132*, 17611–17616.

[44] Zeng, J.; Jean, D. I.; Ji, C.; Zou, S. In Situ Surface-Enhanced Raman Spectroscopic Studies of Nafion Adsorption on Au and Pt Electrodes. *Langmuir* **2012**, *28*, 957– 964.

[45] Malevich, D.; Zamlynny, V.; Sun, S.-G.; Lipkowski, J. *In situ* Infrared Reflection Absorption Spectroscopy Studies of the Interaction of Nafion® with the Pt Electrode Surface. *Z. Phys. Chem.* **2003**, *217*, 513–525.

[46] Korzeniewski, C.; Snow, D. E.; Basnayake, R. Transmission Infrared Spectroscopy as a Probe of Nafion Film Structure: Analysis of Spectral Regions Fundamental to Understanding Hydration Effects. *Appl. Spectrosc*. **2006**, *60*, 599–604.

[47] Yamaguchi, M.; Ohira, A. Vibrational Analysis of Side Chain Model Compounds of Perfluorinated Alkyl Sulfonic Acid Ionomers. *J. Phys. Chem. A* **2012**, *116*, 10850–10863.

[48] Warren, D. S.; McQuillan, A. J. Infrared Spectroscopic and DFT Vibrational Mode Study of Perfluoro(2-ethoxyethane) Sulfonic Acid (PES), a Model Nafion Side-chain

Molecule. *J. Phys. Chem. B* **2008**, *112*, 10535–10543.

[49] Ludvigsson, M.; Lindgren, J.; Tegenfeldt, J. FTIR Study of Water in Cast Nafion Films. *Electrochim. Acta* **2000**, *45*, 2267–2271.

[50] Malek, K.; Mashio, T.; Eikerling, M. Microstructure of Catalyst Layers in PEM Fuel Cells Redefined: A Computational Approach. *Electrocatal*. **2011**, *2*, 141–157.

[51] Yagi, I.; Inokuma, K.; Kimijima, K.; Notstu, H. Molecular Structure of Buried Perfluorosulfonated Ionomer/Pt Interface Probed by Vibrational Sum Frequency Generation Spectroscopy. *J. Phys. Chem. C* **2014**, *118*, 26182–26190.

[52] Shim, H. K.; Paul, D. K.; Karan, K. Resolving the Contradiction between Anomalously High Water Uptake and Low Conductivity of Nanothin Nafion films on SiO_2 Substrate *Macromolecules* **2015**, *48*, 8394–8397.

Chapter 3
Highly proton conductive polyimide thin films with organized structure

Abstract

The insight into confined polymer thin film is imperative to enhance the performance of polymer electrolyte fuel cells. The previous study revealed that the enhancement of the proton transport was attributable to molecular ordering and orientation of the liquid crystal domains in sulfonated polyimide thin films. However, collation of its property and water-uptake is still not well understood. This chapter clarifies the relationship between the proton transport property, water uptake and organized structure using sulfonated polyimide thin film with different molecular structure. Quartz crystal microbalance (QCM) was used to investigate the water uptake for thin film. The different main chain alkyl sulfonated polyimide (ASPI) show the well-defined ordering structure and highly proton transport property at the high relative humidity. These results demonstrated that the molecular ordering structure of the polyimide thin film may significantly affect the proton transport property.

3-1. Introduction

1. Introduction

Research on energy conversion technology has rapidly expanded for use as a next-generation power source due to necessary for sustainable energy. Polymer electrolyte fuel cells (PEFCs), in which typically proton exchange and anion exchange membranes, respectively have been expected because of their environmentally friendly and high efficiency. Due to the most important components of fuel cell, much effort has been devoted for the research of advanced polymer electrolyte [1-5].

Nafion is one of the most widely studied polymer electrolytes for fuel cell study [6-10]. The hydrated Nafion, it is well known that high proton conductivity is achieved by well phase-separated hydrophilic nanochannel. However, perfluorosulfonated polymer is restricted by some drawbacks such as high cost, high gas permeability and poor molecular design [11,12]. In order to solve these problems, development of alternative polymer electrolyte is needed. Over the past decade many efforts have been devoted to the development of alternative polymer electrolyte. To achieve the high proton conductivity, several PEM such as sulfonated block copolymers and graft copolymers using the concept of the well phase-separated hydrophilic channel. In addition, proton conductivity of polymer electrolyte membranes is closely related to several parameters

such as acidity, number of sulfonic acid groups, main chain and side chain structures, and membrane morphology [13-18]. These are mainly done by chemical modification. Therefore, it should be hard to focus on the relationship between the structure and proton conductivity.

From another view point, structural confinement effect of the polymer electrolyte thin film has been reported [19-39]. Structure and property of confined polymer thin film are altered drastically from the bulk due to interaction of the surface and substrate interface. For example, study of the Nafion thin films has demonstrated that the degree of the phase segregation and proton conductivity losses with decreasing the thickness [37]. Another Nafion thin film study have reported a lower water uptake, but it is still not well understood [29, 37].

In contrast, recent investigations of the enhancement for proton conductive properties have been reported by the structural control of the proton conductive channel without chemical modification [22-28]. Sato and Matsui *et al.* reported that the well-defined two-dimensional lamella structure of the thin polymer film with carboxylic acid shows the high proton conductivity and large anisotropic proton conductivity [23,24]. This result shows a possibility for enhancement the proton conductivity using the molecular orientation.

In order to characterize the proton conductive nanochannel it is necessary to investigate the orientation and higher order structure in polymer. Sulfonated polyimide with alkyl side chains is found to be the high proton conductivity as well as highly molecular ordered structure [25-27].The SPI with rigid and planer molecular structure shows the lyotropic LC like property by water uptake, which responds reversibly by the humidity. Furthermore, proton conductivity of the SPI thin film was affected by size of the LC domains and degree of the molecular ordering [27]. However, relationship between the proton transport property and ordered structure remains unclear.

It is well known that aggregation structures in polyimide results in a LC like ordered structure and amorphous matrix. Ando and co-workers have investigated the detail orientation and aggregation structures of the aromatic and semialiphatic polyimides (PIs) [42]. They found that PI film with nonplanar molecular structure exhibits lower degree of the orientation in the liquid-crystalline-like ordered domains than those of rigid planar molecular structure. The steric effects of the PI film have influences on the aggregation structure, packing structure and π−π stacking of imide and phenyl rings. In other words, such higher order structure of PI can be modified by different molecular structure. In this chapter, author designed and synthesized SPI with nonplanar molecular

structure using the different dianhydride moieties. The nonplanar molecular structure can be expected the different molecular ordering.

This work provides insight into the relationship between the proton transport property and organized polymer nanostructure. In this study an effect of nonplanar polymer backbone to the organized structure, water uptake and proton conductivity of the four sulfonated polyimide thin film is discussed. Grazing-Incidence Small-Angle X-ray Scattering (GISAXS) is used to elucidate the structure of thin films and help to understanding of differences of the higher-order structure. Quartz crystal microbalance (QCM) was conducted to investigate precisely the influence of adsorbed water molecules on lyotropic liquid crystallinity property of the polymer thin film. The *in-situ* FT-IR measurement was investigated for dissociation of the sulfonic acid groups. I finally discuss the importance of higher-order structure for achieving high proton conductivity.

3-2. Experimental section

3-2-1. Materials

1,4,5,8-Naphthalenetetracarboxylic dianhydride (NTDA) was used as received from Sigma–Aldrich. 3,3′-Dihydroxybenzidine, propanesultone, and pyromellitic dianhydride

(PMDA), 4,4'-oxydiphthalic anhydride (ODPA) and 4,4'-biphthalic anhydride (BPDA) were used as received from TCI, Japan. Acetic acid, acetic anhydride, methanol, and acetone were purchased from Wako Chemicals, Japan. Hydrochloric acid (Nacalai Tesque, Japan), sodium hydroxide (Kishida Chemical, Japan), *m*-cresol, and triethylamine (TEA) (Kanto Chemicals, Japan) were used as received. 3,3'-Bis(sulfopropoxy)-4,4'-diaminobiphenyl (3,3'-BSPA) was synthesis by according to the literature [25-27].

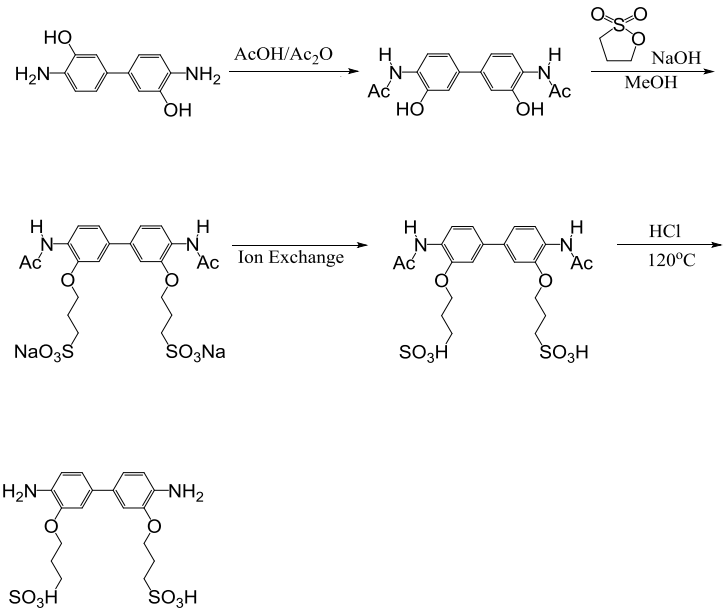

Scheme 3-1. Synthesis of monomer (3, 3'-BSPA).

Sulfonated polyimide with various molecular structures was prepared using the same polymerization scheme (Scheme 3-2). A typical procedure for the synthesis of sulfonated polyimide (ASPI) is as follows. 1 mmol of BSPA, 1 mmol of anhydride-monomer, 7 ml of m-cresol, and 300μl of TEA were added to a round-bottom

flask equipped with a magnetic stirrer bar under argon atmosphere at a constant temperature of 150 ℃ for 6 h. The polymerized product was precipitated in large excess cooled acetone. The precipitate was collected by centrifuge, washed several times with fresh acetone and dried under vacuum for overnight. The final product was subjected to an ion-exchange process using Amberlyst. ^{1}H NMR measurements were performed on a Bruker Avance III 400 spectrometer using dimethyl sulfoxide (DMSO-d_6) as the solvent and tetramethylsilane (TMS) as the internal reference.

Infrared (IR) spectra were measured by Fourier-transform infrared (FTIR) spectrometer (Nicolet 6700; Thermo Fisher Scientific Inc.) equipped with attenuated total reflection (ATR) accessory in the range 400−4000 cm^{-1}.

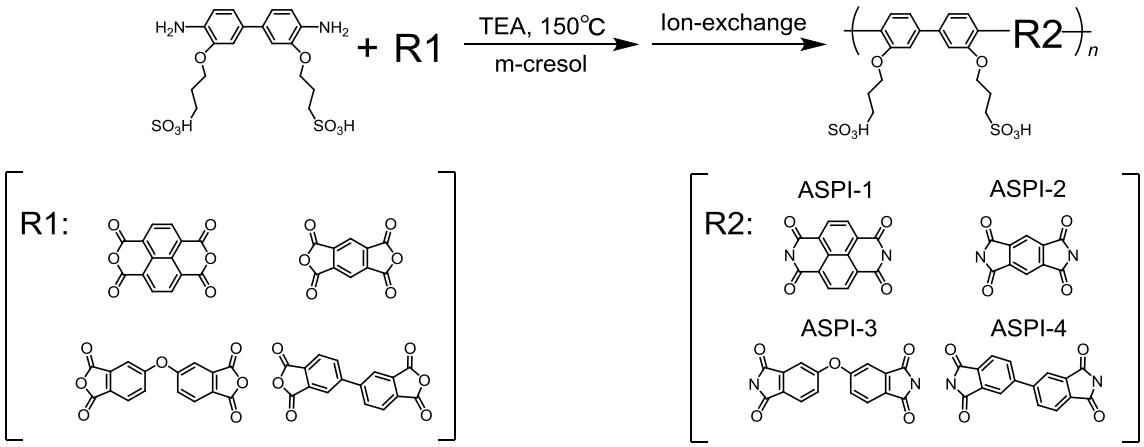

Scheme 3-2. Synthesis of Sulfonated Polyimide.

3-2-2. Gel Permeation Chromatography (GPC)

The molecular weights of SPI were determined by Gel permeation chromatography (GPC, LC-2000plus; Jasco Inc.) with Shodex GF-1G 7B and GF-7M HG columns. Response to the HPLC system control of up to four through the (controller) LC-Net II/ADC enables simultaneous recording of four chromatograms per system. A DMF-, H_2O-, CH_3COOH-, and $NaNO_3$-containing mixture was used as the eluent at a flow rate of 1.0 mL min^{-1}. The polymer solutions were filtered through a 0.50 μm PTFE hydrophobic filter before being injected into the column. The molecular weight was calibrated with a polystyrene standard.

3-2-3-1. Thin Film Preparation

For this study, Si , SiO_2 substrates (each 15 × 15 × 0.5 mm) and SiO_2 -coated 9 MHz quartz crystal microbalance (QCM) substrates (SEIKO EG&G Co. Ltd.) were used respectively for thin film preparation by spin-coating (ACT-200; Active Co. Ltd.), few wt % ASPI dispersion was used. Thicknesses of c.a.500 nm were found using an atomic force microscopy (AFM, VN-8000; Keyence Co.) and White interference microscope (BW-S506; Nikon Co.). The ASPI thin films were dried for at least 12 hr in a desiccator.

3-2-3-2. Solution Shearing of ASPI Thin film

Uniaxial orientation film was prepared by solution shearing the high viscosity ASPI-2 solution (c.a.18wt%) in H_2O and THF on CaF_2 substrate. Solution shearing was performed in ambient condition, using a doctor-blade (Figure 3-1). The sheared ASPI-2 film was dried under vacuum condition.

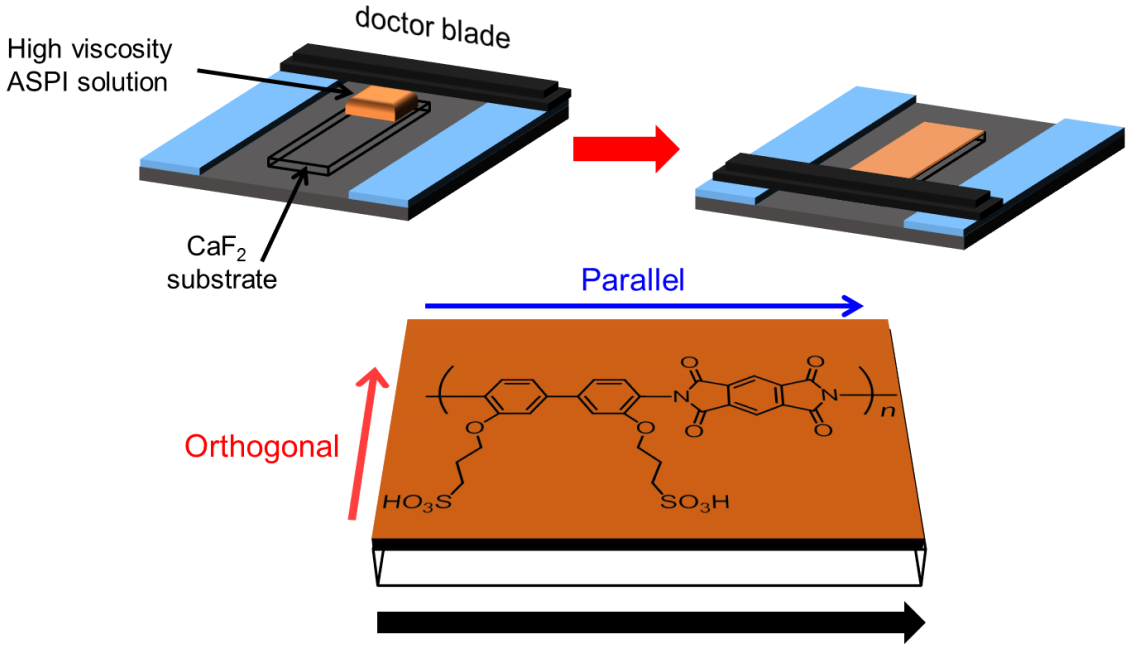

Figure 3-1. Schematic illustration of the solution shearing.

3-2-4. Proton Conductivity Measurement of the SPI Thin Films

The proton conductivity of thin films were was measured in at relative humidity (RH) range of 40–95% with and temperature of 298 K using an impedance / gain-phase analyzer (SI1260; Solartron Analytical) with a dielectric interface system (SI1296; Solartron Analytical) with humidity-controlled and temperature-controlled chamber

(SH-221; Espec Corp). The Measurements were taken parallel to the substrate. The Au electrodes were fabricated at the edge of thin film. The impedance data were collected in at the frequency range of 10 MHz and 1 Hz with amplitude of 50 mV. Proton conductivity (σ) was calculated as follows,

$$\sigma = \frac{d}{Rlt} \quad (1)$$

where d is the distance between the Au electrodes, R is the resistance value from impedance, l and t are the length of the contact electrodes and thickness of the film respectively.

3-2-5. Water Uptake Measurements

Water up-take was measured using an *in-situ* QCM system. Figure 3-2 shows the schematic illustration of QCM measurement. QCM substrates were connected to oscillation circuit with DC power supply and frequency counter (53131A, Agilent Technologies Japan). The QCM substrate was placed in an in-house constructed humidity chamber with high-resolution RH sensor. A various humidity environments were produced using a dry N_2 and humidified streams by humidity controller (BEL Flow, BEL Japan). The frequency of the before and after the spin-coating of the QCM substrate were conformed at the dry N_2 stream for determined the mass of dry film by

the Sauerbrey equation

$$\Delta m = \frac{S \times \sqrt{\rho \mu}}{2 \times F^2} \times (-\Delta F) \quad (2)$$

where S is electrode surface area, ρ is density of quartz and F is fundamental frequency of QCM substrate.

The water content , λ was calculated as follows,

$$\lambda = \left(\frac{m}{m_0} - 1\right) \times \frac{EW}{M_{H_2O}} \quad (3)$$

where m is film mass at the each RH, m_0 is film mass of at the 0%RH, M_{H_2O} is molecular mass of water molecular, and EW is equivalent weight of each SPI.

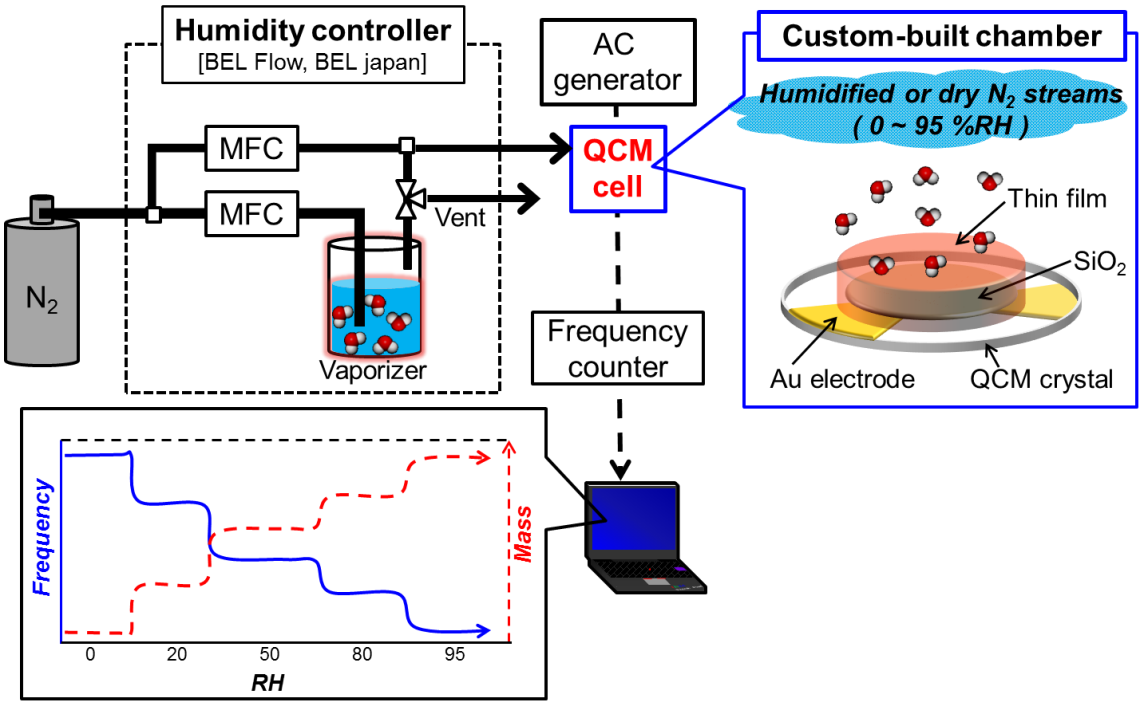

Figure 3-2. Schematic illustration of QCM measurement.

3-2-6. Polarized Optical Microscopy (POM)

POM was used to elucidate the lyotropic LC domain morphologies and there size in ASPI films. POM observation was performed using an Optical microscope (BX51, BX51-P; Olympus Corp.) with digital camera (DP28 camera; Olympus Corp.). All POM observation was carried out at the room temperature and ambient humidity.

3-2-7. Grazing-Incidence Small-Angle X-ray Scattering Measurements (GI-SAXS).

GI-SAXS measurements were carried out as described previously in the literature. Figure 3-3 shows the schematic illustration of *in-situ* GI-SAXS measurement. The in-situ X-ray scattering experiments were performed on a X-ray diffractometer (FR-E; Rigaku Corp.) with an R-AXIS IV two-dimensional (2D) detector. The sample stage was composed of the goniometer and a vertical stage (ATS-C316-EM/ALV-300-HM; Chuo Precision Industrial Co. Ltd.) with a humidity-controlled cell. The typical cell holds polyimide film (Kapton) windows and the humidity-controlled cell. Nitrogen carrier gas was used as received, without further dehumidification, from the gas cylinder to control the humidity. Cu Kα radiation (λ = 0.1542 nm) with a beam size of approximately 300 μm × 300 μm. The camera length was 300 mm. The incidence angle

was chosen in the range from 0.20° to 0.22°.

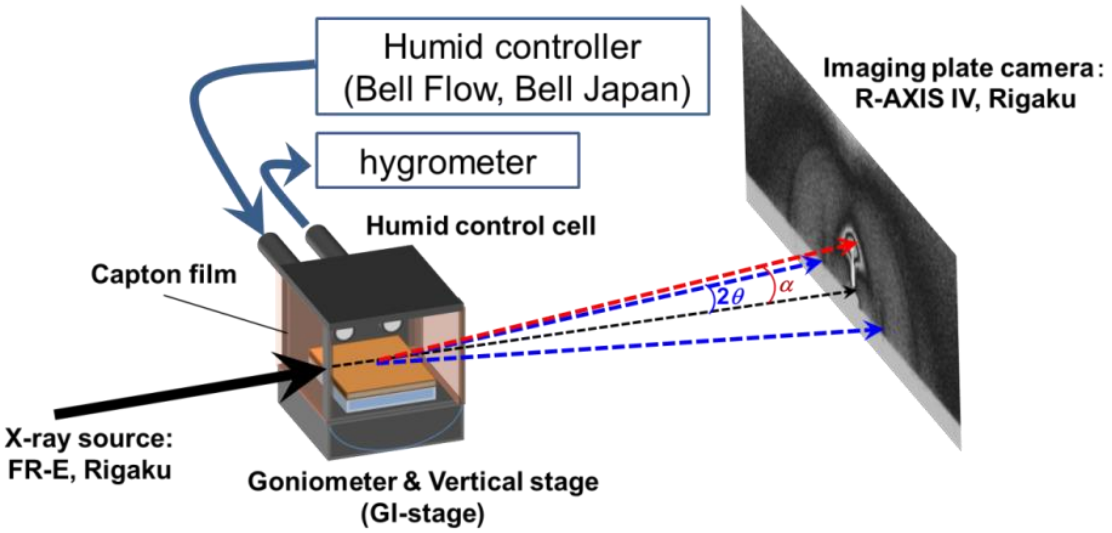

Figure.3-3. Schematic illustration of in-situ GI-SAXS measurement.

3-2-8. DFT Calculations

Density functional theory (DFT) calculations were performed using the DMol3 package in Materials Studio (Accelrys Software Inc.). The Perdew−Burke−Ernzerhof (PBE) function was chosen. Convergence threshold for the maximum force and maximum displacement for normal geometry optimization were set respectively to 0.004 Ha $Å^{-1}$ and 0.005 Å.

3-2-9. Infrared (IR) p-polarized Multiple-angle Incidence Resolution Spectrometry (pMAIRS)

To investigate IP and OP molecular vibrations in an identical thin film, the IR pMAIRS technique was performed. The pMAIRS measurements were taken using an FT-IR spectrometer (Nicolet 6700; Thermo Fisher Scientific Inc.) equipped with a mercury–cadmium–telluride (MCT) detector. The optical configuration is shown in Figure 1. To obtain the p-polarized light, a ZnSe polarizer was used. Single-beam spectra were collected from 38° through 8° in 6° steps between the angles of incidence. The wavenumber resolution was 4 cm^{-1}. The number of scans was were 64 for each angle of incidence. Dry air or N_2 gases were passed through the sample compartment and inside of the spectrometer for air purge. The humidity of the sample compartment was less than 5% under room temperature. The aperture was fully opened (size of 150). A metal plate with small pores was placed in the light path of the incidental beam to prevent saturation. The pMAIRS analysis from the collected spectra was conducted automatically using pMAIRS analyzer software (Thermo Fisher Scientific Inc.).

3-3. Results and Discussion

3-3-1. Synthesis and Characterization of the ASPI

The chemical structures of the synthesized sulfonated monomer and ASPI characterized by ^{1}H NMR (Figure 3-4 and 3-5). The peaks between δ = 7 to 9 ppm corresponds to the H atoms in the aromatic rings. The aliphatic protons were observed at δ = 2.0−4.4 ppm. Integration of proton peaks in ^{1}H NMR spectra was in good agreement with the number of hydrogen in both the backbone and side chain of ASPI structure. No residual amide and carboxylic protons were observed, which indicates that the imidization reaction was completed. Spectrum is after ion exchanged product. A very small amount of the TEA was observed (ca.1%). FTIR-ATR spectra of the ASPI were shown in Figure 3-6. The absorption bands of the (C=O) were observed at 1720 and 1780 cm^{-1}, which corresponds to the C=O asymmetric and symmetric stretching vibrations in ASPI-2, ASPI-3, and ASPI-4 case. Similar vibrations of the C=O were observed at c.a. 1660 and 1710 cm^{-1} in ASPI-1. The observed vibrational mode at 1500 cm^{-1} is attributed to the phenyl C−C stretching vibration. The vibrational mode at 1380 (in ASPI-2, ASPI-3 and ASPI-4) and 1350 (in ASPI-1) cm^{-1} is C−N bond of the imide groups. The characteristics absorption bands of the sulfonic acid groups (O=S=O) normally appear between 1030 cm^{-1} and 1250 cm^{-1}. Table 1 shows the molecular weight, ionic exchange capacity (IEC), proton conductivity and water uptake.

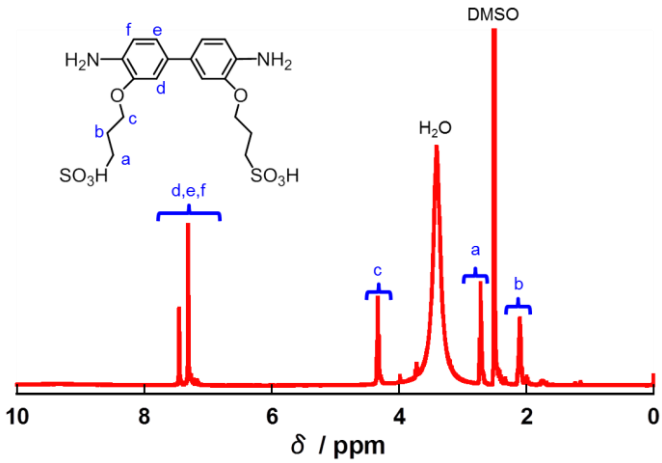

Figure 3-4. ^{1}H NMR (DMSO-d_6) spectra of sulfonated monomer (3, 3'-BSPA).

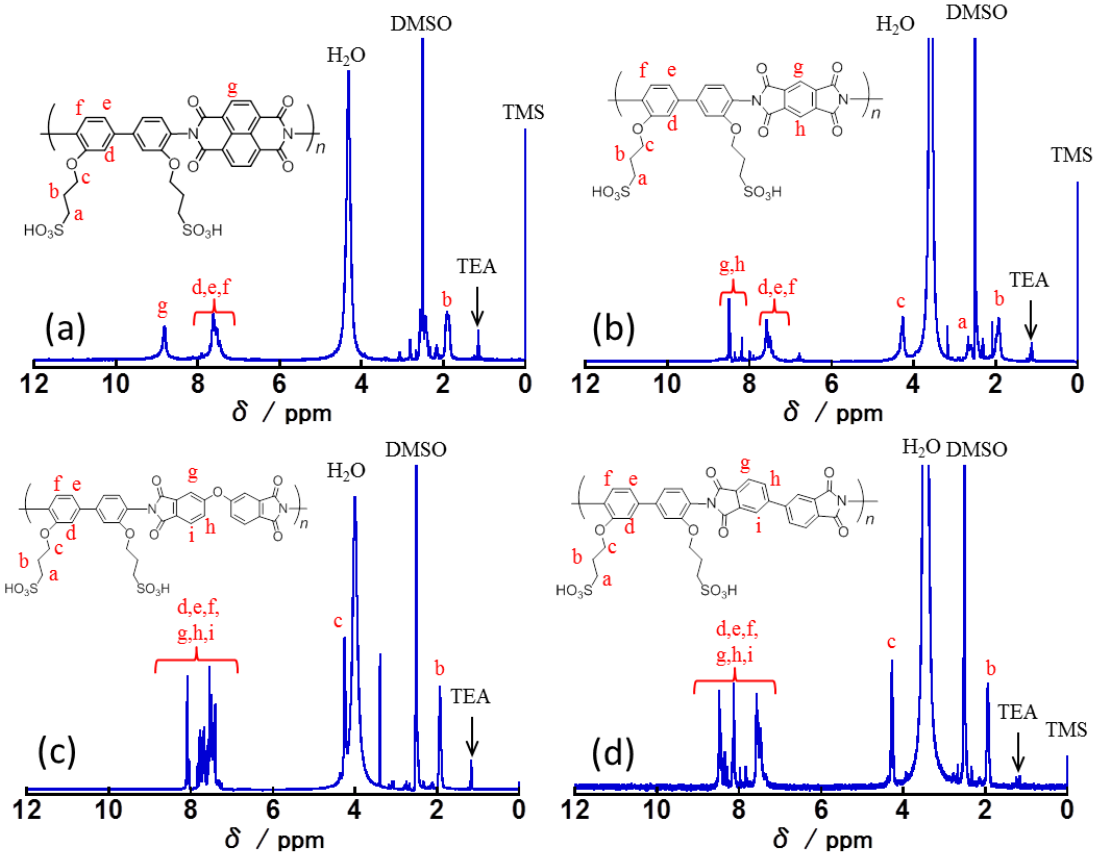

Figure 3-5. ^{1}H NMR (DMSO-d_6) spectra of various sulfonated polyimide. (a)ASPI-1, (b)ASPI-2, (c)ASPI-3, and (d)ASPI-4.

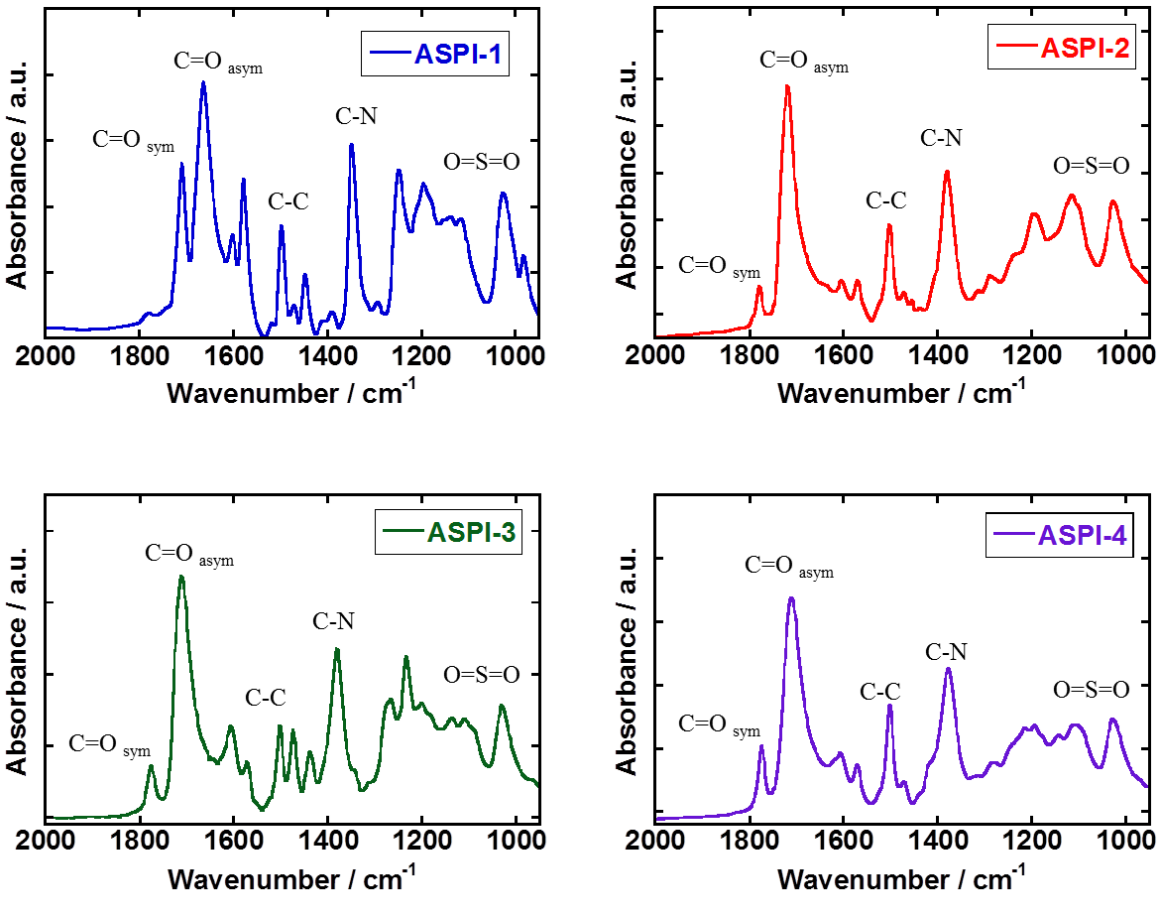

Figure 3-6. FTIR-ATR spectra of the ASPI-1, ASPI-2, ASPI-3, and ASPI-4.

Table 3-1. Physical Properties of ASPI thin films.

Sample	IEC [a] (mequiv/g)	Mw	H^+ conductivity 10^{-1} (S/cm)	Water uptake[b] (%)	λ [b]
ASPI-1	2.89	$4.9x10^5$	1.78	76.8	14.8
ASPI-2	3.11	$8.0x10^5$	1.96	78.7	14.0
ASPI-3	2.72	$6.5x10^5$	0.29	63.3	12.9
ASPI-4	2.78	$5.6x10^5$	0.8	66.0	13.3

[a] IEC calculated from ^{1}HNMR. [b]Proton conductivity, water uptake and λ measured at 95% RH.

3-3-2. Proton conductivity.

The proton conductivity of the ASPI-1, ASPI-2, ASPI-3 and ASPI-4 thin films for various RH at 298 K is shown in Figure 3-7. The proton conductivity of the all ASPI thin films exponentially increased with RH, which is typical phenomenon of proton conductive polymers. High IEC value means high ion concentration, so high proton conduction can be expected. The proton conductivity and IEC value increased in the order of the ASPI-2 (IEC = 3.11) > ASPI-1 (IEC = 2.89) > ASPI-4 (IEC = 2.78) > ASPI-3 (IEC = 2.72). The proton conductivity for all of the ASPI thin films showed the remarkably higher value of above a 10^{-2} S / cm (at 25℃, 95% RH). This proton conductivity is comparable to the typical PEM and Nafion membrane, which indicates that the ASPI thin films can conductive proton as efficiently as state of the art PEM.

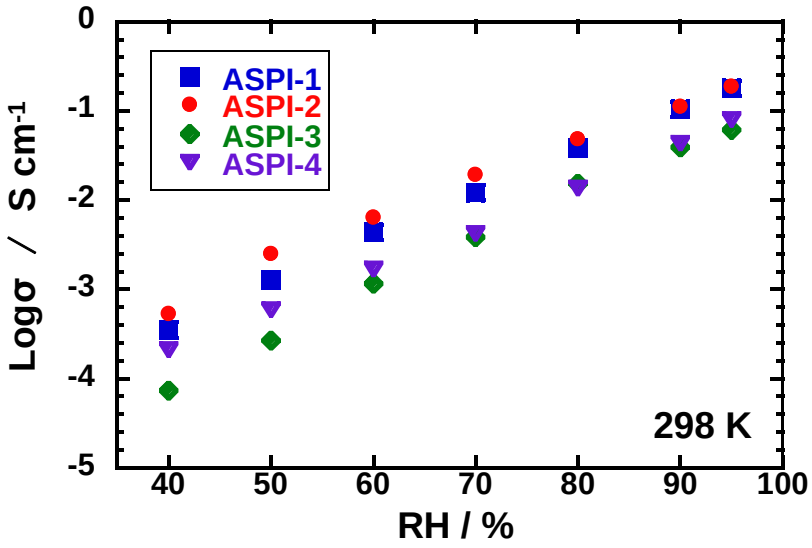

Figure 3-7. Proton conductivity of the ASPI thin films as a function of relative humidity at 298 K.

3-3-3. Water uptake.

The water uptake of the polymer electrolyte membrane is an important factor for the proton conductivity. The RH dependence of water uptake of ASPI-1, ASPI-2, ASPI- 3 and ASPI-4 thin films was investigated for hydration behavior using the in-situ QCM measurements. Figure 3-8 shows the humidity dependence of the water uptake and number of water molecules per sulfonic acid (λ [H_2O / SO_3H]). The water uptake increased with IEC value and humidity. The water uptake almost followed the order of the IEC values (Table 3-1). The λ value of the ASPI thin film is also comparable to or little lower than those of Nafion membrane [43]. Although there are no differences in their λ values at the 20–90% RH, the λ value for ASPI-1 thin film was higher than that for ASPI-2 thin film despite of the lower IEC value.

The proton conductivity and water uptake of the all of the ASPI thin films was almost follows order of the IEC. In other words, if λ value and /or IEC value is same, there is a possibility to show the same proton conductivity. The thresholds of the proton conductivity was observed at the c.a. λ = 5-6.5 (Figure 3-9). Kreuer *et al.* reported that $6H_2O$ molecules are needed to efficiently facilitate proton transport for sulfonated PEM [44].The thresholds of the ASPI thin films are close to this value, which agrees with the results of a studied here. For investigated the state of sulfonic acid groups, *in-situ* FT-IR

measurement was carried out.

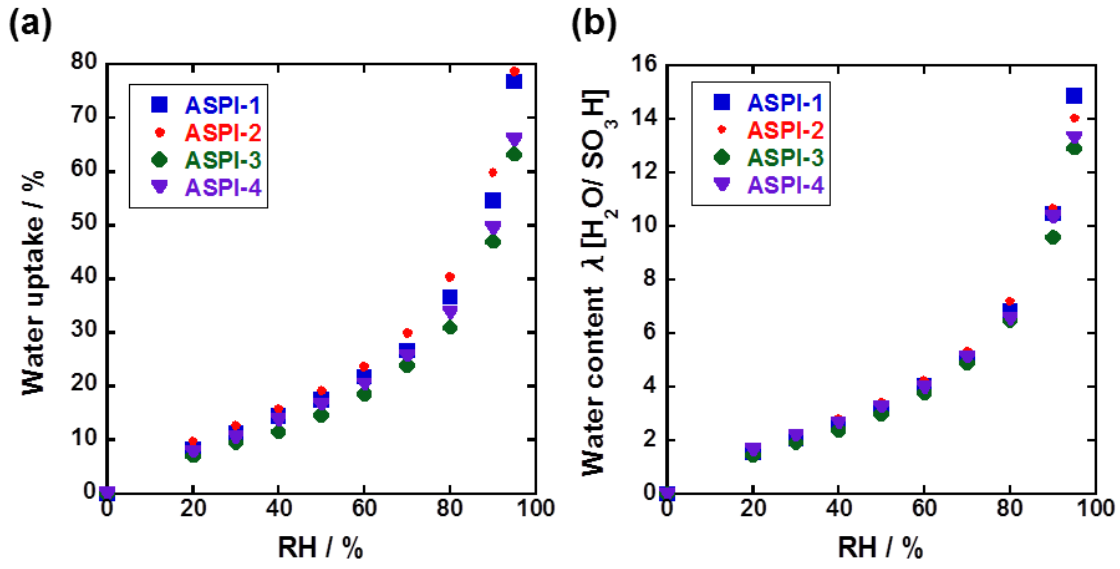

Figure 3-8. (a) Water uptake and (b) number of absorbed water molecules per sulfonic acid group (λ) of the ASPI-1, ASPI-2, ASPI- 3 and ASPI-4 thin films as a function of relative humidity at 298 K.

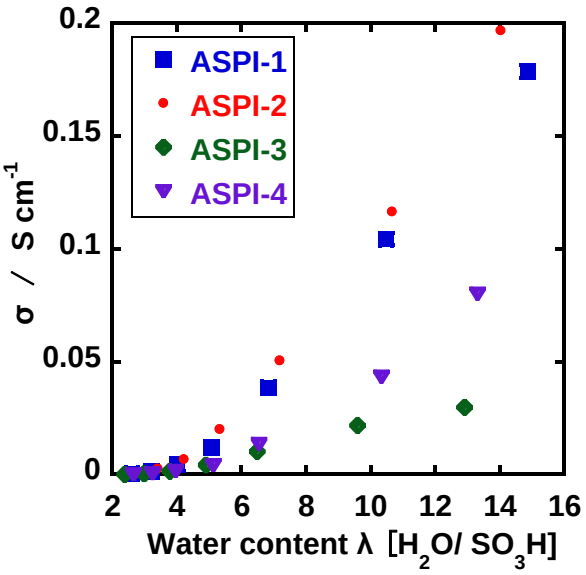

Figure 3-9. Proton conductivity of the ASPI thin films as a function of the λ value.

3-3-4. *in-situ* FT-IR

The *in-situ* FT-IR measurement was investigated for dissociation of the sulfonic acid groups. Figure 3-10 shows RH dependent FT-IR spectra of the ASPI-2 thin film. Fundamentally, the fingerprint region of this spectrum was similar to FT-IR ATR spectra. The observed broad peak at the 3000-3700 cm^{-1} corresponds to OH stretching vibration mode of the water molecular. This absorbance of OH stretching vibration mode increased with RH and water uptake (Figure 3-11 (a)). The absorption bands of the dissociated sulfonic acid groups were observed at 1040 cm^{-1} and 1200 cm^{-1}, which correspond to the SO_3^- symmetric ($v_s(SO_3^-)$) and asymmetric($v_s(SO_3^-)$) stretching vibration modes. These bands of the dissociated sulfonic acid groups also increased with RH and water uptake (Figure 3-11 (b)). However, these trends showed different tendency compared to water uptake and OH stretching vibration mode (ν(OH)). At the low RH region, absorbance of the $\nu_s(SO_3^-)$ drastically increased. Then, absorbance increased gradually up to 70 %RH. Finally, absorbance reached 0.055. The results indicate that dissociation of the sulfonic acid groups almost completed around 70 %RH. The absorbance of the $\nu_s(SO_3^-)$, ν(OH) and proton conductivity are plotted as a function of λ value to estimate conductivity change in terms of dissociation of the sulfonic acid groups in Figure 3-12. The absorbance of the ν(OH) linearly increases with λ value. The dissociation of the sulfonic acid groups almost completed at λ =c.a 5 which drastically

increases proton conductivity. This result indicate that the proton conductivity improves after completed dissociation of the sulfonic acid groups. After completed dissociation of the sulfonic acid groups, additional water uptake can be contributed to development of the proton conduction channels.

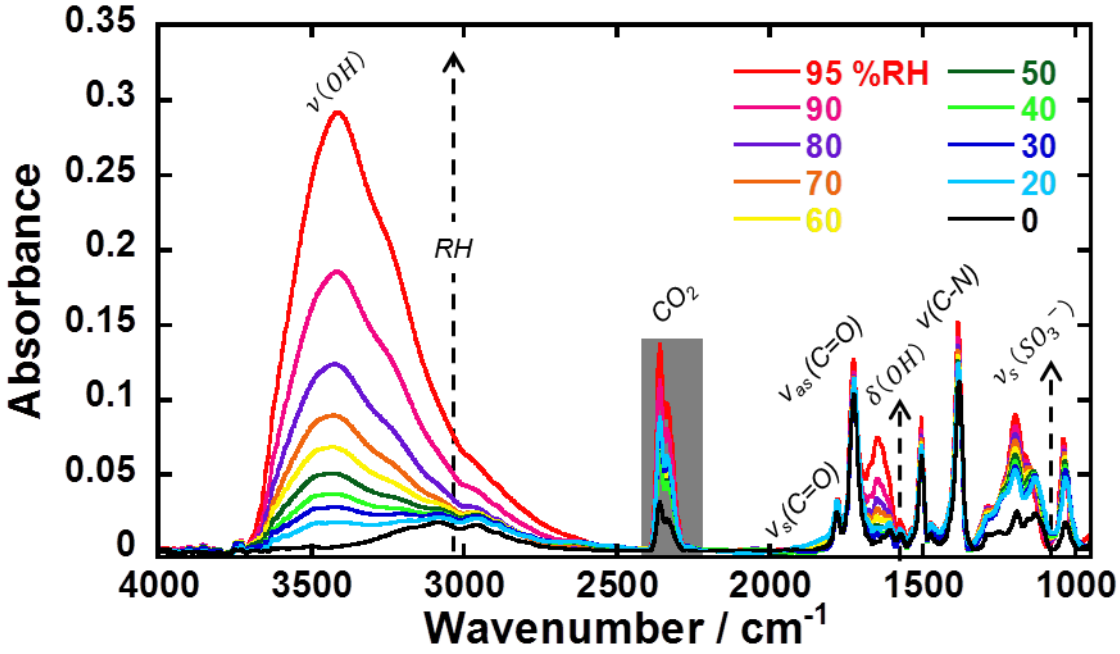

Figure 3-10. *in-situ* FT-IR spectra of the ASPI-2 thin film under RH control .

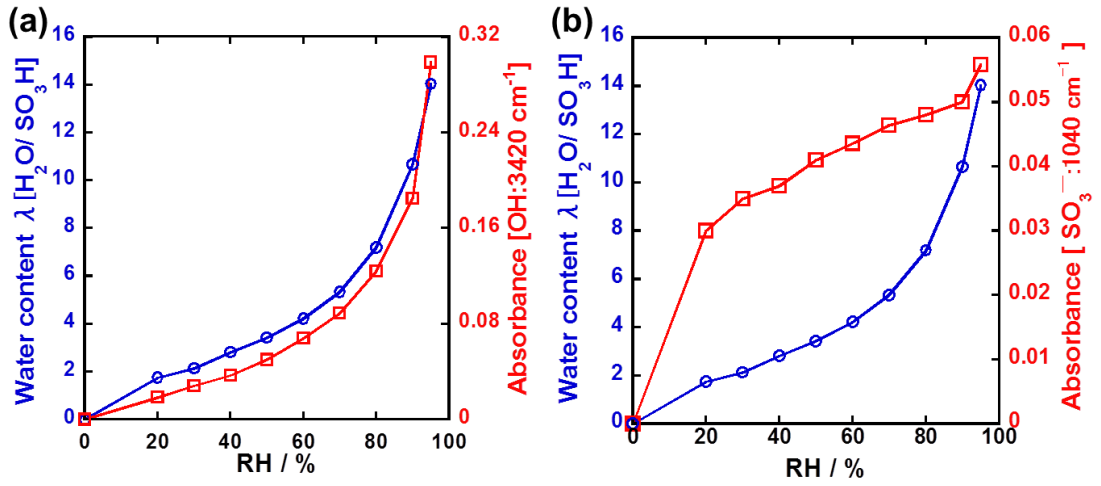

Figure 3-11. RH dependent absorption of (a) OH stretching (3420 cm^{-1}) and (b) SO_3^- symmetric stretching (1040 cm^{-1}).

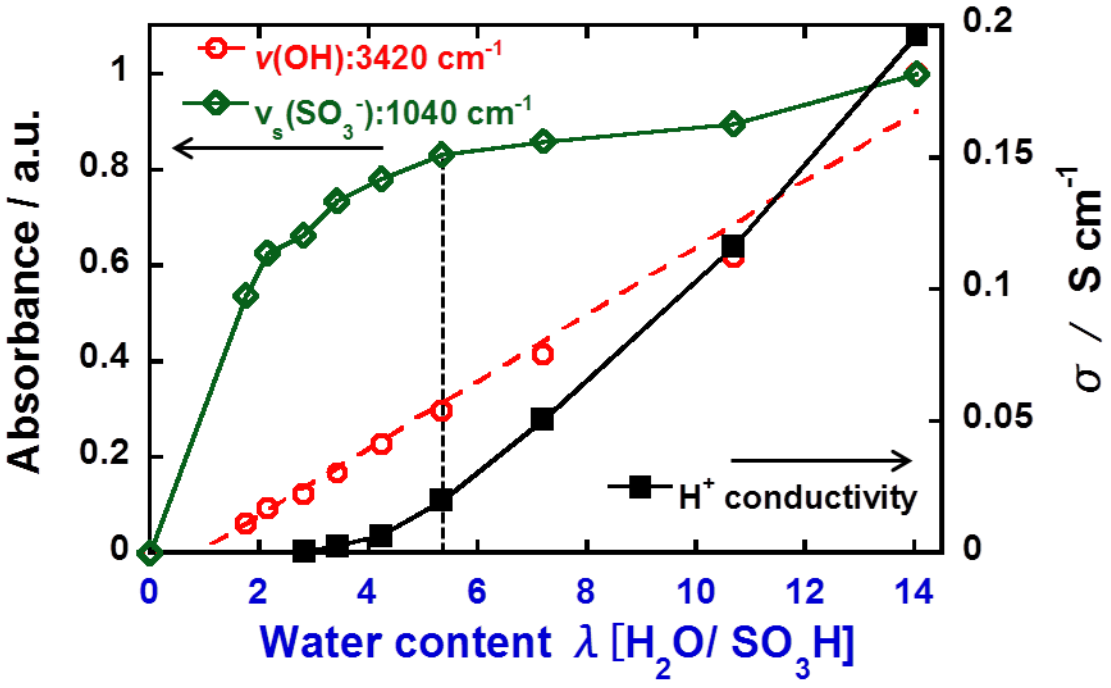

Figure 3-12. Proton conductivity and change of the absorbance of the $\nu_s(SO_3^-)$, ν(OH) as a function of λ value.

3-3-5. LC ordered domain

Figure 3-13 shows the representative POM images of the ASPI-1, ASPI-2, ASPI-3 and ASPI-4 thin films. Rikukawa et al. reported that the sulfonated poly(4-phenoxybenzoyl-1,4-phenylene)s showed the lyotropic nematic phase in DMSO solution [45]. Noteworthy, all ASPI films (not in solution phase) exhibited strong birefringence due to the LC like morphology with large domain. Furthermore, it was demonstrated that there were clear differences for the morphology and domain size due to different polymer structure. Our previous study revealed that the high molecular weight ASPI-2 has large domain size and high proton conductivity compared to low molecular weight ASPI-2 [27]. These results suggest that the LC like morphology and domain size was not only depend on the molecular weight but also influenced by polymer structure. This difference of the morphology and domain size could be affected to internal nanostructure. Therefore, detailed structural analysis was carried out by GI-SAXS measurements.

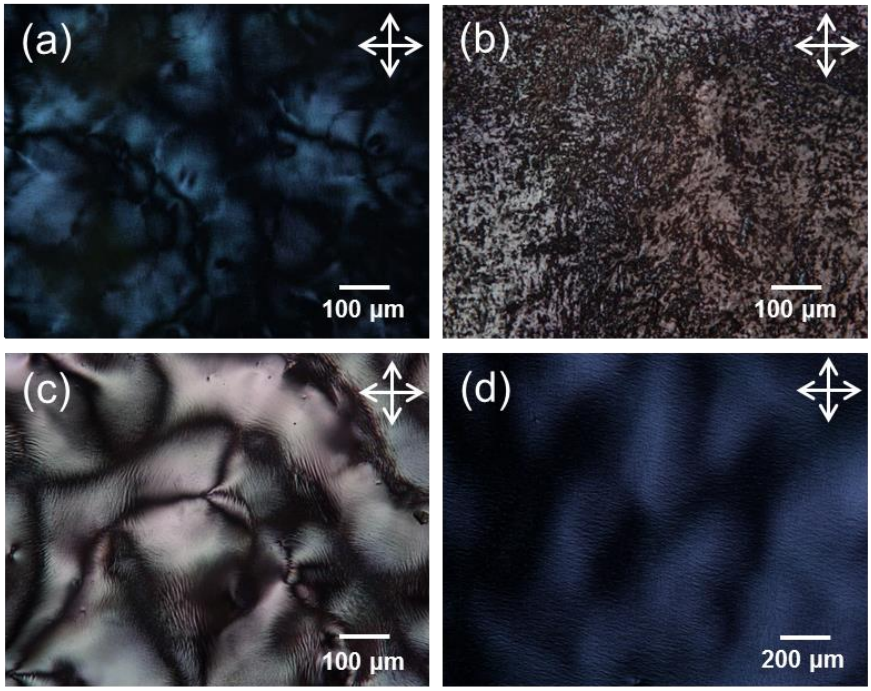

Figure 3-13. Polarized optical microscope images of the ASPI thin films. (a)ASPI-1, (b)ASPI-2, (c)ASPI-3, and (d)ASPI-4.

3-3-6. GI-SAXS

In order to investigate the molecular ordered structure at the various humidity conditions, *in-situ* GI-SAXS measurements were performed for ASPI-1, ASPI-2, ASPI-3, and ASPI-4 thin films. Figure 3-14 shows the 2D GI-SAXS patterns at 0-95% RH and humidity dependent 1D GI-SAXS profiles in the in-plane and out-of-plane directions. The scattering arcs at the positions of q_y = 0.75 and 0.82 $Å^{-1}$ were artifacts caused by diffraction of the windows for the humidity-controlled cell. In the previous

literature of the GI-SAXS measurements (Figure 3-14 (b)), a self-assembled lamellar structure parallel to substrate surface has been determined in the ASPI-2 thin film [25, 27]. This lamellar distance expands to the out-of-plane direction by water uptake (Figure 3-15). And a degree of molecular ordering improves by water uptake based on the lyotropic LC property (Figure 3-16). In the in-plane direction, the insensitive scattering peak (nm) for the humidity change can be observed, which is attributable to the periodic monomer unit length.

In the same manner, ASPI-1 (Figure 3-14 (a)), ASPI-3 (Figure 3-14 (c)) and ASPI-4 (Figure 3-14 (d)) thin films exhibit the same humidity dependent self-assembly structure. The d-spacing and assignment of the peaks were listed in Table 3-2. Qualitatively, similar behavior for enhancing of the molecular ordering and expansion of lamellar structure is seen for all ASPI thin films studied here. On the other hand, π-stacking (d = 0.35 nm) was observed only ASPI-1 thin film. This difference might be derived from the different molecular structure such as naphthalene ring and benzene ring. Generally, π-stacking of the polyimide was observed in highly crystalline structure [46]. Furthermore, scattering peak of π-stacking of the ASPI-1 is enhanced with increasing the humidity. Based on this finding, main chain packing or degree of crystallization of ASPI-1increased with humidity.

In the in-plane direction at the q_y = 0.38 $Å^{-1}$ (d=1.63 nm), the periodic monomer unit length for the polyimide chain units is observed only in ASPI-1 and ASPI-2 thin films. This value is close to periodic monomer unit length estimated from DFT calculation (Figure 3-17). However, higher order peaks were not observed in ASPI-1 and ASPI-2 thin films in the in-plane direction. This result suggests that the main chain orderings parallel to the surface direction is not as high as that of typical aromatic polyimide [46]. In the case of the ASPI-3 and ASPI-4 thin films, diffraction peaks of periodic monomer unit length were not observed because of the main chain was nonplanar molecular structure. The order of the interchain packing in aromatic polyimide considerably according to differences between the planar and nonplanar molecular structure [46]. Therefore, main chain orderings of ASPI-3 and ASPI-4 parallel to the surface direction are significantly lower than those of ASPI-1 and ASPI-2 thin films. Nevertheless, the diffraction peak in the out-of-plane direction as a lamella structure and interchain packing reveals that all ASPI thin films indicate the humid-induced lyotropic lamella structure is oriented parallel to the substrate plane. Ando *et al.* reported the molecular ordered structure of polyimide with nonplanar (bent) molecular structure using detailed GISAXS analysis [46]. The polyimide with nonplanar (bent) molecular structure shows the isotropic order domain [46]. Hence the highly in-plane oriented structure in ASPI-3

and ASPI-4 thin films is not explainable from typical polyimide. This difference might be derived from the presence of the hydrophilic alkyl sulfonated side chains. The amphiphilic polyimide with alkyl sulfonated side chains might promote a favorable structure for in-plane orientation due to the lyotropic LC property. Therefore, highly in-plane orderings of the ASPI thin films are significantly influenced by molecular structure of diamine moiety with alkyl sulfonated side chains. The results of GI-SAXS revealed that all ASPI thin films formed highly in-plane ordered structure, in which lamellar distance expands to the out-of-plane direction and a degree of molecular ordering improves by water uptake (Figure 3-18).

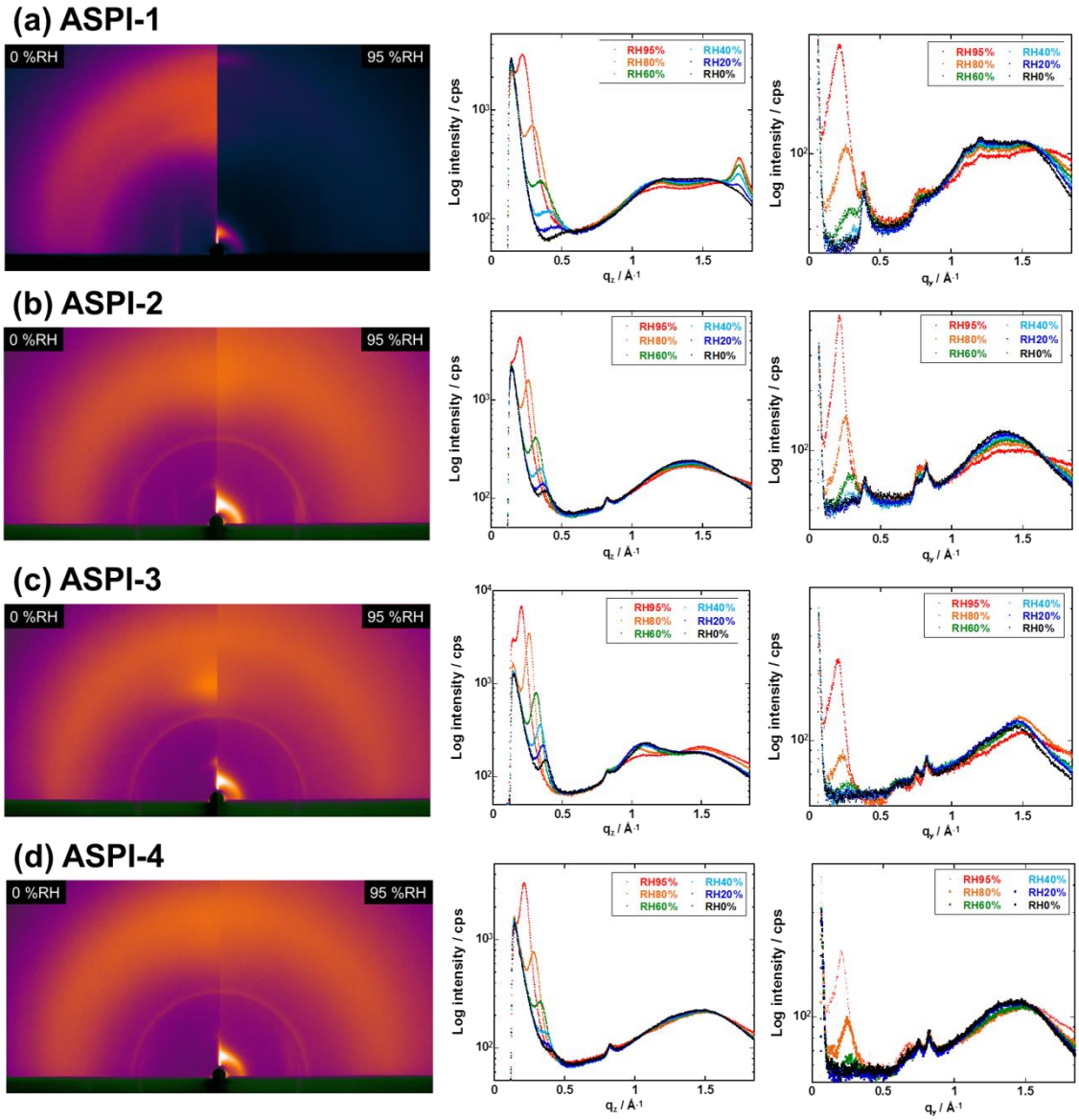

Figure 3-14. The 2D GI-SAXS patterns at 0%RH and 95%RH respectively, and humidity dependent 1D GI-SAXS profiles in the in-plane and out-of-plane directions of the (a) ASPI-1, (b) ASPI-2, (c) ASPI-3, (d) ASPI-4

Table 3-2. d-spacing and assignment in the in-plane (IP) and out-of-plane (OP) directions

Sample	Direction	d-spacing / nm	Assignment

		0% RH	95% RH	
ASPI-1	OP	1.3	2.85	lamellar
	OP	—	0.35	π-stack
	IP	1.6	1.6	(100)
ASPI-2	OP	1.62	3.0	lamellar
	OP	0.44	0.44	ch-pack
	IP	1.6	1.6	(100)
ASPI-3	OP	1.66	3.08	lamellar
	OP	0.56	0.58	ch-pack
ASPI-4	OP	1.52	2.94	lamellar
	OP	0.42	0.42	ch-pack

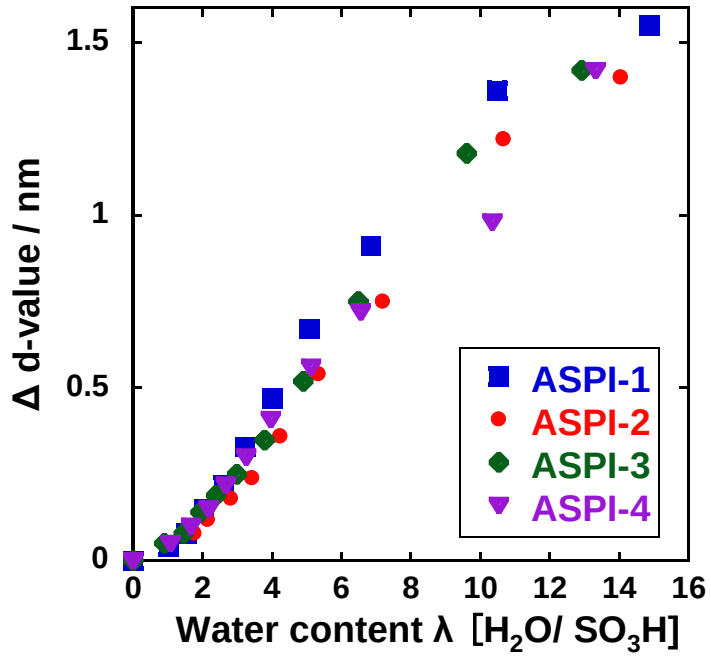

Figure 3-15. Lamella distance for ASPI-1, ASPI-2, ASPI-3, and ASPI-4 thin films as a function of relative humidity at 298 K.

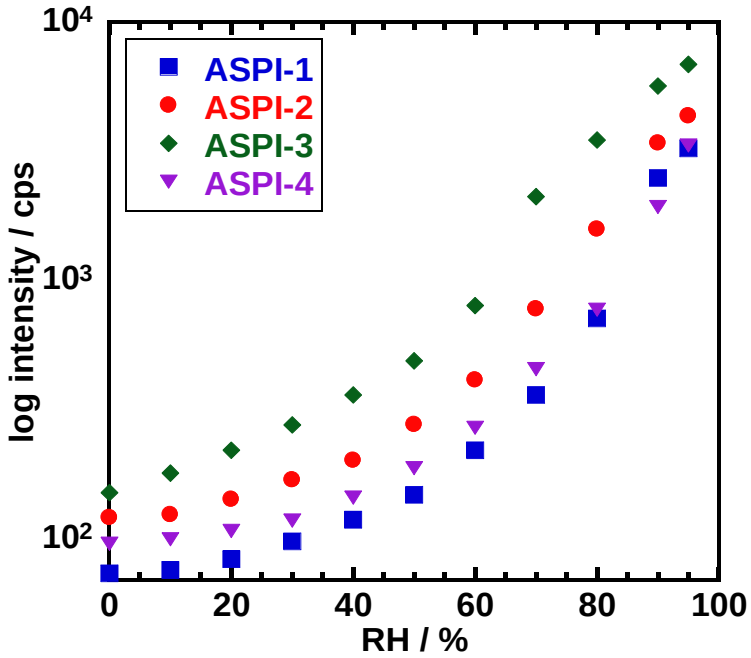

Figure 3-16. Scattering intensity of the lamella structure for ASPI-1, ASPI-2, ASPI-3, and ASPI-4 thin films as a function of relative humidity at 298 K.

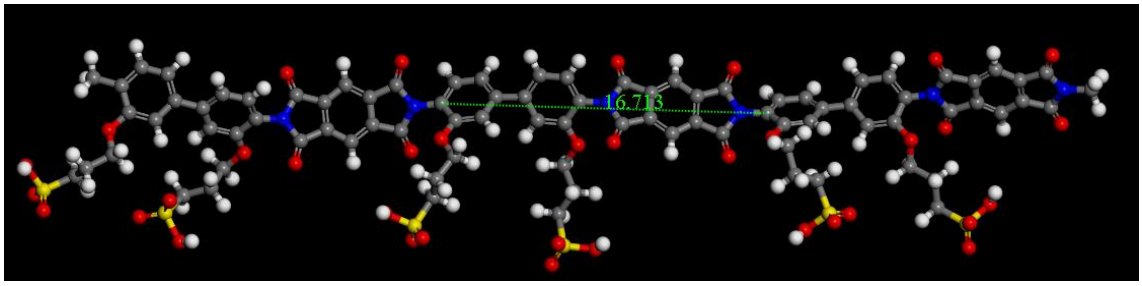

Figure 3-17. Optimized structure model of the ASPI-2 obtained by DFT calculation.

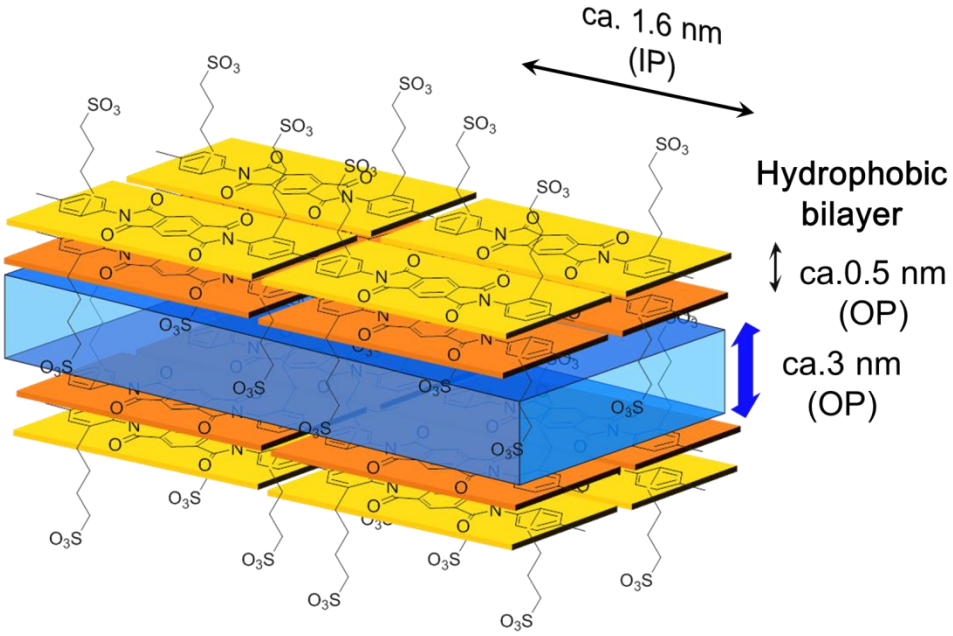

Figure 3-18. Schematic illustration of ASPI thin film structure.

The above structural data are consistent with all ASPI thin films enhancing of the molecular ordering and expansion of lamellar structure by water uptake. These results indicate that all ASPI thin films are inherent in high proton conductive channel with water nanochanel. In addition, high proton conduction was achieved at more than λ = 5 (ASPI-1), 5.3 (ASPI-2), 6.5 (ASPI-3) and 6.5 (ASPI-4) respectively. Similar trends were observed in relationship between λ value and scattering intensity of the lamellar structure (Figure 3-19). The obtained results show a significant increase in scattering intensity as λ value increase, in particular for above c.a. λ = 6. These results suggest that the proton conductivity depends on not only the water uptake but also degree of the molecular ordering.

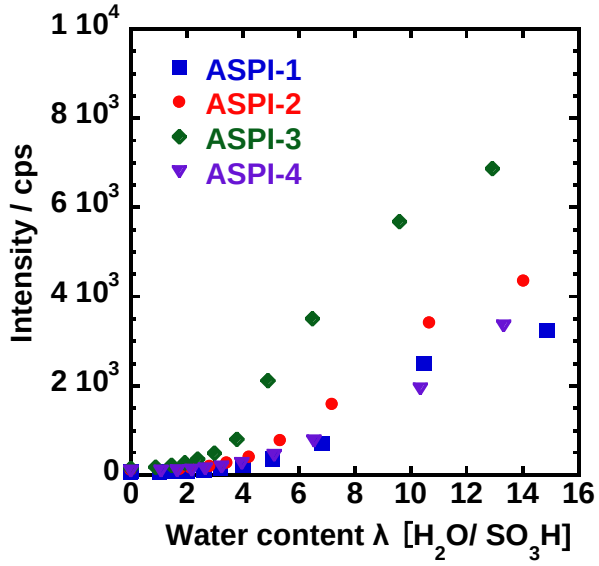

Figure 3-19. Scattering intensity of the ASPI thin films as a function of the λ value.

3-3-7. Characterization of the sheared ASPI film

For further detailed structural analysis, characterization of ASPI sheared film was carried out by additional analysis. Figure 3-20 shows the polarized FT-IR spectra of an ASPI-2 sheared film with polarized light orthogonal and parallel to the applied shear direction. The spectra of the ASPI-2 sheared film show highly dichroism. A large difference between orthogonal and parallel spectra demonstrates the uniaxial orientation of the film. The effect of molecular orientations have on the degree of alignment during film can be quantified by comparing the resulting absorbance dichroism. The observed vibrational modes at 1380 and 1500 cm^{-1} are assigned respectively to the C–N bonds of the imide groups and to phenyl C–C stretching vibration. Adjacent vibrational modes at 1720 and 1780 cm^{-1} correspond to the C═O asymmetric and symmetric stretching vibrations of imide groups, respectively. The absorbance dichroism was estimated according to the following equation

$$S = (A_{Para.} - A_{ortho.})/(A_{Para.} + 2A_{ortho.})$$

Where $A_{para.}$ and $A_{ortho.}$ are absorbance of the orthogonal and parallel to the applied shear direction respectively and *S* is order parameter. A large difference of the order parameter was found a C═O asymmetric and C–N bond of the imide groups (Table 3-3). The vibrational mode of the former corresponds to the orthogonal to the main chain

direction. The latter mode corresponds to the parallel to main chain direction. These results indicate that the main chains of ASPI-2 sheared film are oriented parallel to applied shear direction (Figure3-21).

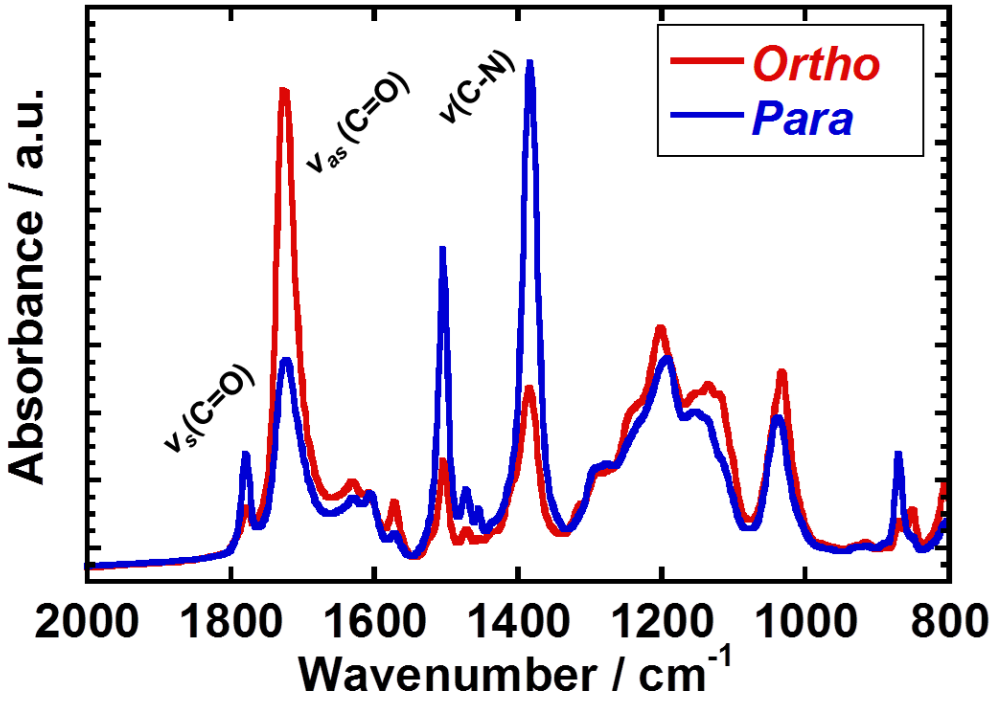

Figure 3-20. Polarized FT-IR spectra of an ASPI-2 sheared film.

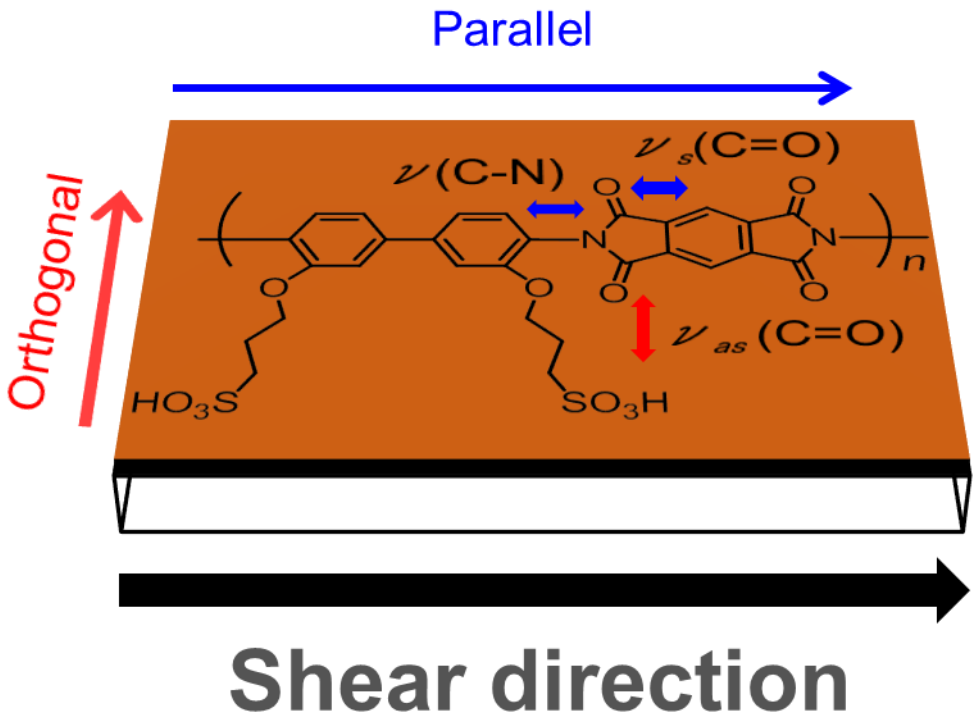

Figure 3-21. Relationship between shearing direction and main chain orientation.

Table 3-3 Order parameter of the ASPI-2 sheared film.

Wavenumber	Assignment	Order parameter
1380 cm^{-1}	ν(C–N)	0.323
1720 cm^{-1}	ν_{as}(C═O)	0.141
1780 cm^{-1}	ν_{s}(C═O)	-0.209

Figure 3-22 shows POM images of a sheared film of ASPI-2 on CaF_2 substrate. The macroscopic alignment and LC like morphology can clearly be seen in POM images. LC like morphology is aligned parallel to the shear direction as indicated by the arrow.

These results support that the ASPI-2 sheared film is oriented parallel to applied shear direction.

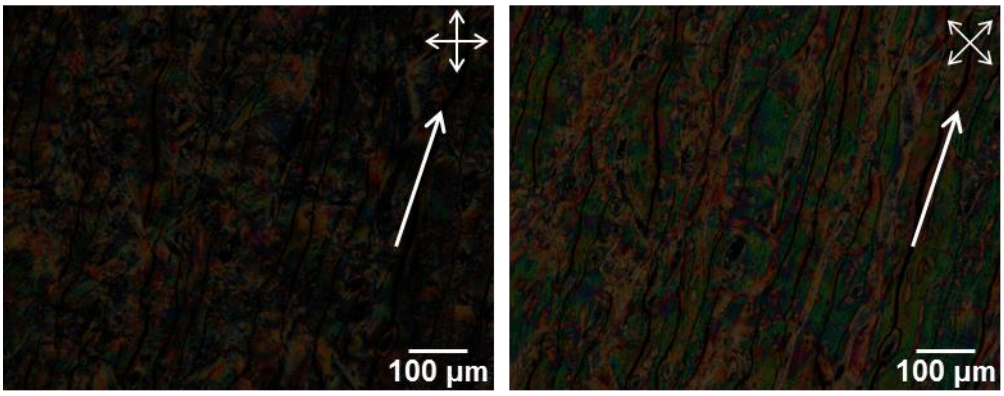

Figure 3-22. POM images of the shear aligned film of ASPI-2 on CaF_2 substrate. The shear direction indicates by the white arrow.

Figure 3-23 shows the 2D GI-SAXS patterns at 0, 95% RH and 1D GI-SAXS profiles in the in-plane and out-of-plane directions of the ASPI-2 sheared film with X-ray incident parallel and orthogonal to the shear direction. In the both parallel and orthogonal directions, diffraction peak in the out-of-plane direction as a lamella structure and interchain packing appeared at $q_z = 0.5$ and c.a.1.3 $Å^{-1}$ which corresponds to the d-value of the 1.26 and 0.47 nm respectively. At the 95% RH, these lamellar distances expanded to the out-of-plane direction at the $q_z = 0.22$ (d=2.8 nm). The similar behavior for enhancing of the molecular ordering and expansion of lamellar structure is seen for spin-coat film. The 2D GI-SAXS image of the sheared film shows a lamellar

spacing similar to the spin-coated thin films.

In the in-plane direction at the q_y = 0.375 $Å^{-1}$ (d=1.66 nm), 0.78 $Å^{-1}$ (d=0.81 nm) and 1.52 $Å^{-1}$ (d=0.41 nm) the periodic monomer unit length for the polyimide chain units is observed in the orthogonal direction at both 0 and 95% RH. The diffraction peaks of periodic monomer unit length were not observed in out-of-plan direction and parallel direction to the shear direction. The absence of peak for periodic monomer unit length out-of-plan direction and parallel direction to the shear direction indicates that the main chains of ASPI-2 are highly oriented parallel to the shear direction (Figure 3-24 (a)). Furthermore, the scattering peak of lamella structure and interchain packing in the 2D GI-SAXS pattern of parallel direction to the shear direction exhibited an isotropic scattering arc compared with that of orthogonal directions. At the 95% RH, the scattering peak of lamella structure in parallel direction clearly exhibits an isotropic scattering arc, which demonstrates that the polymer orientation possesses isotropically to orthogonal direction (Figure 3-24 (b)).

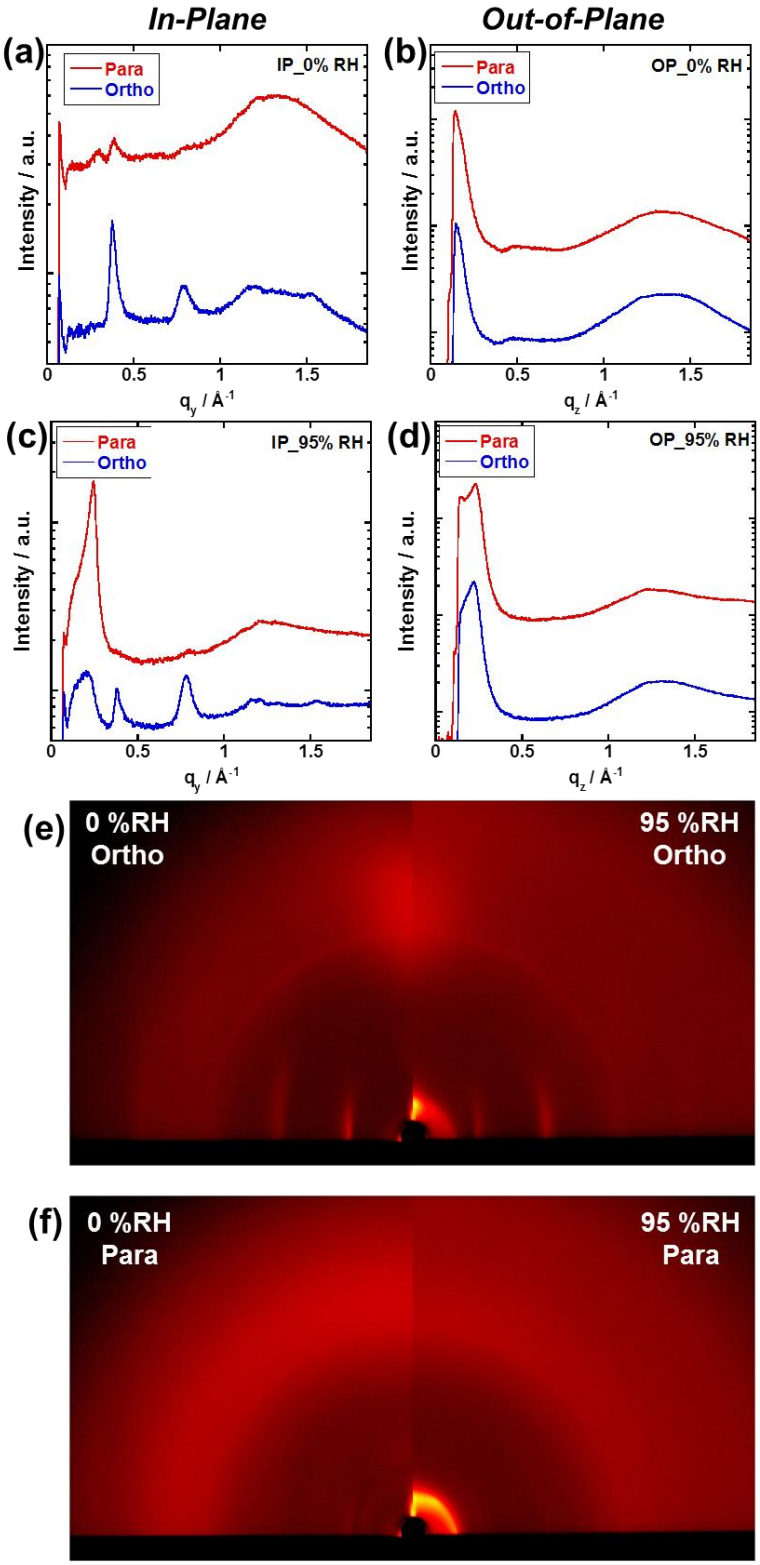

Figure 3-23. The 1D GI-SAXS profiles in the (a), (c) in-plane, (b), (d) out-of-plane directions and 2D GI-SAXS patterns with (e) orthogonal, (f) parallel direction of the ASPI-2 sheared film at 0 and 95 %RH.

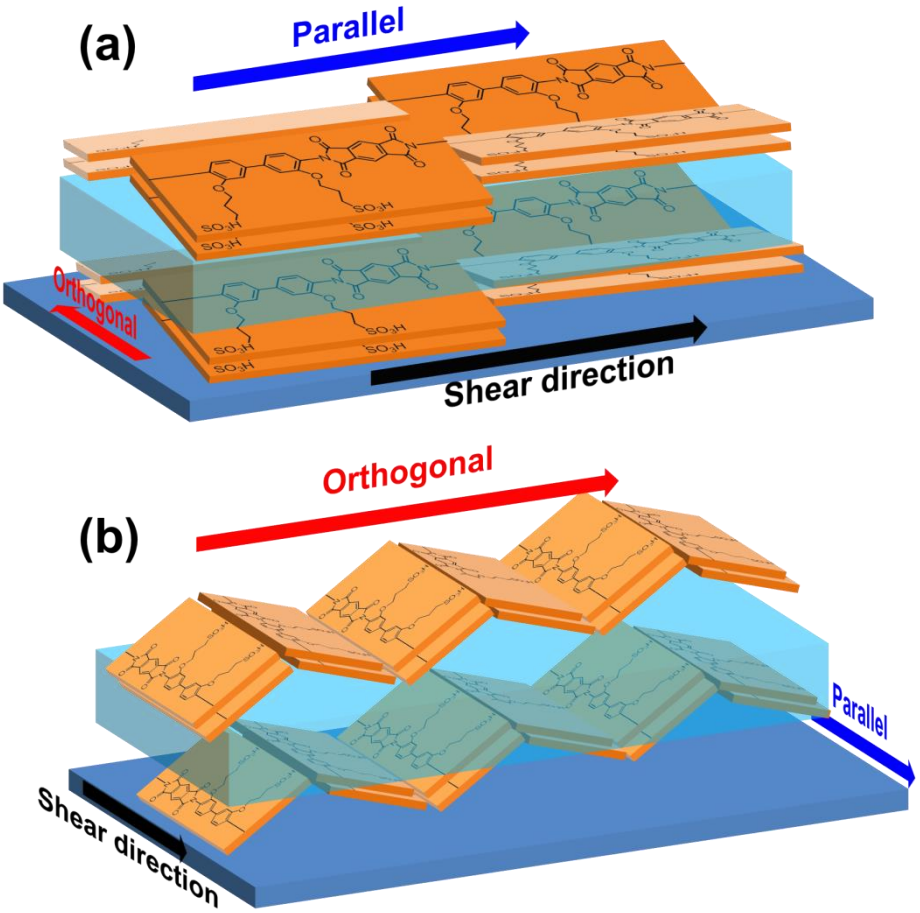

Figure 3-24. Schematic illustration of main chain orientation model in ASPI-2 sheared film.

3-3-8. Solution property in ASPI

The solution state in the ASPI-2 was investigated for effect of concentration using POM. Figure 3-25 shows POM images of various concentration of the ASPI-2 solution in H_2O and THF mixed solvent. The concentration of the 10 and 15 wt% solution exhibit strong birefringence and LC like texture in solvents. This distinctly indicates that ASPI-2 solution is lyotropic solution. Moreover, these textures similar to ASPI-2 sheared film prepared using similar concentration. On the other hand, POM images of the 5 wt% solution increased dark area, and finally LC like texture disappeared in 2.5wt% solution. The dark area can be consider to optically isotropic part because molecules disperse randomly at low concentration. This transition might be explainable as different LC phase by the different concentration due to lyotropic LC property. The ASPI-2 thin film shows still highly concentration (c.a.60 wt%) at the high RH region (Figure 3-26) compared to solution state (15 wt%). These results indicate that the solution state of the ASPI above 10 wt% shows the ordered lyotropic LC property.

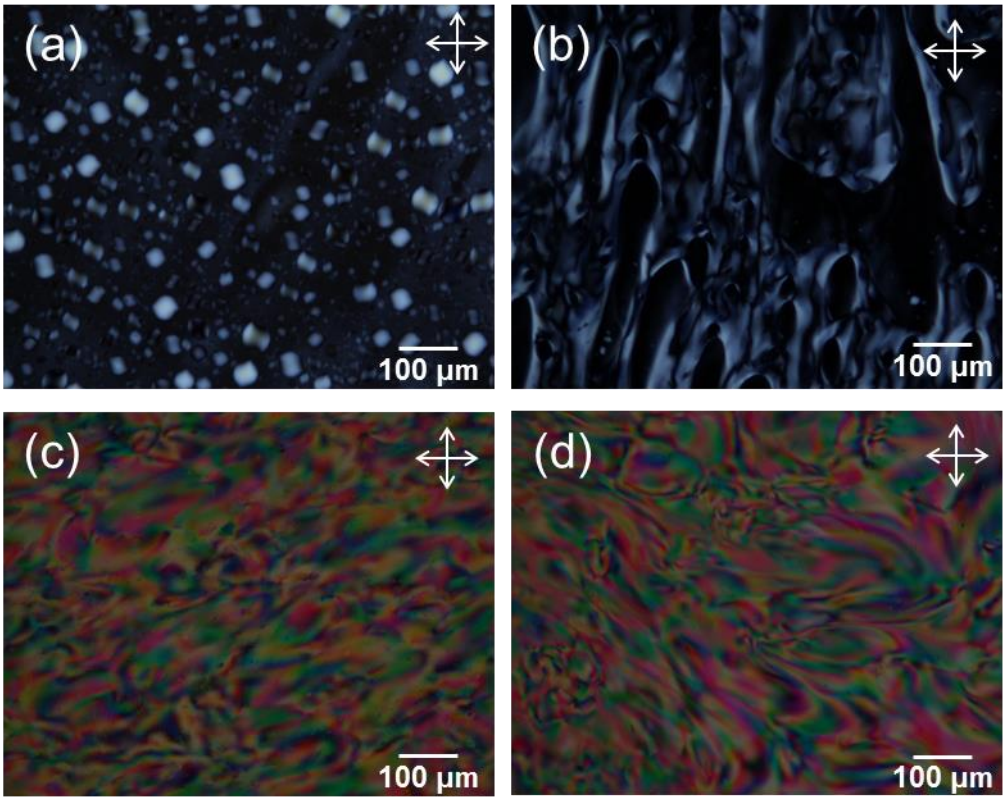

Figure 3-25. POM images of the ASPI-2 solution in H_2O and THF mixed solvent. (a) 2.5 wt%, (b) 5 wt%, (c) 10 wt% and (d) 15 wt%.

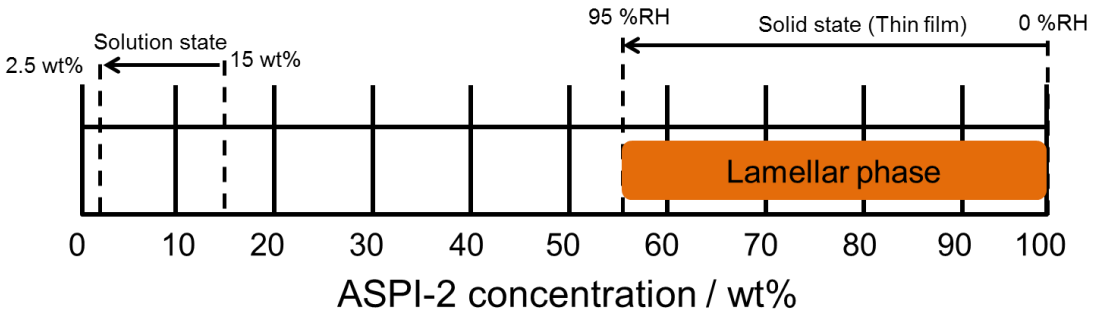

Figure 3-26. Lyotropic liquid crystalline behavior of ASPI-2.

3-3-9. Molecular oriented structure by pMAIRS

IR pMAIRS is increasingly regarded as a powerful spectroscopic tool for revealing molecular orientation in thin films [47-49]. The pMAIRS analysis showed that in-plane (IP) and out-of-plane (OP) transition dipoles are distinguishable in an identical infrared transparent substrate. Figure 3-27 shows pMAIR spectra of the ASPI-1, ASPI-2, ASPI-3, ASPI-4 thin films. The observed vibrational modes of the ASPI-2, ASPI-3, ASPI-4 at 1380 and 1500 cm^{-1} are assigned respectively to the C–N bonds of the imide groups and to phenyl C–C stretching vibration. Adjacent vibrational modes at 1720 and 1780 cm^{-1} correspond to the C═O asymmetric and symmetric stretching vibrations of imide groups, respectively. In a similar manner, pMAIRS spectra of the ASPI-1 shows the C–N bonds, C–C stretching vibration, C═O asymmetric and symmetric stretching vibrations were observed at the 1350, 1500, 1680 and 1720 cm^{-1} respectively.

The relative intensity between the in-plane and out-of-plane vibrational modes of pMAIR spectra was depend on the molecular orientation. A large difference between in-plane and out-of-plane spectra demonstrates the anisotropic orientation of the thin film. In the all thin films, at the C–N bonds, C–C stretching vibration gave the stronger intensity in the 2 × IP spectrums than in the intensity of the OP spectrum. This result indicates that the main chains of all ASPI thin films are oriented parallel to the surface.

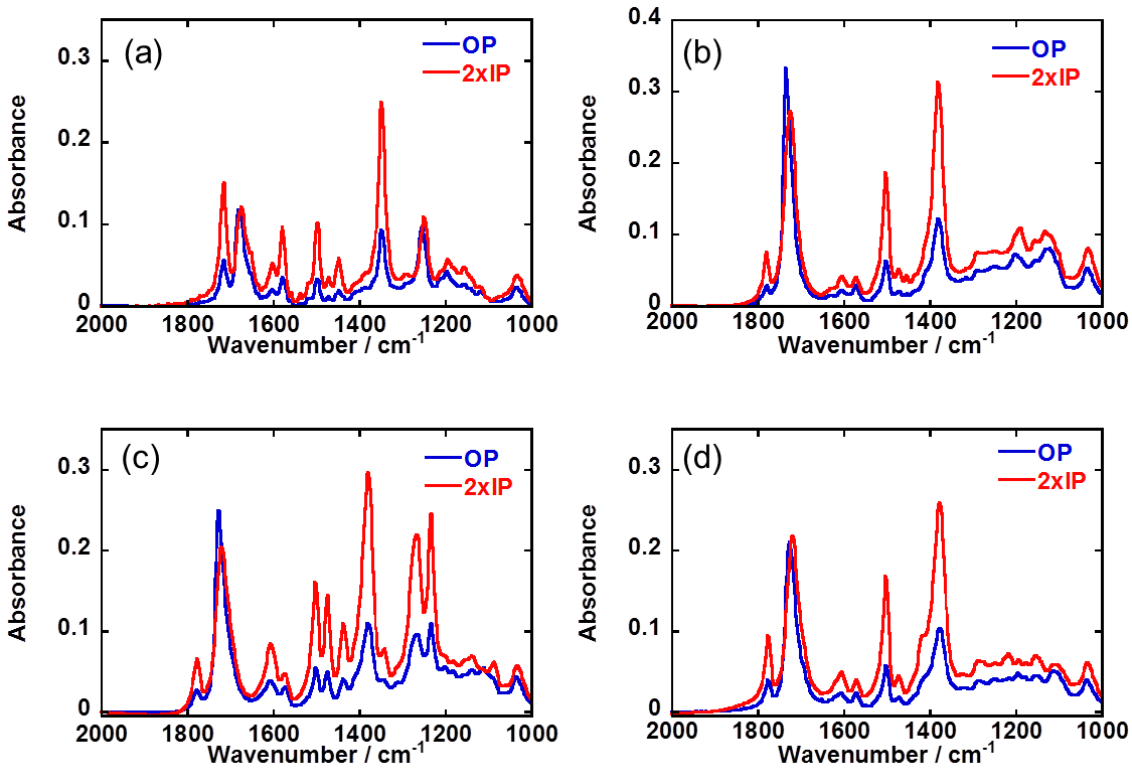

Figure 3-27. pMAIRS pectra of the (a) ASPI-1, (b) ASPI-2, (c) ASPI-3, (d) ASPI-4 thin films.

3-10. Conclusion

Highly ordered structure and high proton conductive material may present opportunities to investigate the relationship between the structure and proton conductivity. This work demonstrated that the ordering structure strongly affects to the proton conductivity. This study investigated the relationship between the proton transport property and organized polymer nanostructure using the sulfonated polyimide with alkyl side chain (ASPI) thin films. All ASPI thin films exhibited the LC like morphology, and different morphology and domain size due to different molecular structure. These organized lamellar structure with highly oriented ASPI thin films achieved high proton conductivity (above 10^{-2} S/cm). The degree of the molecular ordering of those hydrated domains increased with proton conductivity. The main chain orderings of nonplanar polymer backbone parallel to the surface direction are significantly lower than those of planar polymer backbone. However, lamella structure and interchain packing reveal that all ASPI thin films indicate the humid-induced lyotropic lamella structure, which is oriented parallel to the substrate plane.

I propose that the proton conductivity depends on not only the water uptake but also degree of the molecular ordering.

References

[1] Li, N.; Guiver, M. D.Ion Transport by Nanochannels in Ion-Containing Aromatic Copolymers. *Macromolecules* **2014**, 47, 2175– 2198.

[2]He, G.; Li, Z.; Zhao, J.; Wang, S.; Wu, H.; Guiver, M. D.; Jiang, Z. Nanostructured Ion-Exchange Membranes for Fuel Cells: Recent Advances and Perspectives. *Adv. Mater.* **2015**, 27, 5280– 5295.

[3] Shin, D. W.; Guiver, M. D.; Lee, Y. M. Hydrocarbon-Based Polymer Electrolyte Membranes: Importance of Morphology on Ion Transport and Membrane Stability. Chemical Reviews **2017**, 117, 2175– 2198.

[4] Rikukawa, M.; Sanui, K.Proton-conducting polymer electrolyte membranes based on hydrocarbon polymers. *Prog. Polym. Sci.***2000**, 25, 1463–1502.

[5] Miyatake, K.; Bae, B.; Watanabe, M.Fluorene-containing cardo polymers as ion conductive membranes for fuel cells. *Polym. Chem.***2011**, 2, 1919–1929

[6] Mauritz, K. A.; Moore, R. B. State of Understanding of Nafion. *Chem. Rev.* **2004**, *104*, 4535-4585.

[7] Schmidt-Rohr, K.; Chen, A. Q. Parallel Cylindrical Water Nanochannels in Nafion Fuel-Cell Membranes. *Nature Mater*. **2008**, 7, 75-83.

[8] Gebel, G.; Diat, O. Neutron and X-ray Scattering: Suitable Tools for Studying

Ionomer Membranes. *Fuel Cells* **2005**, *5*, 261-276.

[9] Hsu, W. Y.; Gierke, T. D. Ion Transport and Clustering in Nafion Perfluorinated Membranes. *J. Membr. Sci*. **1983**, *13*, 307-326.

[10] Kreuer, K. D. On the Development of Proton Conducting Polymer Membranes for Hydrogen and Methanol Fuel Cells. *J. Membr. Sci.* **2001**, *185*, 29-39.

[11] Kim, Y. S.; Dong, L. M.; Hickner, M. A.; Glass, T. E.; Webb, V.; McGrath, J. E. State of Water in Disulfonated Poly(arylene ether sulfone) Copolymers and a Perfluorosulfonic Acid Copolymer (Nafion) and Its Effect on Physical and Electrochemical Properties. *Macromolecules*, **2007**, *40*, 3886–3890.

[12] Hickner, M. A.; Ghassemi, H.; Kim, Y. S.; Einsla, B. R.; McGrath, J. E.Alternative Polymer Systems for Proton Exchange Membranes (PEMs). *Chem. Rev.* **2004**, *104*, 4587–4611.

[13] Miyatake, K.; Chikashige, Y.; Watanabe, M. Tuned Polymer Electrolyte Membranes Based on Aromatic Polyethers for Fuel Cell Applications. *J. Am. Chem. Soc.*, **2007**, *129*, 3879–3887

[14] Bae, B.; Miyatake, K.; Watanabe, M.Sulfonated Poly(arylene ether sulfone ketone) Multiblock Copolymers with Highly Sulfonated Block. Synthesis and Properties. *Macromolecules* **2010**, *43*, 2684–2691.

[15] Wang, C.; Li, N.; Shin, D. W.; Lee, S. Y.; Kang, N. R.; Lee, Y. M.; Guiver, M. D.Fluorene-Based Poly(arylene ether sulfone)s Containing Clustered Flexible Pendant Sulfonic Acids as Proton Exchange Membranes. *Macromolecules* **2011**, *44*, 7296–7306.

[16] Li, N.; Guiver, M. D. Ion Transport by Nanochannels in Ion-Containing Aromatic Copolymers. *Macromolecules* **2014**, *47*, 2175–2198.

[17] Chang, Y. ;Brunello, G. F. ;Fuller, J. ;Hawley, M. ;Kim, Y. S. Disabb-Miller, M. ;Hickner, M. A. Jang, S. S. ;Bae, C. S. Aromatic Ionomers with Highly Acidic Sulfonate Groups: Acidity, Hydration, and Proton Conductivity. *Macromolecules* **2011**, *44*, 8458– 8469.

[18] Chang, Y. ;Mohanty, A. D. ;Smedley, S. B. ;Abu-Hakmeh, K. ;Lee, Y. H. ;Morgan, J. E. ;Hickner, M. A. ;Jang, S. S. ;Ryu, C. Y. ;Bae, C.

Effect of Superacidic Side Chain Structures on High Conductivity Aromatic Polymer Fuel Cell Membranes. *Macromolecules* **2015**, *48*, 7117–7126.

[19] Ono, Y.; Nagao, Y. Interfacial Structure and Proton Conductivity of Nafion at the Pt-Deposited Surface. *Langmuir* **2016**, *32*, 352–358.

[20] Nagao, Y. Proton Transport Property of Nafion Thin Films on MgO(100) with Anisotropic Molecular Structure. *e-J. Surf. Sci. Nanotechnol*. **2012**, *10* 114–116.

[21] Nagao, Y. Highly Oriented Sulfonic Acid Groups in a Nafion Thin Film on Si

Substrate. *J. Phys. Chem. C* **2013**, *117*, 3294-3297.

[22]Ono, Y.; Nagao, Y.Interfacial Structure and Proton Conductivity of Nafion at the Pt-Deposited Surface. *Langmuir* **2016**, 32 352– 358.

[23]Sato, T.; Hayasaka, Y.; Mitsuishi, M.; Miyashita, T.; Nagano, S.; Matsui, J.High Proton Conductivity in the Molecular Interlayer of a Polymer Nanosheet Multilayer Film. *Langmuir* **2015**, *31* 5174– 5180.

[24] Matsui, J.; Miyata, H.; Hanaoka, Y.; Miyashita, T.Layered Ultrathin Proton Conductive Film Based on Polymer Nanosheet Assembly. *ACS Appl. Mater. Interfaces* **2011**, *3* 1394–1397.

[25] Krishnan, K.; Iwatsuki, H.; Hara, M.; Nagano, S.; Nagao, Y.Proton Conductivity Enhancement in Oriented, Sulfonated Polyimide Thin Films. *J. Mater. Chem. A* **2014**, 2, 6895– 6903.

[26] Krishnan, K.; Ymada, T.; Iwatsuki, H.; Hara, M.; Nagano, S.; Otsubo, K.; Sakata, A.; Kitagawa, H.; Nagao, Y. Influence of Confined Polymer Structure on Proton Transport Property in Sulfonated Polyimide Thin Films. *Electrochemistry* **2014**, *82*, 865-869.

[27] Krishnan, K.; Iwatsuki, H.; Hara, M.; Nagano, S.; Nagao, Y. Influence of Molecular Weight on Molecular Ordering and Proton Transport in Organized Sulfonated

Polyimide Thin Films *J. Phys. Chem. C* **2015**, *119*, 21767–21774.

[28]Yabu, H.; Matsui, J.; Hara, M.; Nagano, S.; Matsuo, Y.; Nagao, Y.Proton Conductivities of Lamellae-Forming Bioinspired Block Copolymer Thin Films Containing Silver Nanoparticles. *Langmuir* **2016**, *32*, 9484–9491.

[29] Kongkanand, A.Interfacial Water Transport Measurements in Nafion Thin Films Using a Quartz-Crystal Microbalance. *J. Phys. Chem. C* **2011**, *115*, 11318– 11325.

[30] Holdcroft, S.Fuel Cell Catalyst Layers: A Polymer Science Perspective *Chem. Mater.* **2014**, *26*, 381– 393.

[31] Paul, D. K.; Karan, K.; Docoslis, A.; Giorgi, J. B.; Pearce, J. Characteristics of Self-Assembled Ultrathin Nafion Films. *Macromolecules* **2013**, *46*, 3461– 3475.

[32] Paul, D. K.; Fraser, A.; Karan, K.Towards the Understanding of Proton Conduction Mechanism in PEMFC Catalyst Layer: Conductivity of Adsorbed Nafion Films *Electrochem. Commun.* **2011**, *13*, 774–777.

[33] Paul, D. K.; Karan, K.Conductivity and Wettability Changes of Ultrathin Nafion Films Subjected to Thermal Annealing and Liquid Water Exposure. *J. Phys. Chem. C* **2014**, 118, 1828–1835.

[34] Dura, J. A.; Murthi, V. S.; Hartman, M.; Satija, S.; Majkrzak, C. F.Multilamellar Interface Structures in Nafion*Macromolecules* **2009**, 42, 4769– 4774.

[35] Ogata, Y.; Kawaguchi, D.; Yamada, N. L.; Tanaka, K.Multistep Thickening of Nafion Thin Films in Water. *ACS Macro Lett.* **2013**, *2*, 856– 859.

[36]Bass, M.; Berman, A.; Singh, A.; Konovalov, O.; Freger, V.Surface-Induced Micelle Orientation in Nafion Films. *Macromolecules* **2011**, 44, 2893– 2899.

[37] Modestino, M. A.; Paul, D. K.; Dishari, S.; Petrina, S. A.; Allen, F.; Hickner, M. A.; Karan, K.;Segalman, R. A.; Weber, A. Z.Self-Assembly and Transport Limitations in Confined Nafion Films. *Macromolecules* **2013**, 46, 867– 873.

[38] Kusoglu, A.; Kushner, D.; Paul, D. K.; Karan, K.; Hickner, M. A.; Weber, A. Z.Impact of Substrate and Processing on Confinement of Nafion Thin Films. *Adv. Funct. Mater.* **2014**, 24, 4763– 4774.

[39] Eastman, S. A.; Kim, S.; Page, K. A.; Rowe, B. W.; Kang, S.; Soles, C. L.; Yager, K. G.Effect of Confinement on Structure, Water Solubility, and Water Transport in Nafion Thin Films. *Macromolecules* **2012**, 45, 7920–7930.

[40] Nagao, Y. Proton-Conductivity Enhancement in Polymer Thin Films. *Langmuir*, **2017**, 33 12547–12558.

[41] Nagao, Y.; Krishnan, K.; Goto, R.; Hara, M.; Nagano, S. Effect of Casting Solvent on Interfacial Molecular Structure and Proton Transport Characteristics of Sulfonated Polyimide Thin Films. *Anal. Sci.* 2017, *33*, 35–39.

[42]Wakita, J.; Jin, S.; Shin, T. J.; Ree, M.; Ando, S. Analysis of Molecular Aggregation Structures of Fully Aromatic and Semialiphatic Polyimide Films with Synchrotron Grazing Incidence Wide-Angle X-ray Scattering. *Macromolecules* **2010,** *43*, 1930-1941.

[43]Kusoglu, A.; Savagatrup, S.; Clark, K. T.; Weber, A. Z. Role of Mechanical Factors in Controlling the Structure-Function Relationship of PFSA Ionomers Macromolecules. **2012**, *45*, 7467–7476.

[44]de Araujo, C. C.; Kreuer, K. D.; Schuster, M.; Portale, G.; Mendil-Jakani, H.; Gebel, G.; Maier, *J. Phys. Chem. Chem. Phys*. **2009**, *11*, 3305-3312.

[45] Tonozuka, I. ;Yoshida, M. ;Kaneko, K. ;Takeoka, Y. ;Rikukawa, M. Considerations of polymerization method and molecular weight for proton-conducting poly(p-phenylene) derivatives. *Polymer* **2011**, *52*, 6020–6028.

[46] Hasegawa, T. A Novel Measurement Technique of Pure Out-of-plane Vibrational Modes in Thin Films on a Nonmetallic Material with No Polarizer. *J. Phys. Chem. B* **2002**, *106*, 4112–4115.

[47] Hasegawa, T.; Matsumoto, L.; Kitamura, S.; Amino, S.; Katada, S.; Nishijo, J. Optimum Condition of Fourier Transform Infrared Multiple-Angle Incidence Resolution Spectrometry for Surface Analysis. *Anal. Chem*. **2002**, *74*, 6049–6054.

[48] Hasegawa, T. Advanced Multiple-angle Incidence Resolution Spectrometry for

Thin-layer Analysis on a Low-refractive-index Substrate. *Anal. Chem.* **2007**, *79*, 4385–4389.

[49] Hasegawa, T.; Itoh, Y.; Kasuya, A. A. Experimental Optimization of P-polarized MAIR Spectrometry Performed on a Fourier Transform Infrared Spectrometer. *Anal. Sci*. **2008**, *24*, 105–109.

Chapter 4 General conclusion

In this work, the proton conductivity and structural properties of the Nafion thin film on Pt surface and sulfonated polyimide with alkyl side chain (ASPI) thin films were investigated.

Chapter 2.

Nafion membrane is one of the most promising PEM for PEFC because of their high proton conductivity. Recently, several studies of Nafion thin films have reported the structure, proton conductivity and water uptake and diffusion coefficient. However, for use in fuel cell operations, the structure and proton conductivity of Nafion thin films on a Pt surface have not been investigated systematically. By considering the above points, I focused on the development of proton conductivity measurement and analysis method of molecular structure of the Nafion thin films on Pt-deposited surface. I found that the Nafion has an orientation structure at the Pt-deposited surface. The degree of orientation on the Pt-deposited surface depends on the thickness. A different dissociation state of sulfonic acid groups was also observed. At the low-RH region, proton conductivity depends on the Pt-deposited and SiO_2 surfaces. Proton conductivity on the Pt-deposited surface was 1 order of magnitude higher than that on SiO_2 substrate, but its conductivity remained lower than that of the bulk membrane. This difference might derive from the

different thin film structure and/or the dissociation state of the protons at the sulfonic acid groups.

Chapter 3.

Sulfonated polyimides of planar and nonplanar polymer backbone were synthesized to investigate the relationship between the proton transport property and organized polymer nanostructure. These highly oriented ASPI thin films with organized lamellar structure achieved high proton conductivity (above 10^{-2} S/ cm). For the investigation of the water uptake of ASPI thin films, I developed the *in-situ* QCM system. The water uptake almost followed the order of the IEC values. The thresholds of the proton conductivity was observed at the c.a. λ = 5-6.5. This result was consistent with dissociation state of the sulfonic acid groups. All ASPI films exhibited strong birefringenceand LC like morphology with large domain. The results of GI-SAXS revealed that all ASPI thin films formed highly in-plane ordered structure, in which lamellar distance expands to the out-of-plane direction and a degree of molecular ordering improves by water uptake. I propose that the proton conductivity depends on not only the water uptake but also degree of the molecular ordering.

The highly in-plane orderings of the ASPI thin films are significantly influenced by molecular structure of diamine moiety with alkyl sulfonated side chains. The degree of the molecular ordering of those hydrated domains increased with proton conductivity.

Future Prospects

From this research, the results suggest that molecular orientation and molecular ordering can improve the proton conductivity.

The future prospects are mentioned as following

1. Nafion thin film shows low proton conduction, but still used as an actual binder in the catalyst layer for PEFC. Because, Nafion ionomer is state of arts ionomer and there are no alternative ionomer. Therefore, it is necessary to investigate more detailed proton conductivity, water uptake and orientation structure in the same environment such as carbon surface. Moreover, development of alternative ionomer for catalyst layer is necessary for both fundamental and application studies.

2. The different types of side chain should be investigated to understand the relationship between the lyotropic LC property and molecular structure as ASPI. The amphiphilic character such as solubility is varied by changing the length and flexibility

of the sulfonated alkyl chain. Different amphiphilic character provides the opportunity to extend the material application using lyotropic LC property.

Acknowledgement

I would like to express my deepest gratitude to my supervisor, Associate Professor Yuki Nagao for his valuable suggestion, kind encouragement, supervision, and supporting throughout my doctoral study.

I would like to gratefully thank to Professor Noriyoshi Matsumi for being my second supervisor and his kind guidance.

I would like to gratefully thank to Prof. Shusaku Nagano (Nagoya univ. VBL) and Assist. Prof. Mitsuo Hara (Nagoya univ.) to provide me a great opportunity to proceed minor research and collaboration, which widen my knowledge in another research field.

I would like to thanks to all of the present and former members in Nagao laboratory for kind supporting and discussion.

Yutaro Ono

Achievements

[Research Publications]

Y. Ono, Y. Nagao, “Interfacial Structure and Proton Conductivity of Nafion at the Pt-Deposited Surface”Langmuir **2016**, *32*, 352−358.

[Other Research Publications]

Y. Guo, Y. Ono, Y. Nagao, “Modification for Uniform Surface of Nafion Ultrathin Film Deposited by Inkjet Printing”, Langmuir **2015**, *31*,

[Award]

Poster award in 2nd International Symposium on Center of Excellence for Innovative Material Sciences Based on Supramolecules、石川、10 月 2016 年

[Conferences]

Oral Presentation

1、○小野祐太朗，後藤崚介，原光生，永野修作，安部隆，長尾祐樹　「スルホン化ポリイミド薄膜における側鎖構造のプロトン伝導性への影響」『第 66 回高分子討論会』愛媛、 9 月 2017 年

2、○小野　祐太朗、露木　新也、後藤　崚介、原　光生・永野　修作、長尾　祐樹、「組織構造を有するスルホン化ポリイミド薄膜のプロトン輸送特性と分子構造の相関」、『日本化学会第 96 春季年会(2016)』京都、3 月 2016 年

3、○Y. Ono, Y, Naga,「Proton transport property at Nafion-Pt interface」,『Pacifichem 2015』　Hawai, 12 月 2015 年

4、○小野　祐太朗、長尾祐樹　「Pt 界面における Nafion 薄膜の配向構造とプロトン輸送特性」、『第 66 回高分子討論会』仙台、9 月 2015 年

5、○小野　祐太朗、長尾祐樹　「異なる基板上に成膜した Nafion 薄膜の界面構造とプロトン輸送特性」、『日本化学会第 95 春季年会(2015)』千葉、3 月 2015 年

6、○小野　祐太朗、長尾祐樹　「Nafion-白金界面構造とプロトン輸送特性の評価」、『第 40 回固体イオニクス討論会』東京、11 月 2014 年

7、○小野　祐太朗、大山隆宏、長尾祐樹　「赤外 pMAIRS による Nafion-白金界面構造の評価」、『日本化学会第 94 春季年会(2014)』名古屋、3 月 2014 年

Poster Presentation

1、○小野祐太朗, 後藤峻介, 原光生, 永野修作, 安部隆, 長尾祐樹　「組織構造を有するスルホン化ポリイミド薄膜の水分子吸着量とプロトン輸送特性」、『第 24 回ポリイミド・芳香族系高分子会議』石川、12 月 2016 年

2、○Y. Ono, R. Goto, M. Hara, S. Nagao, T. Abe, Y. Nagao　「Liquid crystalline structure and proton transport in sulfonated polyimide thin film」、『2nd International Symposium on Center of Excellence for Innovative Material Sciences Based on Supramolecules』石川、10 月 2016 年

3、○Y. Ono, R. Goto, M Hara, S. Nagano, Y. Nagao　「Organized structure and proton transport property in sulfonated polyimide thin films」、『IISc-JAIST Joint Workshop on Functional Inorganic and Organic Materials』石川、3 月 2016 年

4、○Y. Ono, S. Tsuyuki, M. Hara, S. Nagano, Y. Nagao, 「Proton transport property in organized polyimide thin films」, 『Pacifichem 2015』 Hawai, 12 月 2015 年

5、○Y. Ono, Y. Nagao, 「Suppression of coffee-stain for Nafion thin film by ethanol vapor treatment」, 『Pacifichem 2015』 Hawai, 12 月 2015 年

6、○Y. Ono, Y, Nagao, “Proton transport property and interface structure at the Nafion-Pt”, 『第 25 回日本 MRS 年次大会』、横浜、12 月 2015 年

7、Y. Ono, Y, Naga, 「Evaluation of Nafion interface structure and proton conductivity at Pt surface」, 『5th Molecular Materials Meeting (M3)』 Singapore, 8 月 2015 年

8、○小野　祐太朗、長尾祐樹「赤外多角入射分解分光法(MAIRS)による燃料電池用プロトン交換膜の構造同定」『FT-IR・ラマン ユーザーズフォーラム 2015』大阪、5 月 2015 年

9、○Y. Ono, Y. Nagao 「The correlation of the interfacial structure and proton transport properties of Nafion thin film at the Pt interface」、『JAIST Japan-India Symposium on

Materials Science 2015 (JISMS 2015)』石川、　3 月 2015 年

10、○小野　祐太朗、長尾祐樹　「Nafion-白金界面構造とプロトン輸送特性の評価」『平成 26 年度北陸地区講演会と研究発表会』富山、11 月 2014 年
11、○小野　祐太朗、長尾祐樹　「Nafion-白金界面構造とプロトン輸送特性の評価」、『第 4 回 CSJ 化学フェスタ 2014』東京、10 月 2014 年